Electrical Characterization and Optimization of Gallium Arsenide Nanowire Ensemble Devices

ELECTRICAL CHARACTERIZATION AND OPTIMIZATION OF GALLIUM ARSENIDE NANOWIRE ENSEMBLE DEVICES

BY

ANDREW CHUNG ERN CHIA, B.Sc. (Hons.)

A THESIS

SUBMITTED TO THE SCHOOL OF GRADUATE STUDIES OF MCMASTER UNIVERSITY

IN PARTIAL FULFILLMENT OF THE REQUIREMENTS FOR THE DEGREE OF DOCTOR

OF PHILSOPHY

© Copyright by Andrew Chung Ern Chia, August 2013

All Rights Reserved

Doctor of Philosophy (2013) McMaster University

(Engineering Physics) Hamilton, Ontario, Canada

TITLE: Electrical Characterization and Optimization of Gallium Arsenide Nanowire Ensemble Devices

AUTHOR: Andrew Chung Ern Chia

B.Sc. (Hons.) SSP, (Physics)

Queen's University, Kingston, Canada

SUPERVISOR: Dr. R. R. LaPierre

NUMBER OF PAGES: xvi, 155

Abstract

III-V nanowire (NW) ensemble devices were fabricated using novel approaches to address key NW optoelectronic issues concerning electrical contacts, doping, surface effects and underlying electrostatics physics.

NWs were first embedded in a filling medium, thus achieving low sheet resistance front contacts while preventing shunts. Various filling materials were assessed for porosity, surface roughness and thermal stability, giving Cyclotene as an ideal filing material. Sonication was also introduced as a novel method to achieve perfect planarization.

The presence of the Cyclotene also enabled the NWs to be characterized precisely and easily by secondary ion mass spectrometry (SIMS) to give the NW dopant concentration with excellent spatial resolution. Additionally, SIMS characterization demonstrated the ability to characterize the height uniformity of individual segments in a heterostructure NW ensemble.

The focus of the work shifted towards surface effects on NW device performance. Therefore, Poisson's equation was solved to provide a comprehensive model of NW surface depletion as a function of interface state density, NW radius and

doping density. Underlying physics was examined where surface depletion was found to significantly reduce the conductivity of thin NWs, leading to carrier inversion for some.

This model was then applied in conjunction with a transport model to fit current-voltage curves of an AlInP-passivated GaAs NW ensemble device. A 55% decrease in surface state density was achieved upon passivation, corresponding to an impressive four order of magnitude increase in the effective carrier concentration. Additionally, conventional and time-resolved photoluminescence measurements showed intensity and carrier lifetime improvement greater than 20x upon passivation.

Finally, the model was extended to describe radial pn junction NWs with surface depletion to give radial energy band profiles for any arbitrary set of NW parameters. Specific cases were analyzed to extract pertinent underlying physics, while the built-in potential was optimized for the design for an optimal device.

Acknowledgements

First of all, I would like to thank my colleagues for the LaPierre group, both past and present for support and general guidance. At the top of that list is Dr. Ray LaPierre himself. I have at many times said that I could not have asked for a better supervisor and I maintain that stance until today. He has been a constant source of guidance. I have learned much from him about the ins and outs of academia, how to approach technical challenges systematically, but most of all keeping even keeled through both good and bad seasons of experimental success. His confidence and steady hand spared me so much of the common graduate student paranoia and I am so grateful for that. Within that LaPierre group, I would like to thank past members who were most influential during my formative years. These included Martin Plante, Subir Ghosh, Parsian Mohseni, and Chris Haapamaki. I would like to thank Jonathan Boulanger for numerous discussions. Going through graduate school alongside a friend was a true blessing. I would also like to thank my supervisory committee, Adrian Kitai and Rafael Kleiman, for excellent advice and guidance along the way. I am also deeply grateful for the contributions from collaborators. The foremost to thank is Dr. Martin Aagesen, who so freely shared information in helpful discussions, while being so willing to send state-of-the-art NW samples and spincoating polymers for device fabrication. I would also like

to acknowledge other collaborators, such as Dr. David Comedi, Dr. Zetien Mi, Dr. Richard Leonelli, and Dr. Silvia Rubini.

I would also like to thank the technical staff, without whom I definitely would not be here today. At the CEDT, I would like to thank Brad Robinson and Shahram Tavakoli for discussions on film growth and vacuum systems in my formative years and of course, the growth of all of my NW samples. I am also very grateful to Doris Stevanovic and Zhilin Peng for numerous hours of training, repairs (especially when I caused the breakdowns!) and general assistance in the cleanroom. I would also like to extend my gratitude to Jacek Wojcik for educating me on the assembly of vacuum systems. I am also very grateful to the staff at the CCEM whose assistance was indispensable especially in a project that relied so heavily on electron microscopy. In particular, I thank Fred Pearson, Carmen Andrei and Steve Koprich. Many thanks goes to Gary Good and Heng-Yong Nie at Surface Science Western for many helpful discussions, giving me a basic orientation to SIMS characterization and performing actual SIMS measurements. I would also like to acknowledge the administrative staff at the Department of Engineering Physics and the CEDT such as Marilyn, Linda, Nadine, Fran, Alex, Alexa.

Finally, I would like to thank my family. Beginning with both my parents and in-laws, you have been a constant source of support through these years and to you, I owe a debt of gratitude. I thank my cousins and siblings for providing much needed escape at key times from the rigours of research. Of all my family, I would most like to thank my wife, Joyce, who has been unwavering in support, celebrating the high points and being

a comfort in the low points. Joyce, I love you oh so much. Lastly, I would like to thank my Lord and Saviour, Jesus Christ, who is beyond gracious to a sinner like me.

I dedicate this to my wife, Joyce, God's greatest gift to me after Christ on the cross

Table of Contents

Abstract iii

Acknowledgements v

Table of Contents ix

List of Figures xiii

List of Tables xvi

1 Introduction 1

1.1 Background: NW Growth Kinetics 2

1.2 III-V Nanowire Optoelectronic Devices 4

1.3 Motivation for Present Work 8

1.4 Thesis Overview 10

2 Experimental Methods 12

2.1 Pre-growth Sample Preparation 12

2.2 Molecular Beam Epitaxy (MBE) 13

2.3 Electron Microscopy 14

2.3.1 Scanning Electron Microscopy (SEM) 15

2.3.2 Transmission Electron Microscopy (TEM) 17

2.4 Device Fabrication 18

2.4.1 Polymer Spincoating 18

2.4.2 Reactive Ion Etching (RIE) 20

2.4.3 Sonication 20

2.4.4 Electron Beam Evaporation 21

2.5 Electrical Characterization 21

2.5.1 Current-Voltage (I-V) Characterization 22

2.5.2 Capacitance-Voltage (C-V) Characterization 22

2.6 Optical Characterization 23

2.6.1 Photoluminescence (PL) 23

2.6.2 Time-Resolved Photoluminescence (TRPL) 24

2.7 Spatially-resolved X-ray Photoelectron Spectroscopy (SRXPS) 25

2.8 Secondary Ion Mass Spectrometry (SIMS) 26

3 Contact Planarization of Ensemble Nanowires 28

3.1 Introduction 28

3.2 Experimental Details 30

3.3 Results and Discussion 34

3.4 Conclusion 43

4 Unlocking Doping and Compositional Profiles of Nanowire Ensembles using SIMS 44

4.1 Introduction 44

4.2 Experimental Details 47

4.3 Results and Discussion 49

4.4 Conclusion 61

5 Analytical Model of Surface Depletion in Nanowires 63

5.1 Introduction 63

5.2 Theory 64

5.2.1 Partially Depleted Regime: $\mathbf{r}_q > 0$ 66

5.2.2 Fully Depleted Regime: $\mathbf{r}_q = 0$ 72

5.2.3 Effective free carrier concentration and conductivity 74

5.3 Results and Discussion 75

5.3.1 Model Output versus D_{it} 75

5.3.2 Model Output versus a 79

5.3.3 Comparison with SRXPS measurements 84

5.4 Conclusion 86

6 AlInP Surface Passivation of GaAs Nanowires 88

6.1 Introduction 88

6.2 Experimental Details 90

6.3 Results 93

6.4 Model 98

6.4.1 Modified Surface Depletion Model 99

6.4.2 Capacitance Model 102

6.4.3 Transport Model 104

6.5 Analysis and Discussion 108

6.6 Conclusion 110

7 Electrostatic Model of Radial PN Junction Nanowires 112

7.1 Introduction 112

7.2 Theory 113

7.2.1 Case 1: Partially Depleted P-core and N-shell 114

7.2.2 Case 2: Fully Depleted P-core and Partially Depleted N-shell 120

7.2.3 Case 3: Partially Depleted P-core and Fully Depleted N-shell 123

7.2.4 Case 4: Fully Depleted P-core and N-shell 127

7.2.5 Classification into Cases Based on NW Parameters 130

7.3 Results and Analysis 133

7.4 Discussion 140

7.5 Conclusion 142

8 Conclusion and Future Work 144

8.1 Thesis Summary 144

8.2 Future Work 146

References 148

List of Figures

Figure 1.1: Schematic of VLS growth of GaAs NWs 3

Figure 2.1: 45° tilted SEM image of GaAs NWs after growth. 16

Figure 3.1: 45° tilted SEM images and schematics outlining the effectiveness of the processing steps in fabricating the NW ensemble device. 31

Figure 3.2: 45° tilted SEM images of NWs spin coated with different filling polymers. .. 35

Figure 3.3: Post-anneal SEM images of showing cracking, delamination and the appearance of voids in the filling polymers following anneal. 38

Figure 3.4: I-V curves in various colour-coded probe configurations showing low sheet resistance front contacts and absence of shunts due to Cyclotene layer. 41

Figure 4.1: Dynamic SIMS profile of Te-doped GaAs NWs compared with SEM predictions and corresponding doping profile. 50

Figure 4.2: TOF-SIMS depth profile of Te-doped NWs. 52

Figure 4.3: SEM and TEM images of a GaAs/GaP axial heterostructure.. 54

Figure 4.4: Dynamic SIMS profile of Be-doped axial GaAs/GaP NWs compared with SEM predictions and corresponding doping profile. 56

Figure 5.1: Band diagram along the cross-section of a NW 66

Figure 5.2: Model predictions of key parameters and energy band diagrams versus D_{it} for different *a* curves. $N_D = 10^{18}$ cm^{-3} for all plots. 77

Figure 5.3: Model predictions of (a) w, (b) ψ_s, (c) ψ_0 and (d) V_{bb} versus a for different N_D curves. $D_{it} = 10^{13}$ cm^{-2}eV^{-1} for all plots. 80

Figure 5.4: Model predictions of (a) n_{eff} and (b) σ_{rel} versus a for different N_D curves. $D_{it} = 10^{13}$ cm^{-2}eV^{-1} for all plots. 83

Figure 5.5: SRXPS measurements of surface potential with theoretical fits from the surface depletion model. 85

Figure 6.1: Tilted and side-view SEM images and schematics outlining the effectiveness of the processing steps in fabricating the NW ensemble device. 92

Figure 6.2: SEM and TEM images of GaAs NWs encapsulated in AlInP........................... 94

Figure 6.3: I-V characteristics showing a significant current gain upon passivation........ 97

Figure 6.4: 1kHz-modulated C-V data (black circles, left axis) and interpolated *D_{it}(V)* (solid line, right axis) for unpassivated NWs.. 103

Figure 6.5: Equivalent circuit diagram of the ensemble device plus the radius distribution of all contacted GaAs cores. 105

Figure 6.6: PL spectra from passivated (red) and unpassivated (black) NWs 109

Figure 6.7: TRPL decay curves comparing passivated NWs (green) with unpassivated NWs (red) 110

Figure 7.1: Schematic (top) of a NW slice where O is the centre of the NW and the corresponding energy band diagram (bottom) for Case 1 of a p-core/n-shell NW. 115

Figure 7.2: Logic flowchart outlining the classification of a NW with arbitrary a, a_p, N_A, N_D and D_{it} into each of the four depletion cases 131

Figure 7.3: Contour plots showing the case (1-4) as a function of a and a_p. 134

Figure 7.4: Band diagrams of different (a_p, a) coordinates corresponding to the lettered points in Figure 7.3 (for a typical $D_{it} = 10^{13}$ cm^{-2}eV^{-1} and $N = 10^{18}$ cm^{-3}). 135

Figure 7.5: Contour plots showing the built-in potential as a function of a and a_p. Different rows and columns in the matrix correspond to different D_{it} and $N \equiv N_A = N_D$, respectively. 138

Figure 7.6: Contour plots showing the built-in potential as a function of a and a_p for a typical $D_{it} = 10^{13}$ cm^{-2}eV^{-1}. Different rows and columns in the matrix correspond to different N_D and N_A , respectively. 140

Figure 7.7: Contour plot showing the case (1-4) as a function of N_A and N_D for $a_p = 50$ nm, $a = 90$ nm, $D_{it} = 10^{12}$ cm^{-2}eV^{-1}. Inset: Schematic of proposed design. 142

List of Tables

Table 3.1: Outline of spin coating parameters for each filling material. 33

Table 3.2: Mechanical properties of each filling material. 37

Table 5.1: List of symbols 65

Table 6.1: Parameter values used in model 96

1 Introduction

Semiconductor nanowires (NWs) can be defined as free standing semiconductor rods with diameters ranging from a few to hundreds of nanometers and lengths ranging from hundreds of nanometers to tens of microns. Since the discovery of the vapour-liquid-solid (VLS) mechanism by Wagner and Ellis in 1964 [1], semiconductor NWs have been studied extensively by physicists and engineers alike. For physicists, NWs provide a unique platform upon which novel behaviours at the nanoscale can be explored. Most notably, indium antimonide NWs have been instrumental in providing evidence of Majorana bound states in superconductors [2]. For engineers, the initial motivation behind the study of NWs was the rapid scaling of conventional CMOS devices. As transistor size is reduced to the sub-100 nm range, conventional scaling meets with significant technological and fundamental challenges, such as a larger fluctuation in device performance metrics and the requirement for higher resolution top-down processes already pushed to their practical limits [3]. This necessitated the exploration of new systems to sustain CMOS scaling. Today, semiconductor NWs are one such system to meet this future demand. As NWs have been studied more extensively, the promise of NWs has extended beyond the initial CMOS vision. Due to an intersection between the fundamental physicist and pragmatic engineer approaches, NWs currently

hold great promise for a wide variety of future electronic, optoelectronic and even biochemical applications.

This introductory chapter will begin by giving some background behind the growth of NWs in Section 1.1, followed by a review of potential next generation NW optoelectronic applications in Section 1.2. Section 1.3 will then examine key issues preventing the realization of these optoelectronic applications with the subsequent Section 1.4 giving a thesis overview outlining this contribution's efforts in addressing these issues.

1.1 Background: NW Growth Kinetics

Typically, NWs are grown by the VLS mechanism which describes the process whereby a vapour growth species dissolves in droplets of liquid catalyst before finally precipitating the growth species out in solid form. The typical III-V NW growth process by VLS can be qualitatively explained as follows. First, a thin layer of Au is deposited onto a substrate (chosen as GaAs here for simplicity). The GaAs substrate is subsequently transferred to the molecular beam epitaxy system (MBE) where it is heated above the Au-GaAs eutectic temperature, causing the Au film to melt and segregate to form Au-Ga liquid alloy droplets on the surface of the substrate as shown in Figure 1.1a. These droplets serve as the seed particle for growth. When the growth

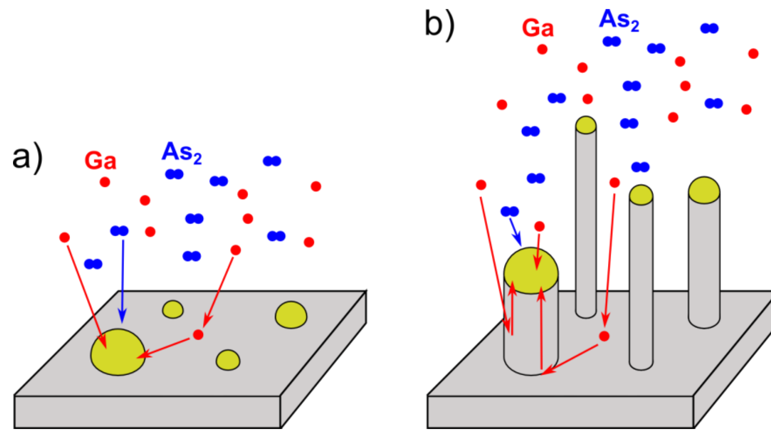

Figure 1.1: Schematic of VLS growth of GaAs NWs

species (specifically Ga and As_2 as per Figure 1.1a) is introduced above the sample, group III monomers will either impinge directly onto and subsequently dissolve into the seed particle or the monomers will adsorb onto the substrate and diffuse into the seed. Meanwhile, group V dimers and any additional impurity dopant atoms will dissolve into the seed particle by direct impingement. As the growth species is continually supplied, the seed particle will reach a state of supersaturation with the Ga and As. Past this point, the seed particles begin to precipitate the growth species, nucleating at the NW-substrate interface. As more of the growth species is supplied, each seed particle will precipitate more material beneath it, thus forming a pillar of material beneath each droplet as shown in Figure 1.1b. A collection of these pillars of material constitute the nanowire array. At this stage, group III adatoms impinging on the NW sidewalls can also diffuse to the seed particle to contribute to NW growth. Group V species may also

impinge on the substrate, desorb, and then impinge on the droplet (secondary adsorption).

The VLS mechanism, however, does not explain shell growth (or radial growth) of a NW. As the NW length begins to exceed the diffusion length of the adatoms, adatoms initially impinging on the substrate or near the base of the NW are unable to diffuse all the way to the seed particle, resulting in the group III incorporation by vapour-solid growth along the NW sidewall. In this way, short diffusion lengths result in radial growth which can be utilized to grow radial homojunctions or heterostructures. Alternatively, long diffusion lengths of group III adatoms promote axial growth for the synthesis of axial homojunctions or heterostructures. Diffusion length of adatoms can be varied by changing the temperature, V/III flux ratio and/or impingement rate.

1.2 III-V Nanowire Optoelectronic Devices

In addition to the ability to engineer a wide variety of axial and radial structures, III-V NWs have proven to possess many benefits that lend themselves well to many electronic and biochemical devices including NW transistors [4], flash memory [5] and gas sensors [6]. Of particular interest in the scope of this thesis are the wide variety of potential optoelectronic applications, including lasers [7], LEDs [8], photodetectors [9] and perhaps most interestingly, solar cells [10].

Due to the high crystal quality, high index of refraction and smooth surface of III-V NWs, individual NWs make for very ideal laser cavities [11]. GaN NW lasers have been demonstrated to have high quality factors while also boasting an unrivalled small cavity size thus giving great promise to its future use in nanophotonics integrated systems [12].

There has also been considerable research in the area of III-V, specifically III-nitride, NW LEDs because current GaN LEDs are limited by the need for expensive, thermally insulating, inflexible and size-limited silicon carbide or sapphire substrates for epitaxial growth of GaN thin films [13]. However, since substrate-NW interfacial strain can be accommodated along the NW sidewalls [14], GaN NW LEDs can be grown on cheap, thermally conductive, flexible and large lattice-mismatched substrates, thus alleviating these limitations. Lattice mismatch accommodation also allows for any composition of InGaN to be grown, thus opening the door for bandgap tuning. Additionally, recent NW LEDs have demonstrated an emission wavelength dependence on the NW diameter [15], giving the potential for multiple colours using the same material. This provides great promise in the field of solid state lighting.

III-V NW photodetectors has also been a topic of considerable interest due to the many unique NW benefits. For instance, the small size of NWs enables dense packing of devices, thus giving photodetectors a very high spatial resolution [16]. Additionally, the directionality of the NW allows for high polarization sensitivity. Finally, the high surface

area to volume ratio uniquely provides a high internal photoconductive gain, resulting in high sensitivity photodetectors [16].

Of all the potential NW optoelectronic devices, NW solar cells have been studied most intensively and perhaps hold the most promise due to the numerous benefits of NWs. For instance, it has been found that the textured, nonplanar geometry of NW ensembles results in superior light trapping in comparison to a thin film with equivalent material volume [17]. This reduces the material cost needed for maximum light absorption. Additionally, the synthesis of NWs typically has a lower thermal budget and device fabrication after NW synthesis is typically less complex than bulk solar cells, resulting in a further reduction in cost [18]. Furthermore, the synthesis of these NWs is compatible with current large scale semiconductor manufacturing capabilities. Perhaps the most innovative facet of NW solar cells is the ability to grow radial core-shell pn junctions in an effort to orthogonalize the light absorption and carrier collection directions [19]. This would allow the for light to be absorbed along a long optical path length in the axial direction of the NW, while carriers would be separated and collected across short distances in the radial direction of the NW, thus reducing the bulk recombination and effectively increasing the defect tolerance of the NWs. This opens the door for new material candidates previously unavailable to bulk solar cells due to poor film quality or low mobility [20]. Moreover, the ability of NWs to be grown on lattice-mismatched substrates allows NWs to be grown on flexible or transparent substrates, opening possibilities for further cost reductions and broader applications.

While these aforementioned benefits primarily offer a cost reduction akin to the paradigm of second generation photovoltaics, NW solar cells, like other candidate third generation technologies, possess several unique properties that offer a large boost in efficiency. For example, in addition to long optical path lengths and excellent light trapping, NW solar cells also benefit from photonic effects such as having intrinsic waveguide properties and possessing an intrinsic light concentrating nature due to the optical antenna effect [20]. This allows for the un-concentrated Shockley-Quiesser limit to be overcome without external light concentration [21]. Additionally, unlike in thin films and most technologies, strain relaxation along the NW sidewalls allows for high quality, epitaxial III-V NWs of various compositions to be grown on Si [22]. Without lattice-matching restrictions, a high quality, ideal bandgap double-junction tandem cell can be fabricated whereby a 1.7 eV energy bandgap III-V NW ensemble top cell is grown atop a Si bottom cell. The theoretical efficiency of this structure rivals that of current triple-junction solar cells restricted by lattice matching [23]. Furthermore, both the bandgap and absorption tunability of a NW ensemble can be utilized in conjunction with areal current matching to give flexibility in the NW material choice [24,25]. Finally, the small dimensions of the NWs and short charge separation distances make NWs an ideal platform for various third generation schemes such as quantum dot enhanced solar cells and hot carrier solar cells.

Due to their promise, the scope of the thesis will largely focus on the realization of high efficiency NW solar cells, although most of the results can be widely applied to other optoelectronic applications as well.

1.3 Motivation for Present Work

While NW solar cells hold great promise, the realization of these devices presents a new set of technical and fundamental challenges [26].

The first issue is one of electrical contacts. Due to the high-aspect ratio of NWs and the non-planar geometry of a NW ensemble, typical front contacts suffer from poor interconnection of contact material among the NWs, leading to a high sheet resistance [27]. Front contacts deposited directly onto NW ensembles also tend to create shunting paths present between the front electrode on top of the NWs and the rear electrode consisting of the substrate on which NWs are grown [28]. Both of these electrical contacting issues severely limit the performance of the solar cell [19].

Another issue is one of NW doping. In order to realize the ideal NW solar cell, there is a great need to control the doping concentration and uniformity in the NW. However, this task is made difficult due to the few methods available for precise, quantitative measurement of the doping concentration in NWs [29].

A third major issue is related to deleterious, efficiency-limiting surface effects. These novel NW device schemes capitalize on the small diameter of NWs which allow

for short charge separation distances, quantum confinement and lattice-mismatched growth of novel heterostructures due to effective strain relaxation at the NW sidewall surfaces [22]. However, these small NW diameters also serve to magnify harmful surface effects such as carrier depletion and surface recombination. These surface effects have been shown experimentally to significantly reduce device performance [30]. Recent numerical modelling of radial GaAs NW solar cells has shown that surface depletion and recombination are the primary factors limiting NW solar cell efficiency [31]. This stresses the need for surface passivation to reduce the density of surface states.

While effective surface passivation is crucial to the future of NW solar cells, this also highlights the immediate need to gain a quantitative, theoretical understanding of surface effects in NWs. However, this presents another major issue in that there has been little in literature that has given a thorough, quantitative description of surface effects in NWs, especially with regards to surface depletion of these high surface area to volume ratio structures. Moreover, while radial pn junction NW cells have been fabricated and have led to several promising results [18,32,33], there has been little in literature that has described the underlying electrostatics of radial pn junctions that may be limiting device performance. In all, a theoretical model is needed to better understand the electrostatics of NW solar cells.

1.4 Thesis Overview

Before the aforementioned issues are addressed, the experimental methods used to perform all the experiments will be described Chapter 2. This chapter will include details on NW growth, electron microscopy, device fabrication and characterization by electrical, optical, x-ray and mass spectrometric techniques.

Chapter 3 addresses the issue of electrical contacting to NW ensembles by examining the viability of different organic polymers as filling materials to achieve planarization of ensemble nanowire arrays. The porosity, surface roughness and thermal stability of each filling material was analyzed and can be found in published form in Nanotechnology [34].

Chapter 4 addresses the issue of dopant concentration evaluation in NWs by presenting secondary ion mass spectrometry (SIMS) on NWs embedded in a filling medium as a simple precise method of doping evaluation. This work was published in collaboration with Jonathan Boulanger (fellow PhD candidate in the LaPierre group) in Nanotechnology [35].

In Chapter 5, Poisson's equation is solved to provide a comprehensive model of nanowire (NW) surface depletion as a function of interface state density, NW radius and doping density. This was done to address the need for a deeper understanding of the surface depletion in NWs and has been published in the Journal of Applied Physics [36].

In an effort to address deleterious surface effects, Chapter 6 describes how GaAs NWs were passivated with AlInP, fabricated into devices and subsequently characterized by current-voltage (I-V) measurements and fit to an analytical model. Passivation was found to decrease interface state density while significantly boosting free carrier density. This work has been published in the Nanotech 2013 conference proceedings [37] and in Semiconductor Science and Technology [38].

Finally, a solution to Poisson's equation for radial pn junction NWs with surface depletion is given in Chapter 7. This resulted in a model capable of giving radial energy band and electric field profiles for any arbitrary core/shell doping density, core/shell dimensions and surface state density. This work has been published in the Journal of Applied Physics [39].

2 Experimental Methods

This chapter will give a general outline of the experimental methods used in this thesis. Since most of these processes are well-established and have been described in detail elsewhere, emphasis will be given to the underlying physics of each method and their specific application to semiconductor NWs.

2.1 Pre-growth Sample Preparation

Before a NW sample is grown by molecular beam epitaxy (MBE), a substrate must first be prepared for growth. In this thesis, a single-side polished, epi-ready, three-inch diameter GaAs (111)B substrate from AXT Incorporated is the standard substrate of choice. The substrate was doped at a density of (1-5)$\times 10^{18}$ cm^{-3} with either Si (n-type) or Zn (p-type). The specific details are given in the corresponding chapters. The substrate first undergoes a UV ozone treatment for 20 minutes to remove hydrocarbon contamination and grow a sacrificial oxide. The substrate is then etched in buffered HF for 30s to strip off the sacrificial oxide and leave behind a pristine GaAs surface. After etching, the substrate is rinsed in running deionized (DI) water for 10 minutes to rinse off the HF and finally dried with N_2 before being transferred to an electron-beam evaporation system. There, 1 nm of Au is evaporated onto the substrate at a rate of

0.1nm/s (as measured by a quartz crystal thickness monitor) to serve as the catalyst for VLS NW growth. With the Au deposited, the substrate is ready to be transferred to the MBE system for NW growth.

2.2 Molecular Beam Epitaxy (MBE)

MBE, as with other epitaxial techniques, allows for the deposition of epitaxial atomic layers arranged in the same manner as the underlying substrate. This gives a layer-by-layer growth which gives excellent control of doping, composition and thickness as well as high quality crystals suitable for high performance NW devices.

All NWs in this thesis were grown using a gas source MBE (GSMBE) made by SVT Associates. In this system, group III species are provided from effusion cells as monomers (Ga, Al, In), while group V species are supplied as dimers (P_2 and As_2) cracked from hydrides (PH_3 and AsH_3). This occurs in a gas cracker at a temperature of 950°C.

Upon completion of the pre-growth sample preparation steps mentioned above, the sample is transferred to a pre-deposition chamber where it is degassed for 15 minutes at 300°C before being transferred to the growth chamber where it is heated to 540°C under an inductively coupled hydrogen plasma (ICP) and As_2 overpressure for 10 minutes. The purpose of the high temperature is the desorption of oxygen from the surface and the formation of Au droplets, while the ICP is used to clean the surface of hydrocarbons, and the As_2 overpressure is needed to prevent As desorption. After 10

minutes, the sample is heated up to the growth temperature and the Ga shutter is opened, thus initiating NW growth by VLS described in the Introduction. The specific growth conditions, such as growth duration, V/III flux ratio, equivalent 2D growth rate and dopant flux, are tailored to the end goals of the experiment. As such, details of each growth will be given in subsequent corresponding chapters.

Following growth, the NWs are immediately characterized by electron microscopy.

2.3 Electron Microscopy

The Rayleigh criterion dictates that in order to spatially resolve two points, the minimum distance between those points is given by [40]

$$s = \frac{0.61\lambda}{NA} \tag{2.1}$$

where λ is the wavelength of the imaging source and *NA* is the numerical aperture. In vacuum, *NA* has a maximum value of unity, making the best theoretical resolution equal to roughly 60% of the imaging wavelength. Since the visible spectrum is on the order of hundreds of nanometers, NWs cannot be resolved by optical wavelengths. Alternatively, the relativistic wavelength of electrons are in the sub-Angstrom range, thus allowing even for the resolution of individual atoms to be well within the theoretical limitation of electron microscopy. As such, electron microscopy is used in the imaging of NWs.

2.3.1 Scanning Electron Microscopy (SEM)

To determine the basic morphology, density, length and radii of NWs in an ensemble, a JEOL JSM-7000F field emission scanning electron microscope (SEM) was used to tilt and image a cleaved edge of NWs standing on the substrate as shown in Figure 2.1. In this SEM, primary electrons are emitted by field emission from a tungsten source, accelerated to the sample and focused to a spot by magnetic lenses. At this spot, primary electrons penetrate the samples and are scattered elastically and inelastically within some interaction volume. Due to inelastic scattering, a number of loosely bound valence electrons are ejected by the primary electrons. These ejected electrons are called secondary electrons. Due to their low energy, only secondary electrons produced near the surface of the sample (within some escape depth) are able to escape the surface of the sample. Upon escape from the sample, the secondary electrons are detected by an Evenhart-Thornley detector which operates as follows. Secondary electrons are first attracted towards a positively biased (on the order of a hundred volts) wire-mesh electrode. Most of these electrons pass through the mesh and are accelerated further, impinging on a scintillator that is positively biased on the order of a thousand volts. The cathodoluminescent property of the scintillator results in the production of photons which impinge on the photocathode of a PMT, which converts the light into electrons (photoelectrons). Finally, through a series of dynodes, the photoelectrons are multiplied and detected at the anode, giving rise to an amplified signal with magnitude corresponding to the number of secondary electrons entering the

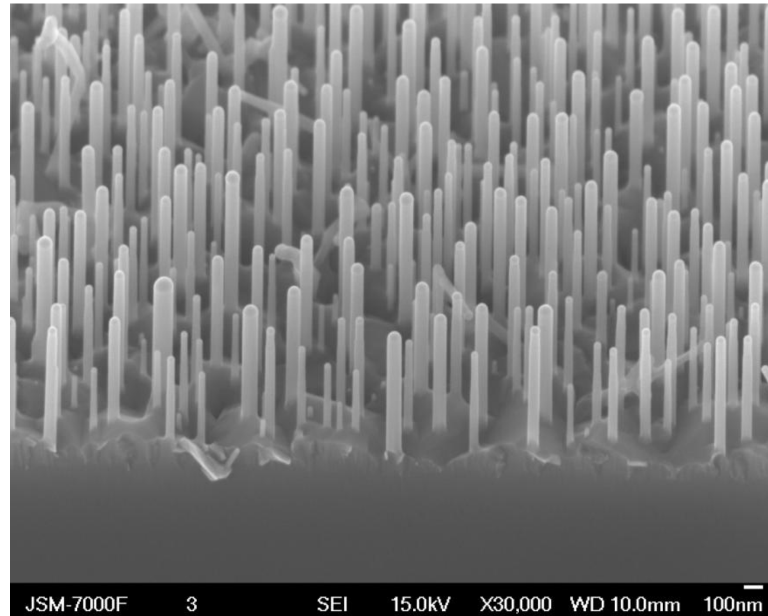

Figure 2.1: 45° tilted SEM image of GaAs NWs after growth.

detector. In this way, a signal is produced for each electron spot. As such, a full secondary electron image of the whole sample can be achieved by rastering the electron beam across the entire sample and detecting the secondary electrons at each spot.

For the purpose of NWs, the sample is cleaved prior to imaging to yield a clean edge, free of broken NWs or substrate chunks as shown in Figure 2.1. The heights of NWs standing perpendicular to the surface can be calculated easily from the tilt angle by basic trigonometry while the diameters of the NWs can be measured directly. When viewing a cleaved edge at an angle, it is clear from Figure 2.1 that the NW diameters and heights can be measured for each NW within a few hundred nanometres from the edge. This allows for representative height versus diameter (or radii) distributions to be calculated. To calculate the density of the NWs, plan view SEM images are used.

2.3.2 Transmission Electron Microscopy (TEM)

In addition to the imaging of NW ensembles by SEM, individual NWs were also imaged by a high resolution JEOL 2010F transmission electron microscope (TEM) to examine material properties such as heterostructure morphology and chemical properties such as stoichiometry.

Before imaging in TEM, the samples were first prepared using sonication. Small NW specimens were placed into vials filled with methanol and sonicated for five to thirty seconds. This broke the NWs, causing them to mix with the methanol. By applying drops of this mixture to a TEM grid, broken NWs were deposited onto the grid for TEM analysis.

For the scope of this thesis, the microscope was mostly operated in high angle annular dark field (HAADF) mode in conjunction with analysis by energy dispersive x-ray spectroscopy (EDX). In HAADF imaging, an annular detector is located below the sample to collect electrons scattered at large angles. Samples containing high atomic number elements will cause electrons to be scattered at large angles, subsequently resulting in detection by the annular detector and appearing brighter. This gives an elemental sensitivity in HAADF that is very useful in confirming the intended morphology of both radial and axial NW heterostructures.

To shed more light on the composition of the NWs, EDX is used. In EDX, an incoming primary electron ejects a core electron (at K, L levels), resulting in a vacancy in the shell. This vacancy is then filled by an electron from an outer shell, resulting in the

emission of a x-ray at an element-specific energy. Upon detection and energy measurement of these characteristic x-rays, the chemical composition of the sample can be determined. EDX measurements were taken primarily as linescan measurements generated using INCA software from Oxford Instruments.

2.4 Device Fabrication

After the analysis of basic morphology and stoichiometry of grown NW ensembles, the NW ensembles are then typically fabricated into devices. While the fabrication recipes vary with application, the general process and principles are similar to each and will be discussed below. A detailed description of the specific fabrication recipes and processing parameters will be given in subsequent relevant chapters.

2.4.1 Polymer Spincoating

In general, the first step in the device fabrication is the spincoating of a filling polymer required for front contact planarization and prevention of shunts in the ensemble device. Although different polymers were used, this discussion will be limited to the spincoating of Cyclotene due to its exclusive use for most of the thesis. Chapter 3 gives specific spincoating details (e.g. speed, dilution, ramp acceleration, softbake time/temp, hardbake time/temp) for each polymer, while giving justification for Cyclotene as the ideal choice as a filling medium.

To begin, ~0.5 mL of Cyclotene is dispensed onto an ensemble NW sample using a syringe such that Cyclotene uniformly covers the whole sample. The Cyclotene is then allowed to sit for 5 minutes to seep to the bottom of the NWs in an effort to minimize voids in the subsequent film. The sample is then spincoated at a set speed dictated by the desired cyclotene thickness.

Variations to this process included the occasional use of an adhesion promoter or dilution. For some samples, a layer of adhesion promoter (AP3000 from DOW Chemical) was spun on the NWs at 2000 RPM for 20s prior to spincoating the Cyclotene. However, AP3000 was generally observed to be redundant for high NW densities due to the larger area of adhesion at the polymer/semiconductor interface. In other samples, the Cyclotene was diluted into a 1:1 or 3:1 volume mixture of Cyclotene 3022-35 to T1100 thinner to reduce the thickness of the spincoated film.

After spincoating, the sample is softbaked for 90s at 100°C and subsequently transferred to a nitrogen glovebox where it is hardbaked (to cure the Cyclotene) by ramping the temperature from room temperature to 250°C at a slow rate of 5 ^{o}C/min and subsequently baking at a constant 250°C . The nitrogen glovebox environment provided an oxygen concentration of less than 100 ppm. The baking conditions were chosen upon recommendation by the manufacturer.

2.4.2 Reactive Ion Etching (RIE)

After spincoating the NW ensemble with Cyclotene, a reactive ion etching (RIE) step is often needed to reduce the thickness of the Cyclotene to a desired height. This was performed using a Technics Micro RIE series 800 system equipped with an RF power supply operating at 13.56 MHz. This step enabled the removal of the Cyclotene top layer mechanically by sputtering and chemically by reaction of ionized O_2 and CF_4 etch gas with cyclotene. Typical RIE parameters included an O_2 and CF_4 flow rate of 2 sccm each, an RF power of 50 W and a chamber pressure of 150 mTorr as recommended by previous reports [41].

2.4.3 Sonication

Sonication was used as the next step as a novel method to remove the tops of the NWs protruding out of the Cyclotene. This was done to meet two goals. Firstly, it was used to achieve complete planarization of the subsequent top contact. Secondly, passivated samples were often composed of conductive GaAs cores completely encapsulated in insulating AlInP. Sonication removed the insulating AlInP at the top of the NWs to allow the GaAs to be contacted.

Sonication was performed in DI water for 30-60 minutes at 40 kHz in a Branson 1510 ultrasonic cleaner. In this system, sound waves are induced in the tank, creating alternating high and low pressure states in the solution. During the low pressure stage cavitation occurs whereby microscopic bubbles (cavities) are formed and grow. During

the high pressure stage, the bubbles implode, thus agitating surfaces around it. This implosion is strong enough to knock off entire NW sections protruding out of the Cyclotene.

2.4.4 Electron Beam Evaporation

The final step in the device fabrication was the deposition of front and back contacts by electron beam evaporation. In the scope of this thesis, only opaque contacts were used to make contact to n-type GaAs. As such, the bottom contact was composed of standard 25 nm Ni, 50 nm Ge and 120 nm Au to make ohmic contact. Conversely, the top contact was composed of an array of 0.5 mm^2 circular contact pads composed of 50 nm Ni, 100 nm Ge and 650 nm Au. This added thickness was chosen due to the additional roughness of the Cyclotene layer relative to the substrate. After contact deposition, the samples are annealed in N_2 at 400 ^oC for 30s to make an ohmic, alloyed contact to the GaAs.

2.5 Electrical Characterization

In order to probe the electrical properties of the fabricated NW devices, current-voltage (I-V) and capacitance-voltage (C-V) characterization methods were used.

2.5.1 Current-Voltage (I-V) Characterization

To determine the I-V characteristics of the device, a two-point probe system and a Keithley 2400 sourcemeter was used to ramp the bias voltage between an initial and final voltage while measuring the current along the way. Due to the fragility of the front contacts, specialized spring clip probes were used to probe the top of the device. To make contact to the back contact of the device, the back contact was epoxied to a copper plate with silver paste and the copper plate was subsequently contacted with a probe. At its most fundamental level, the purpose of the these measurements is to examine resistivity and effective free carrier density. Further analysis in the shape of I-V curves gives insight into diode characteristics and underlying physics of the device.

2.5.2 Capacitance-Voltage (C-V) Characterization

C-V characteristics were measured for NW devices using a Hewlett Packard HP4192A analyzer with a typical 0.01 V modulation voltage at frequencies ranging from 1 kHz to 10 MHz. The sample was connected to the instrument by means of the HP 16047 C Test Fixture. These measurements were performed by Monica Tirado and David Comedi, a collaborator at Laboratorio de Nanomateriales y de Propiedades Dieléctricas in Argentina.

To generate the C-V curve, a dc bias is first applied, followed by the application of a small ac modulation voltage, V_{AC}, at some frequency, *f*. A measurement of the resultant AC current, I_{AC} yields the capacitance at that particular DC bias as:

$$C = \frac{dQ}{dV} = \frac{dQ}{dt}\left(\frac{dV}{dt}\right)^{-1} = \frac{I_{AC}}{2\pi f V_{AC}} \tag{2.2}$$

For NW devices, C-V was used primarily in examining the surface charge and corresponding surface state density by filling and de-filling surface states with the ac modulation voltage.

2.6 Optical Characterization

The optical characterization techniques of photoluminescence (PL) and time-resolved photoluminescence (TRPL) were used to probe the impact of surface defects on the luminescence and carrier lifetimes of the NW devices.

2.6.1 Photoluminescence (PL)

PL measurements were performed on sonicated NWs dispersed on a Si substrate with thermally grown 300nm thick silicon oxide. The excitation source used was a semiconductor laser diode (λ≈635 nm), while the PL emission was detected and measured by a high-resolution spectrometer and a single channel InGaAs photodiode

with lock-in amplification. These measurements were performed in collaboration with Yukun Li, Songrui Zhao and Zetian Mi at McGill University.

For the purposes of NWs, PL was used to analyze the impact of surface state density on optical quality. PL examines the internal efficiency of the NWs, a measure of light-emitting radiative recombination of electron-hole pairs excited by the laser source. Material defects, such as surface states, play a large role in quenching radiative recombination, thus reducing internal efficiency and resultant light emission. This effect is pronounced in NWs due to the high surface area to volume ratio, thus making PL a useful tool in examining the effectiveness of surface passivation.

In the present thesis, PL spectra were measured at room temperature only. While this elevated temperature results in undesirable thermal line broadening, the line width contribution from thermal broadening is sufficiently narrow to examine band-to-band transitions and compare intensities between passivated and unpassivated NW samples.

2.6.2 Time-Resolved Photoluminescence (TRPL)

TRPL measurements were also performed on NWs dispersed on a Si substrate with thermally grown 300nm thick silicon oxide. The sample was excited by a laser of 780 nm wavelength, 76.1 MHz repetition rate, ~2 ps pulse duration and 250 µW power. Measurements were performed at 14 K in a closed-cycle, exchange-gas cryostat. The PL signal was dispersed with a 50 cm focal length spectrometer with 600 g/mm grating and

ultimately detected by a silicon avalanche photodiode (Si-APD). Time-correlated single photon counting electronics were from Picoquant. These measurements were performed in collaboration with Felix Thouin and Richard Leonelli at Université de Montréal.

TRPL analyzes the intensity decay of light emitted by recombining electron-hole pairs. As shown in Chapter 5, surface depletion in NWs is expected to sweep excited excess minority carriers into surface trap states, thus reducing the number of electron-hole pairs available for radiative recombination. This leads to a rapid decay of PL light intensity or alternatively, a large reduction in the PL lifetime.

2.7 Spatially-resolved X-ray Photoelectron Spectroscopy (SRXPS)

Spatially-resolved X-Ray Photoelectron Spectroscopy (SRXPS) measurements were performed along the length of free standing NWs to determine the surface Fermi level. SRXPS was performed using a scanning photoelectron microscope (SPEM) whereby a x-ray beam is focused to a spot using Fresnel zone plate optics. Emitted photoelectrons are detected by a SPECS-PHOIBOS 100 hemispherical analyzer with a 48-channel plate spectrometer. These measurements were performed by Mattia Fanetti and others (collaborators from Silvia Rubini's group) at the ESCA Microscopy beamline of the Elettra – Sincrotrone Trieste light facility [42] boasting an excellent ~10Å escape

depth, sub-50nm lateral resolution, sub-200meV spectral resolution and a small 100meV uncertainty [43].

The key operating principle of x-ray photoelectron spectroscopy (XPS) is the photoelectric effect. If photons are incident on a material, photoemission of electrons will occur if the incident light energy is larger than the binding energy. In XPS, X-rays are chosen to be the incident photon, while the photoelectron energy is measured using a spectrometer. If both the incident light energy is known and the resultant photoelectron kinetic energy is measured, the binding energy can be found, thus allowing for chemical and elemental identification. For NWs, determination of the binding energy of electrons trapped in surface states enables the location of the Fermi level at the surface to be calculated, giving valuable insight into understanding NW surface depletion. Additionally, since the SPEM system allows for focussing of the x-ray beam, the surface Fermi level can be determined with excellent spatial resolution.

2.8 Secondary Ion Mass Spectrometry (SIMS)

Secondary ion mass spectrometry (SIMS) measurements were performed on NW ensemble samples planarized with Cyclotene using a Cameca IMS-3f Dynamic SIMS system and an ION-TOF TOF-SIMS IV Time-of-flight (TOF) system. For dynamic SIMS, either 10keV Cs^+ or 12.5keV O^+ primary ion beams were used to analyze a 60 μm-diameter circular area. The primary ion choice was governed by the relative sensitivity

factors of the ions to be monitored. For the TOF SIMS, a Bi^{3+} primary ion beam pulsed at 10 kHz was used to analyze a 50µmx50µm square area. SIMS measurements were performed at Surface Science Western at the University of Western Ontario.

In SIMS, the primary beam removes material by sputtering while a mass spectrometer analyzes and identifies sputtered ions (called secondary ions). SIMS boasts excellent elemental sensitivity (as low as 10^{14} cm^{-3}) and a depth resolution on the order of several nm due to low sputtering rates [40]. To achieve a depth profile, the secondary ion intensity is monitored as a function of time as the sample is sputtered by the primary beam. At the end of the measurement, the depth of the sputtered crater can be measured to convert the time scale to a depth scale, thus giving a secondary ion intensity versus depth profile. Finally, the secondary ion intensity scale can be converted to a concentration scale by comparing to a standard of known composition. For NWs, SIMS offers a simple and precise tool in the determination of the total impurity dopant concentration.

3 Contact Planarization of Ensemble Nanowires

3.1 Introduction

As discussed previously in Chapter 1.3, the non-planar geometry of NW ensembles presents significant technical issues of high sheet resistance front contacts due to poor interconnection of contact material and shunting paths due to the contact between the substrate and the front contact. These challenges can be addressed by the addition of an inactive, support medium to fill the space between the NWs [44]. The presence of this filling medium isolates the front and back contacts of the device to prevent shunting [45], while also planarizing the NW array to allow the deposition of a planar front contact with low sheet resistance on top of the NWs [46]. This chapter was largely taken from our work published in Nanotechnology [34].

Planarization of ensemble NWs using both inorganic and organic filling materials has been reported previously [18,32,46–51]. Among inorganic filling materials, silicon dioxide (SiO_2) and spin on glass (SOG) have been most extensively studied [46,47]. Chemical vapour deposition (CVD) of SiO_2 resulted in a conformal deposition which made filling difficult for tall NWs and created voids in the SiO_2 which in turn caused delamination during subsequent processing [48]. For SOG, planarization was difficult to

achieve for a dense array of thin NWs [48]. Among organic filling materials, some success has been achieved by using poly(methyl methacrylate) (PMMA) [49,50], polydimethylsiloxane (PDMS) [32], accuflow T-27 (Honeywell) [48] and Cyclotene resin (DOW chemical) [18] as filling materials. Conversely, other organic materials have faced many challenges. Spin coated polystyrene caused bundling of NWs due to capillary forces [51], while spin coated Shipley 1518 photoresist left voids between tall wires [44]. Despite these varying degrees of success, there has been no consistent study comparing the suitability of different inorganic materials as a feasible filling medium for planarization. Additionally, there has been no established standard by which the effectiveness of planarization can be assessed.

In this chapter, analysis will be given to the viability of four different transparent, organic polymers as candidate filling materials for radial GaAs-AlInP heterostructured NWs. The studied organic polymers include S1808 photoresist from Shipley, SC200 from Silecs, SU8-2 from Microchem and Cyclotene 3022-35 from DOW Chemical. Unlike previous studies, we will both qualitatively analyze the thermal stability and porosity of each polymer while quantitatively examine the surface roughness to assess the suitability of a material as a filling medium for planarization. Finally, a novel approach of sonication after the addition of the filling medium will be explored as the penultimate processing step towards fabrication of ensemble NW devices.

3.2 Experimental Details

The radial GaAs-AlInP heterostructured NWs were grown by VLS in a gas source molecular beam epitaxy (MBE) system. Before growth, an n-doped (111)B GaAs substrate with an approximate doping density of $1x10^{18}$ cm^{-3} was cleaned by a 20 minute UV ozone, a subsequent 30s buffered HF bath and a final 10 minute rinse in deionized (DI) water. Then, 1 nm of Au was evaporated onto the substrate to serve the role of seed particles for VLS NW growth. The substrate was then placed into the MBE system where it was prepared for growth by degassing and plasma cleaning as described in Chapter 2.2, followed by the NW growth. The NW structure consisted of n-doped GaAs cores covered by nominally undoped AlInP shells. The n-doped GaAs cores were grown at 575 ^{o}C for 25 minutes with a 2D equivalent growth rate of 1 µm/hr and a V/III flux ratio of 2.3. The GaAs cores were Te-doped at a nominal doping density of $1x10^{18}$ cm^{-3} as determined by previous thin film calibrations. The undoped, lattice-matched AlInP shells were grown at 500 ^{o}C for 20 minutes with a 2D film growth rate of 0.5 µm/hr and a V/III flux ratio of 3.45. This structure was grown for future optoelectronic device studies with AlInP as a window layer. The as-grown NWs shown schematically in Figure 3.1a were then characterized using a JEOL JSM-7000F scanning electron microscope (SEM).

After growth and characterization by SEM, a series of processing steps were performed on the NW ensemble to achieve a planar contact that interconnects the NW

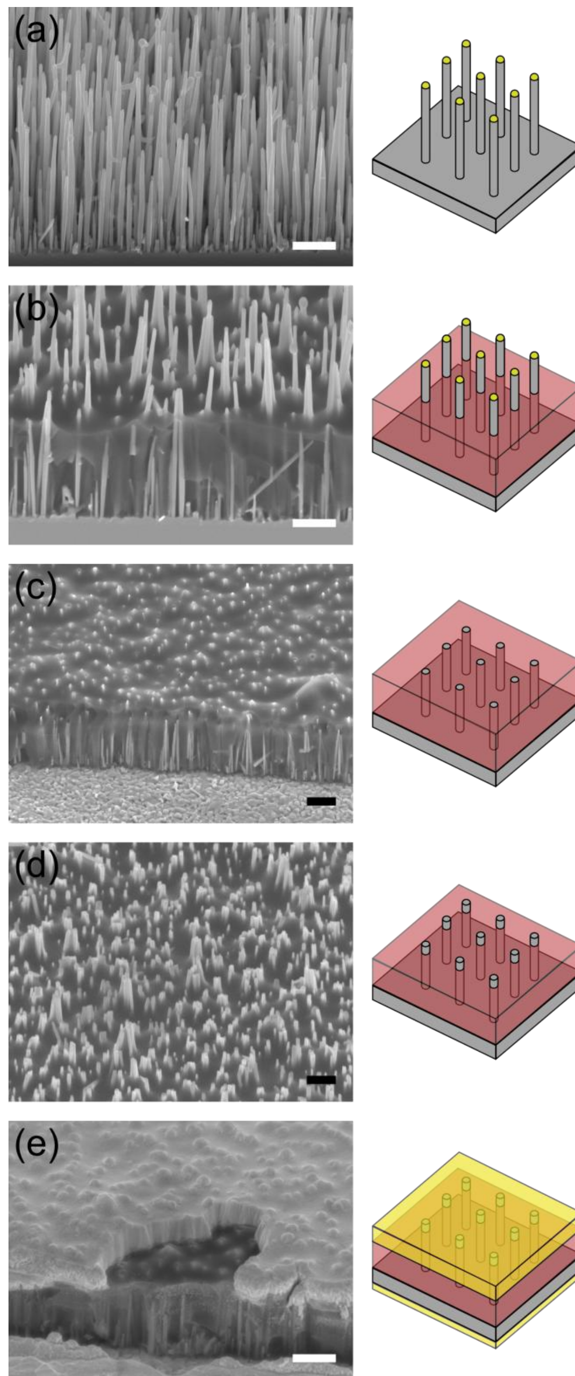

Figure 3.1: 45° tilted SEM images and schematics of the NW ensemble (a) directly after growth, (b) after spin coating with Cyclotene, (c) after sonication in DI water, (d) after RIE and (e) after contact deposition and annealing. The scale bars are 1μm.

array at their top. First, ~0.5 mL of each of the four polymers (S1808, SC200, SU8 and Cyclotene) was dispensed across individual ensemble NW samples using a syringe such that each polymer uniformly covered each sample. Each polymer was then allowed to sit for 5 minutes to seep to the bottom of the NWs in an effort to minimize voids in the subsequent film. To achieve the structure shown schematically in Figure 3.1b, each NW sample was then spin coated with different spinning and curing parameters (outlined in Table 3.1) as recommended by the manufacturer. It must be noted that prior to spin coating the Cyclotene, a layer of adhesion promoter (AP3000 from DOW Chemical) was spun on the NWs at 2000 RPM for 20s. Additionally, the Cyclotene hard bake was done in a nitrogen glovebox environment with an oxygen concentration of less than 100 ppm at a slow temperature ramp of 5 ^{o}C/min as recommended by the manufacturer. Following the spin coat, each sample was studied using SEM to assess the viability of each polymer as a suitable planarizing material. For reasons that will be discussed later, only the SU8- and Cyclotene-spun NW samples were chosen for further study.

Thereafter, the SU8 and Cyclotene samples were sonicated in DI water for 30 minutes at 40 kHz as a novel method to remove the tops of the NWs that are exposed above the polymer film, thus achieving complete planarization of the NW array as shown schematically in Figure 3.1c. As shown schematically in Figure 3.1d, the samples then underwent reactive ion etching (RIE) to etch back the planarizing layer thereby exposing a controlled length of the NWs to allow for subsequent contacting. The SU8-covered sample was plasma etched for 2 minutes with an O_2 flow rate of 28 sccm, an RF

Table 3.1: Outline of spin coating parameters for each filling material.

		S1808	SC200	SU8	Cyclotene
Spin	Duration (s)	30	20	60	60
	Speed (RPM)	4000	2000	3000	3000
Softbake	Duration (min)	2	5	4	1.5
	Temperature (^{o}C)	110	150	95	100
Hardbake	Duration (min)	2	5	5	30
	Temperature (^{o}C)	130	200	200	250

power of 100 W and a chamber pressure of 350 mTorr, while the Cyclotene-covered sample was plasma etched for 2 minutes with an O_2 and CF_4 flow rate of 2 sccm each, an RF power of 50 W and a chamber pressure of 150 mTorr as recommended by previous reports [41].

Next, opaque, metal top contacts composed of 50 nm Ni, 100 nm Ge and 650 nm Au were deposited by electron beam evaporation. To prevent possible short-circuits at the sample edges, the top contacts were deposited through a shadow mask consisting of an array of 800 µm-diameter apertures to produce discrete contact pads. A contact on the bottom of the substrate composed of 25 nm Ni, 50 nm Ge, and 1200 nm Au were also deposited by electron beam evaporation as shown schematically in Figure 3.1e. Finally, the sample was annealed in N_2 for 30s at 400 ^{o}C to alloy the contacts to the GaAs.

SEM analysis was used to study the morphology of the filling materials and contact after each processing step. The performance of the devices was analyzed using I-V characteristics acquired between the top and bottom contacts by a two-point probe

system and a Keithley 2400 sourcemeter. I-V characteristics were used to assess whether the filling medium had successfully prevented shunts between the top and bottom contact. Finally, the two probes were placed across a single contact pad and an I-V curve was measured to ensure a low sheet resistance due to effective planarization.

3.3 Results and Discussion

Figure 3.1a shows an SEM image of the NW array directly after growth. NWs from the same growth sample were used to assess all of the polymers. Analysis of SEM images of the NW array showed that the heights of the NWs varied from ~0.5 to 5 μm while the diameters of the NWs varied between 40 nm and 140 nm. The density of the NW ensemble was approximately $2x10^9$ cm^{-2}. Figure 3.2 shows SEM images of four samples each subsequently spin coated with their respective polymer (S1808, SC200, SU8 and Cyclotene). The heights of the S1808, SC200, SU8 and Cyclotene films were found to be approximately 3.3 μm, 2.7 μm, 3.3 μm and 3.5 μm, respectively. Analysis of SEM images such as those in Figure 3.2 can be used to study the porosity and surface topography of each filling material.

Qualitative examination of porosity was performed by visual observation of the number and relative size of voids present in the filling material. While no observable voids were present for the SC200 (Figure 3.2b) and SU8 (Figure 3.2c) samples, there were many large voids in the S1808 layer (Figure 3.2a), but only a few small voids in the

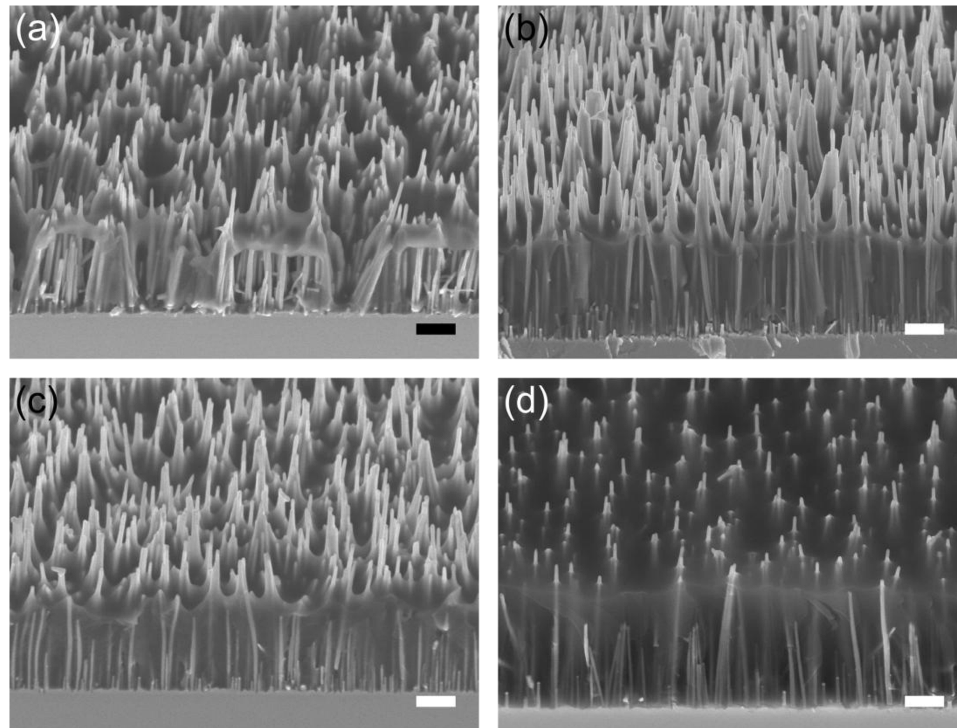

Figure 3.2: 45° tilted SEM images of NWs spin coated with (a) S1808, (b) SC200, (c) SU8 and (d) Cyclotene. The scale bars are 1µm.

Cyclotene layer (Figure 3.1b and Figure 3.2d). The presence of voids may be due to the fact that S1808 has the lowest viscosity of all the polymers examined according to the manufacturers' specifications. Although a low viscosity is generally desired for filling purposes, too much polymer may be spun off if the viscosity is too low, thus leaving voids. The presence of voids can be detrimental to future processing because it prevents controllable wet etching where the polymer is used as an etch stop, and has previously led to NW delamination [48]. It must also be noted from Figure 3.2a that the NWs tend to bundle exclusively in the S1808 samples indicating the presence of capillary forces as previously reported [51]. Since large voids are left behind in the S1808 layer, this leads

to an imbalance of capillary forces towards the sides of NWs which are coated. As such, the NWs bundle at areas where there is polymer.

Surface topography was analyzed quantitatively by using SEM images to find the profile roughness parameter, R_a, of each sample given by [52]:

$$R_a = \frac{1}{n}\sum_{i=1}^{n}|y_i| \tag{3.1}$$

where y_i is the height difference between the mean line of the profile of the filling material and the ith data point (horizontal position along the polymer surface). R_a was calculated by dividing side-view SEM images taken at 10,000x magnification horizontally into n=48 points each separated by 250 nm and finding y_i at each data point. The R_a values were calculated to be 651 nm, 207 nm, 237 nm and 93 nm for the S1808, SC200, SU8 and Cyclotene samples, respectively. By inspection, this trend is clearly consistent with Figure 3.2. The large undulation of the S1808 layer in Figure 3.2a is consistent with a large R_a, while it is clear from inspection of Figure 3.2b-d that SC200, SU8 and Cyclotene have much smoother profiles with Cyclotene being the smoothest in agreement with the small calculated R_a value of 93 nm. Practically, the R_a values are of great significance because they represent the minimum top contact thickness required for good interconnection of contact material between NWs. These roughness parameter values and the porosity results from the previous discussion have been summarized in Table 3.2. Since the S1808 layer had many large voids and a relatively large R_a due to its

Table 3.2: Mechanical properties of each filling material.

	S1808	SC200	SU8	Cyclotene
Thermal Stability	-	Delaminates under anneal	Cracks under anneal. Stable if under contact.	Stable
Porosity	Many, large voids present	No observable voids present	No observable voids present	Few, small voids present
Roughness parameter, R_a (nm)	651	207	237	93

conformal nature, S1808 was disqualified as a potential planarizing material and no subsequent processing was done on this sample.

Before further processing of the remaining 3 candidates (SC200, SU8 and Cyclotene), a small piece of each sample was cleaved off and annealed at 400 ^oC for 30s in N_2 to qualitatively examine the thermal stability of each polymer to subsequent high temperature processes as typically required in Ohmic contact formation. The filling material is referred to as thermally stable if it maintains its structural integrity with no evidence of cracking or delamination when annealed at the aforementioned conditions. Although the Cyclotene film was found to maintain its structural integrity and morphology, this was not the case for the SC200 and SU8 films. Figure 3.3a shows severe cracking and delamination throughout the SC200 film after annealing. For this reason, SC200 was disqualified as a potential filling material. As shown in Figure 3.3b, the SU8 film exhibited cracks spanning tens of microns but no delamination after annealing. As shown in Figure 3.3(c), however, no cracking was observed under the

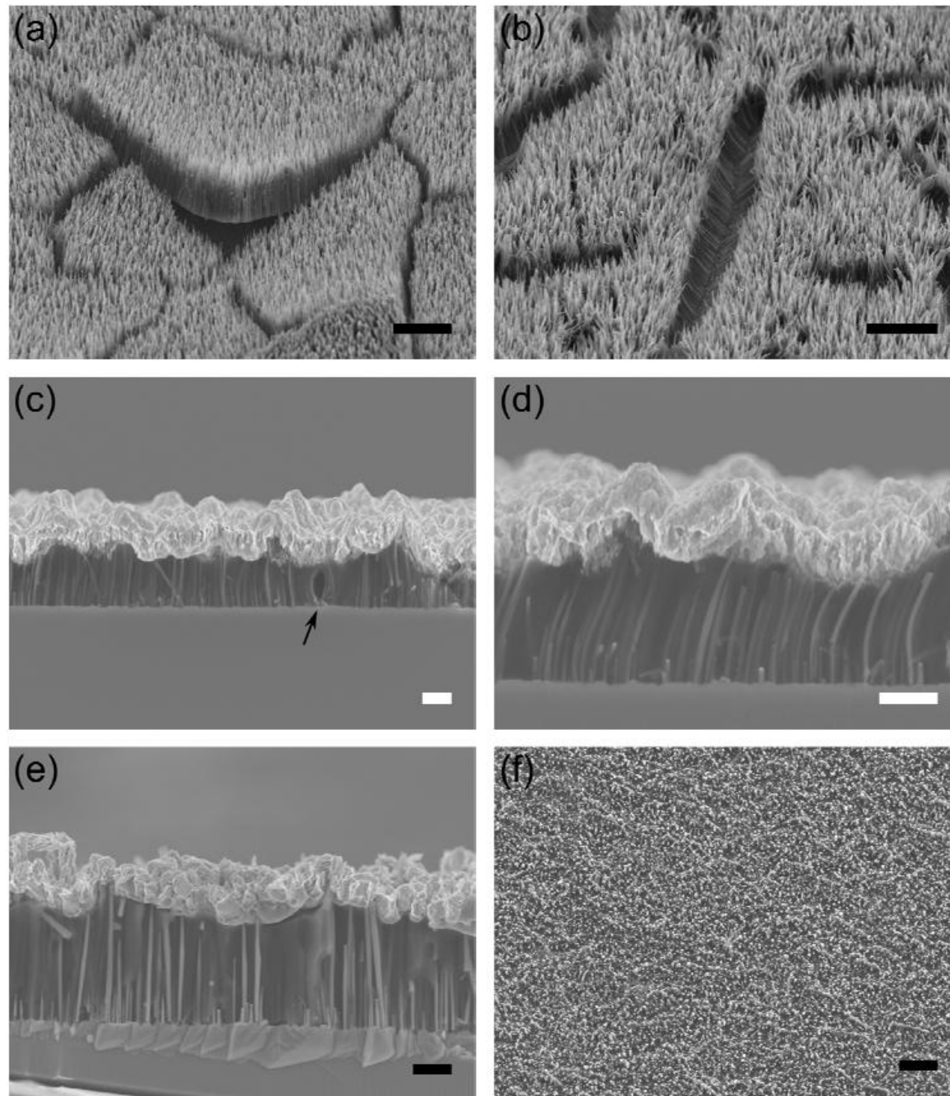

Figure 3.3: Post-anneal SEM images of (a) SC200 film showing severe cracking and delamination (45° tilt, 5 µm scale bar); (b) SU8 film showing major cracking at uncontacted areas (45° tilt, 5 µm scale bar); (c) SU8 film showing minor cracking under a contact pad as indicated by the arrow (90° tilt, 1 µm scale bar); (d) SU8 film showing bowing of the NWs under a contact pad (90° tilt, 1 µm scale bar); (e) Cyclotene exhibiting no bowing of the NWs under a contact pad (55° tilt, 1 µm scale bar) and (f) Cyclotene film exhibiting no cracking even at uncontacted areas (30° tilt, 5 µm scale bar).

contact pad planarized by SU8. It appears, therefore, that the top contact may help to prevent cracking in the case of SU8. These thermal stability results have also been summarized in Table 3.2.

After successful planarization of the NWs with SU8 and Cyclotene, the NWs were sonicated in water. From Figure 3.1c, it is clear that sonication successfully removed the tops of the NWs exposed above the polymer film, thus accomplishing two goals. Firstly, this completed the perfect planarization of the NW sample. Furthermore, sonication eliminated the Au seed particle at the top of the NWs that may be detrimental in some device applications (e.g., the Au particle can reflect light away from the NWs in a photovoltaic device). Secondly, it solved the previously reported problem of an open circuit occurring if photoresist covers the tops of the NWs [44]. Sonication ensures that the top of each NW is a freshly cleaved surface with no residual polymer on it. Previously, these goals have been achieved by chemical-mechanical polishing (CMP) [46,48]. However, sonication presents a more attractive alternative due to its simplicity, lower cost, better scalability and non-destructiveness in terms of potential delamination and cracking.

Next, RIE was examined as a method to selectively etch the polymer to a desired NW height. After sonication, the samples underwent RIE as shown in Figure 3.1d. RIE parameters were described in the Section 3.2. From a comparison of the SEM images in Figure 3.1c and Figure 3.1d, it is clear that the RIE successfully uncovered the top of the NWs for contacting as intended. SEM analysis found that the density of NWs protruding

out of both the SU8 and Cyclotene layers was about $5x10^{8}$ cm^{-2} thus amounting to about 25% of all NWs. This was found to be consistent with the height distribution of the NWs.

Finally, top and bottom contacts were deposited and subsequently annealed. Figure 3.1e shows that a planar top contact was successfully deposited, while the underlying Cyclotene maintained its structural integrity after annealing as mentioned earlier. Figure 3.3c shows an SEM image of NWs embedded in SU8 underneath a contact pad after annealing whereby only small cracks are present (indicated by the arrow in Figure 3.3c), unlike the regions between contact pads as shown in Figure 3.3b. Therefore, as previously hypothesized, the SU8 layer was thermally stable under a contact pad. However, it must be noted from Figure 3.3d that the NWs are bowed indicating substantial stress in the SU8 layer. However, neither this bowing nor the aforementioned small cracks were observed in the Cyclotene sample as shown in Figure 3.3e and Figure 3.3f. Consequently, only Cyclotene was chosen for subsequent I-V measurements.

Figure 3.4c shows the I-V measurements performed at different parts of the sample to assess the success of NW contacting. I-V characteristics were obtained from contact pads in three different locations (A, B, C) on the sample as depicted schematically in Figure 3.4a. The I-V analysis gave rise to four observations. Firstly, no differences in the I-V characteristics of the NWs (pad B) were observed whether the contact was deposited immediately after the sonication step or after the RIE etching

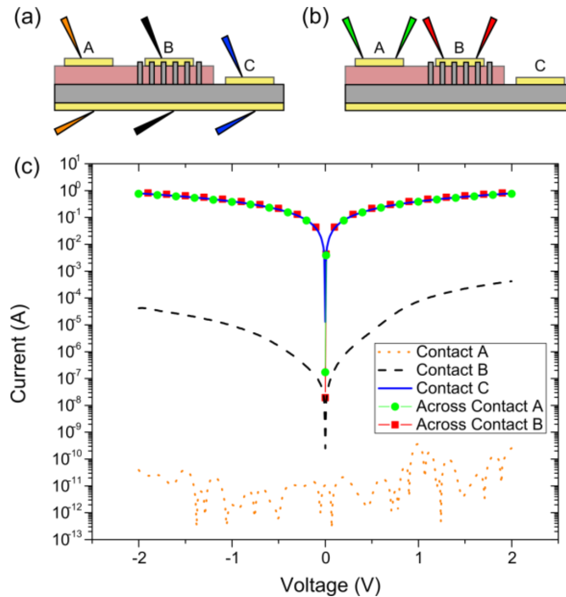

Figure 3.4: (a) Schematic of the three different top contacts deposited on the device with probes contacting the top and bottom of the device. (b) Schematic of the two-point probe measurement across contact pad A and B. (c) Semi-log plot of I-V characteristics between each top contact pad and the rear contact (pad A, pad B, pad C) as indicated in (a), and laterally across a single contact pad A and B as indicated in (b). The color of the probes in (a) and (b) correspond to the color of the curves in (c).

step described earlier, indicating that the RIE process was not detrimental to NW contacting. Secondly, the low current from the control contact A (orange dotted line) formed on the Cyclotene film with no NWs underneath yielded negligible current. This showed that Cyclotene is insulating and effectively isolates the top and bottom contacts. Thirdly, the current passing through contact B (black dashed line) on top of the NWs is more than 4 orders of magnitude higher than the current passing through contact A. By comparison with the I-V characteristics from pad A, the I-V characteristics from pad B indicated that conduction occurred through the NWs as opposed to the filling material. Fourthly, the high current (blue solid line) drawn by contact C on the substrate clearly

indicated the short circuited situation. When comparing the low resistance, linear I-V characteristics of contact A to the higher resistance I-V characteristics of contact B, it is clear that the NWs are not shunted, but exhibit less current possibly due to carrier depletion of the thin NWs. These depletion effects are also responsible for the rectifying nature of the I-V characteristics of pad B as compared to the linear characteristics of pads A and C. Further studies of these depletion effects are currently underway. In all, these three contacts show that the Cyclotene layer has successfully prevented both short circuits and open circuits, while permitting conduction through the NWs.

To further illustrate the effective planarization of the contact on top of the NWs, the sheet resistance of the NW contacts (pad B) were estimated by simple two-point probe measurements across the contact pad as depicted schematically in Figure 3.4b. Figure 3.4c shows the representative I-V characteristics across contact B (red squares). The two-probe resistance across the pad was found to be ~2Ω. I-V characteristics across contact A (green circles) yielded the same nominal two-probe resistance of ~2Ω across the pad. This indicates the deposition of a high quality top contact on the NWs. Additionally, further I-V measurements showed that this resistance was mainly attributed to the parasitic resistance of the measurement apparatus, indicating a negligible voltage drop across the contact pad. Therefore, planarization has been effective in creating a low sheet resistance contact on top of the NWs.

3.4 Conclusion

In conclusion, a consistent study of a variety of organic filling materials (S1808, SC200, SU8 and Cyclotene) was assessed for porosity, planarization and thermal stability. Qualitative analysis of the thermal stability and porosity along with quantitative analysis of the roughness of each filling material has shown that Cyclotene is best suited as an organic filling material. This analysis has in turn provided a set of standards by which future attempts at NW planarization can be judged. The novel method of removing the tops of the NWs by sonication proved to be effective in achieving complete planarization and thus stands as an attractive alternative to the conventional CMP method. Finally, a full device was successfully fabricated where the Cyclotene layer prevented both short circuits and open circuits while allowing the deposition of a low sheet resistance, planar top contact. In all, these processes and analysis can be easily repeated for future characterization and fabrication of ensemble NW devices.

4 Unlocking Doping and Compositional Profiles of Nanowire Ensembles using SIMS

4.1 Introduction

It is readily apparent that doping control in NWs is crucial in the realization of functional semiconductor optoelectronic devices. However, as discussed in Chapter 1.3, doping control is made difficult due to the lack of easy and precise methods of measuring or evaluating doping concentrations in NWs.

Electrical methods are the most common method of measuring doping concentrations in NWs [29]. In the most direct approach, the NW conductance is accurately calculated from current-voltage (I-V) measurements across a doped NW in a four-point probe configuration [53]. Using a surface depletion model, the impurity dopant concentration can be determined [54]. Similarly, NW field-effect transistors (FETs) can be fabricated and the transconductance accurately measured [55]. Using a gate capacitance model, the mobility can be calculated, allowing for the determination of impurity dopant concentration. While both approaches enable the precise quantification of the conductance or transconductance in the NW respectively, the models used to determine the impurity dopant concentration in the NW typically include many assumptions [29]. As such, electrical methods can only be used to give

estimations of the impurity dopant concentration. Similarly, optical methods (such as photoluminescence [56], Raman spectroscopy [57], transient terahertz photoconductivity [58] and photoconductivity [59]) and scanning probe methods (such as scanning photocurrent microscopy [60] and Kelvin probe force microscopy [61]) used to measure impurity dopant concentration offer only qualitative descriptions, not quantitative doping values [29].

Mass spectrometric methods provide the most direct means of precise, quantitative impurity dopant concentration measurement. Currently, the most powerful mass spectrometric method for determining impurity dopant concentration in NWs is pulsed laser atom probe tomography (APT) which provides excellent spatial resolution and low detection limits to allow for full three-dimensional arrangements of dopant atoms to be constructed [62]. However, pulsed laser APT is not without its share of complications. Firstly, characterization by APT requires NWs to be thin (less than 100nm in radius) and conductive to avoid sample fracture and overheating [63,64]. Secondly, APT's requirement for the NW tips to be separated from the substrate by 10-20 μm [63] and for individual NWs to be either isolated or separated from other NWs by large distances of ~400 μm [64] necessitates extensive sample preparation involving either the growth of NWs on isolated, predefined micropillars [64] or mounting individual NWs onto metal tips [65] or semiconductor micropillars [66] using focused ion beam (FIB) in conjunction with a nanomanipulator. Additional requirements including precise alignment of the local electrode, exact focusing of the laser light on the NW tip [64] and

optimizing voltage and laser pulse parameters for efficient field evaporation [63] add to the sophistication of this technique. Thirdly, the detection limit of APT is highly dependent on many sample-related parameters and is limited by counting statistics [66], thus casting doubt on its use for low dopant concentrations. Fourthly, it can be challenging to achieve crucial stoichiometric evaporation for a wide variety of compound semiconductors [67]. Finally, the relatively slow speed of APT characterization limits the throughput of characterized NWs [29].

Secondary-ion mass spectrometry (SIMS) is a logical alternative mass spectrometric method due to its standard use in thin film semiconductors. However, the use of SIMS with NWs has been limited due to its low lateral spatial resolution. Previous work has seen SIMS performed on a collection of NWs dispersed on a substrate [68], but this approach gives only the average doping concentration of the NWs with zero spatial resolution. To improve spatial resolution, NanoSIMS can be used instead, but NanoSIMS systems are not readily available and typically have a maximum spatial resolution of 50 nm, making it advantageous only for dispersed microwires [69]. One compromise is to utilize the high depth resolution of SIMS profiles by performing SIMS on vertically standing NW ensembles instead of on dispersed samples to probe how dopant concentrations change axially along the NW. However, a combination of the large analysis area of SIMS and the nonplanar geometry of the NW ensemble results in the background substrate and NWs being sputtered and analyzed simultaneously, thus allowing only an estimate of dopant concentrations [65]. As such, SIMS has only been

successful in determining trace impurities in NW ensembles dense enough such that the substrate is obscured by the NW ensemble [70] .

To address these issues, SIMS was performed on NW ensembles planarized with a filling medium. By embedding the NWs in a polymer, the top surface of the sample was made planar, while the background substrate was protected from the ion beam, thus allowing for precise dopant concentration quantification. This chapter was largely taken from our work published in Nanotechnology [35] and remains the first reported use of conventional SIMS to accurately determine the doping concentration with excellent axial resolution. Additionally, by performing SIMS on different NW ensembles, SIMS will be showcased as an invaluable tool for characterizing both the uniformity of NW heights and axial heterostructure segment lengths in NW ensembles.

4.2 Experimental Details

Using the vapor-liquid-solid (VLS) mechanism in a gas source molecular beam epitaxy (MBE) system, two NW ensemble samples were grown; an ensemble of GaAs homostructure NWs (Sample A) and an ensemble of axial GaAs/GaP heterostructure NWs (Sample B). For each sample, a GaAs (111)B substrate (Si doped for Sample A and Zn doped for Sample B with a doping concentration of ~10^{18} cm^{-3}) was prepared for growth by cleaning in UV ozone for 20 min, subsequently etching in buffered HF for 30 s and finally rinsing in deionized (DI) water for 10 min. 1 nm of Au was then deposited

onto each substrate via electron-beam evaporation to serve as the catalyst for VLS growth. Finally, each substrate was placed in the MBE system where several degassing and plasma cleaning steps were performed (described in detail in Chapter 2.2) to prepare for NW growth. All samples were grown with a V/III flux ratio of 2.3 and a two-dimensional (2D) equivalent growth rate of 0.5 μm/hr. For Sample A, the GaAs NWs were grown for 30 min at 600°C with Te (from a GaTe effusion cell) added during NW growth to achieve a nominal doping concentration of 10^{18} cm^{-3} as calibrated by previous thin film growths. For Sample B, base GaAs NW segments were grown for 15 min at 600°C, while subsequent upper GaP NW segments were grown for 10 min at 560°C. To ensure an abrupt hetero-interface, the Ga effusion cell was shuttered while As_2 was switched for P_2 and the temperature was adjusted for GaP growth. Each segment was doped from a Be effusion cell to achieve a nominal doping concentration of $5x10^{18}$ cm^{-3} as calibrated by previous thin film growths.

After growth, Cyclotene polymer was used to fill the space between NWs and planarize the top surface. Sample A was spin-coated with a 3:1 volume mixture of Cyclotene 3022-35 to T1100 thinner, while Sample B was spin-coated with pure Cyclotene 3022-35. Both samples were spin-coated for 60 s at 3000 RPM. Cyclotene was chosen due to its low surface roughness, low porosity and high thermal stability as reported in Chapter 3 [34]. The morphologies of NW ensembles were characterized using a JEOL JSM-7000F scanning electron microscope (SEM) before and after the Cyclotene spin-coat.

Finally, SIMS measurements were performed on Sample A, Sample B and thin film standards with similar doping concentrations using a Cameca IMS-3f Dynamic SIMS system and an ION-TOF TOF-SIMS IV Time-of-flight (TOF) system. For dynamic SIMS, both 10keV Cs^+ and 12.5keV O^+ primary ion beams were used to analyze a 60 µm-diameter circular area. For the TOF SIMS, a Bi^{3+} primary ion beam pulsed at 10 kHz was used to analyze a 50µmx50µm square area.

4.3 Results and Discussion

Figure 4.1a shows an SEM image of Sample A spin-coated with Cyclotene, highlighting two features. Firstly, Sample A exhibits a non-uniform height and diameter distribution typical of VLS-grown NWs. Sample A had a high NW density of 3×10^9 cm^{-2} and a corresponding areal density of 10%. Secondly, it is clear that the Cyclotene is successful at completely filling the void between the NWs, while producing a smooth, planar top surface ideal for subsequent SIMS characterization.

Dynamic SIMS was performed on sample A using a Cs^+ primary ion beam, resulting in a depth profile of sputtered negative secondary ions shown in Figure 4.1b. Multiplying the NW density by the SIMS analysis area, the total number of NWs within the analysis volume in Figure 4.1b was found to be 8×10^4 NWs. The carbon profile (magenta line) in Figure 4.1b results from the presence of the Cyclotene in the NW ensemble layer. While the C profile is not perfectly abrupt at the substrate-Cyclotene

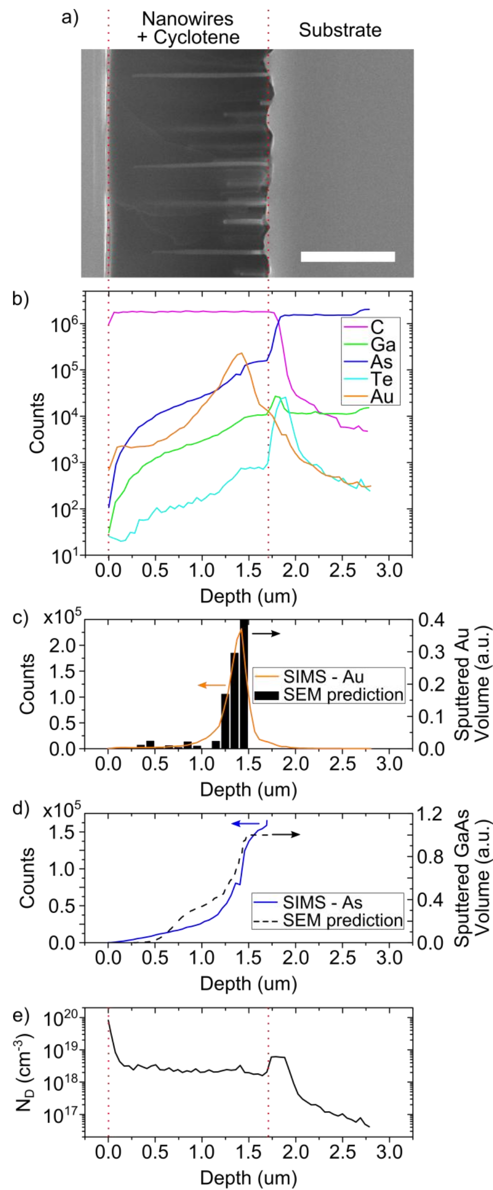

Figure 4.1: (a) Cross-sectional SEM image of Sample A spin-coated with Cyclotene. The scale bar is 1 µm. (b) Semi-log plot of the Sample A dynamic SIMS depth profile using a Cs^+ source. (c) Linear plot of the Au depth profile in contrast with SEM predictions. (d) Linear plot of the As profile in contrast with SEM predictions. (e) Semi-log plot of Te impurity concentration as a function of depth. The depth scale in (b)-(e) are scaled to (a). The vertical red dotted lines serve to demarcate the different regions of interest in the NW ensemble.

interface (1.7 µm depth) due to the roughness of the 2D film between the NWs, it still shows a high degree of abruptness as is apparent from Figure 4.1a.

The Au profile (orange line) in Figure 4.1b arises as the Au catalysts at the tops of the NWs are sputtered. Qualitatively, it is clear that the Au profile rises and falls gradually in Figure 4.1b due to the non-uniform height distribution of the NW ensemble. For quantitative analysis, the NW height versus Au diameter distribution from SEM analysis was used to calculate and plot the total Au catalyst volume as a function of depth in order to simulate the expected Au SIMS profile. Figure 4.1c shows this prediction plotted (black bars) in comparison to the Au SIMS profile from Figure 4.1b. It is clear that the Au profile traces the SEM predictions excellently.

The As profile (blue line) in Figure 4.1b arises as the bulk of the NWs are sputtered. Qualitatively, the gradual increase in As counts with increasing depth is consistent with increasing NW concentration near the substrate. Similar to the previous quantitative analysis, the NW height versus diameter distribution from SEM analysis was used in conjunction with a NW tapering analysis to calculate and plot the total GaAs NW volume as a function of depth in order to simulate the As SIMS profile. This prediction is plotted in comparison to the As profile in Figure 4.1d, where very close agreement is apparent. The excellent agreement between the SIMS profiles and SEM predictions in Figure 4.1c and Figure 4.1d further highlights the accuracy of SIMS analysis on NW ensembles.

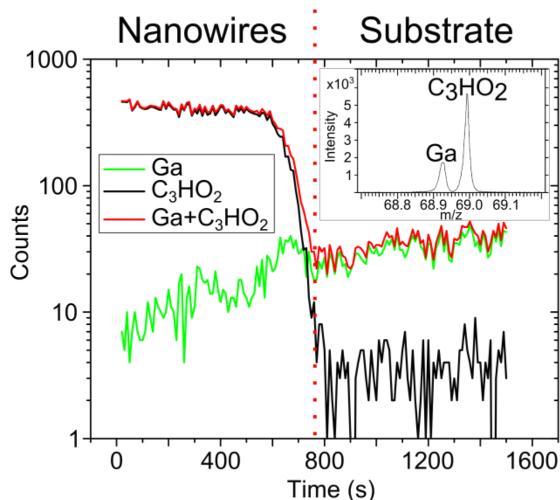

Figure 4.2: TOF-SIMS depth profile of Sample A. Inset: Mass spectrum indicating the presence of nearly equal mass C_3HO_2.

It must be mentioned that the Ga profile (green line) in Figure 4.1b, while showing the same trend as the As profile as expected, exhibits a non-physical artifact near the Cyclotene-substrate interface whereby the number of Ga counts is higher in the NWs than the film. This artifact can be explained by utilizing the superior mass resolution of TOF-SIMS to achieve an additional depth profile of Sample A as shown in Figure 4.2. This figure clearly shows the physical situation of a Ga profile from the film which steadily rises with increasing depth, but never exceeds the number of counts in the substrate. However, Figure 4.2 also shows the presence of an organic polymer, C_3HO_2, as a sputtering product of the Cyclotene surrounding the NWs. Due to its similar charge-to-mass ratio as Ga (m/z, see inset) coupled with the inferior mass resolution of dynamic SIMS, the Ga and C_3HO_2 counts are convoluted in Figure 4.1b, causing the Ga profile to be shifted up in the NW segment by a constant intensity from the C_3HO_2, thus

giving rise to the artifact near the Cyclotene-substrate interface. Furthermore, this issue is exacerbated by the low negative Ga ion yield when a Cs^+ primary ion beam is used [71]. It should be noted that this interference has been observed in other polymers such as SU8.

Finally, the Te profile (cyan line) in Figure 4.1b indicates the presence of intentional Te dopant atoms. Qualitatively, it can be observed that the Te profile follows the same trend as the As profile, thus giving good reason to expect the Te concentration to remain relatively constant as a function of depth. Quantitatively, the Te doping concentration of Sample A can be found using the equation:

$$N_D = \frac{I_{Te} / I_{As}}{I_{Te,std} / I_{As,std}} N_{D,std} \tag{4.1}$$

where I_{Te} is the intensity of Te counts from Sample A, I_{As} is the intensity of As counts from Sample A, $I_{Te,std}$ is the intensity of Te counts from a standard, I_{As} is the intensity of As counts from a standard and $N_{D,std}$ is the Te impurity concentration of the standard. A thin film GaAs sample with a Te dopant concentration of 5×10^{17} cm^{-3} was selected as the standard for SIMS quantification. Te-to-As ratios were selected over Te-to-Ga ratios for Eqn. (4.1) due to the aforementioned interference between Ga and C_3HO_2. Using Eqn. (4.1), the Te dopant concentration was calculated and plotted as a function of depth in Figure 4.1e, where it was confirmed that the Te concentration remained at a relatively constant value of 2×10^{18} cm^{-3} as a function of depth. This is in close agreement to the intended doping of 1×10^{18} cm^{-3}. Figure 4.1e also shows the Te concentration rising

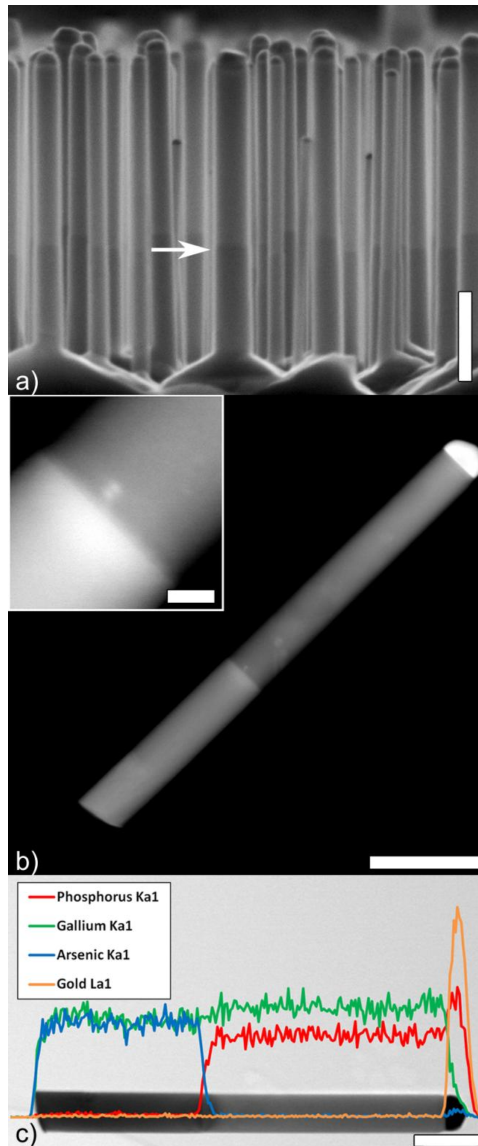

Figure 4.3: (a) Cross-sectional SEM image of Sample B with an arrow delineating the GaAs/GaP junction. The scale bar is 250 nm. (b) High angle annular dark field (HAADF) STEM image of a single NW from Sample B. The scale bar is 200 nm. Inset: Abrupt heterojunction at the GaAs/GaP interface. White marks in the GaP section indicate beam damage. The scale bar is 20 nm. (c) EDX linescan overlayed with a TEM image confirming the axial GaAs/GaP heterostructure. The scale bar is 100 nm.

drastically at the Cyclotene-film interface. This is likely due to Te segregation on the film surface due to the surfactant effects of Te [72,73]. It should be noted that this SIMS analysis only provides a depth profile of the dopant concentration, not the lateral dopant profile across the NW diameter; hence, a similar segregation of Te may exist in the NWs.

Although Figure 4.1e is generated accurately by Eqn (4.1), it only gives a measure of the doping profile averaged at different relative axial positions for different NWs of varying heights. As such, it still does not give a true representation of the axial distribution of dopant atoms. To achieve this, a NW ensemble with uniform height NWs is needed, thus providing motivation for the SIMS characterization of Sample B.

Sample B exhibits two features as shown in Figure 4.3a. Firstly, the ensemble is exceptionally uniform in height. This has been observed elsewhere as a result of the Be doping [74]. Sample B had a high NW density of 10^9 cm^{-2} and a corresponding areal density of 6%. Secondly, the GaAs and GaP segments are visible as contrast in Figure 4.3a where it is seen that both the lower GaAs and upper GaP segments are uniform in height throughout the ensemble. Scanning transmission electron microscope (STEM) analysis of a single NW in Figure 4.3b confirms a very abrupt heterojunction in each NW, while energy dispersive x-ray spectroscopy (EDX) analysis of a single NW in Figure 4.3c confirms the GaAs/GaP axial heterostructure. As with Sample A, Sample B was successfully filled and planarized using Cyclotene as shown in Figure 4.4a. Sample B was analyzed using both Cs^+ and O^+ primary ion beams to gain a comprehensive dataset.

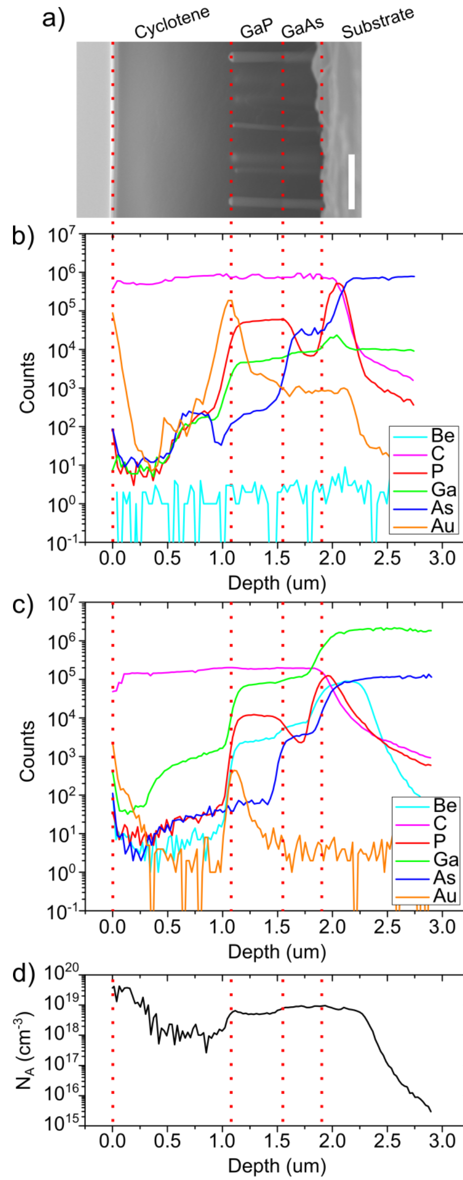

Figure 4.4: (a) Cross-sectional SEM image of Sample B spin-coated with Cyclotene. The scale bar is 500 nm. (b) Semi-log plot of the Sample B dynamic SIMS depth profile using a Cs+ source. (c) Semi-log plot of the Sample B dynamic SIMS depth profile using an O+ source. (d) Semi-log plot of Be impurity concentration as a function of depth. The depth scale in (b)-(d) are scaled to (a). The vertical red dotted lines serve to demarcate the different regions of interest in the NW ensemble.

With the Cs^+ source, the negative secondary ion yield is high for Au, P and As, enabling the height uniformity analysis of the NWs and individual axial segments from depth profiles (Figure 4.4b). Conversely, the O^+ source produces a high positive secondary ion yield for Be and Ga, allowing the Be doping concentration to be determined from depth profiles (Figure 4.4c). The total number of NWs within the analysis volume in Figure 4.4b was found to be 3×10^4 NWs.

From the Cs^+ source depth profile in Figure 4.4b, it is clear that the leading edge of the Au peak (orange line) in Sample B is much sharper than that of Sample A (Figure 4.1b). Quantitatively, the FWHM of the Au peak in Sample B is ~90 nm versus a FWHM of ~230 nm in sample A. This is reflective of the excellent height uniformity in Sample B. The high Au counts at the surface of the Cyclotene is due to Au deposition on the Cyclotene to prevent charging. Sharp leading edges can also be observed for the P and As profiles (red and blue lines respectively) at approximate depths of 1.1 µm and 1.5 µm respectively. This confirms the height uniformity of the NW ensemble. Additionally, Figure 4.4b confirms the height uniformity of the individual GaAs and GaP segments and, furthermore, identifies that the heterojunction is located near a depth of ~1.5 µm.

In Figure 4.4c, the Ga profile is unlike those from Figure 4.1b and Figure 4.4b, in that the Ga intensity does not exceed that of the film near the Cyclotene-substrate interface. Although C_3HO_2 still exists and interferes with the Ga intensity, its contribution to the total Ga intensity is small because of the high positive Ga ion yield

with the O^+ primary ion beam. As such, the Ga profile was used to calculated the doping concentration as per:

$$N_A = \frac{I_{Be} / I_{Ga}}{I_{Be,std} / I_{Ga,std}} N_{A,std} \tag{4.2}$$

where I_{Be} is the intensity of Be counts from Sample B, I_{Ga} is the intensity of Ga counts from Sample B, $I_{Be,std}$ is the intensity of Be counts from a standard, I_{Ga} is the intensity of Ga counts from a standard and $N_{A,std}$ is the Be impurity concentration of the standard. A thin film GaAs sample with a Be impurity concentration of 9×10^{18} cm^{-3} was selected as the standard for SIMS quantification. Using Eqn. (4.2), the Te impurity concentration was calculated and plotted as a function of depth in Figure 4.4d in close agreement with the intended doping of 5×10^{18} cm^{-3}across the GaAs and GaP segments. The calculated doping concentration in the GaP segment is only an estimate since a Be-doped GaP standard was not available. Additionally, the Be impurity concentration may be slightly overestimated due to possible cascade mixing of the Be from the GaP segment, but this should represent a small contribution to the increased Be intensity in the GaAs segment.

Next, we address several SIMS-related issues. First, we examined whether the sputtering rate was uniform across the sputtered region; i.e., there was no difference in sputtering rate between the NWs and the surrounding Cyclotene, and the NWs were being sputtered in a planar fashion. SEM analysis (not shown) was performed at the bottom of the crater formed in sample B after either Cs- or O-sputtering to a depth of approximately 1 µm (i.e., near the GaAs/GaP heterointerface). The SEM analysis

indicated a smooth surface in the crater bottom with no discernible roughness, indicating equal sputter rates between the NWs and Cyclotene and thus confirming excellent depth resolution.

Secondly, Eqns (4.1) and (4.2) assume that the secondary ion yields for dopant atoms remain unchanged between the thin film standard and Sample A and B. One common situation in which this assumption may be invalid occurs due to the matrix effect whereby the secondary ion yields are affected by the chemical matrix within which the dopant is situated. In this work, the physical matrix of Sample A and B (GaAs NWs embedded in polymer) is different from the physical matrix of the thin film standard (pure GaAs crystal). Nevertheless, from the reference point of the dopant atoms, their surrounding chemical matrix is the same for both the thin film standards and Sample A and B, thus avoiding the matrix effect. This analysis, however, still ignores the role played by ion beam mixing in changing the chemical matrix. Considering ion beam mixing of Cyclotene into GaAs, the matrix effect will be present along the NW sidewalls throughout the entire length of the depth profile for Sample A and B, while being only present at the planar Cyclotene-GaAs interface in the thin film standard and being absent in the bulk of the thin film standard. This weakens the aforementioned assumption of unchanging secondary ion yield between the thin film standards and Sample A and B.

To ascertain the extent of the matrix effect in the NWs due to ion beam mixing, the depth of the ion beam mixing region along the GaAs NW sidewalls was estimated.

Using SRIM 2013 software [75], a Monte-Carlo simulation was performed for 10 keV Cs^+ primary ions impinging on GaAs covered with Cyclotene. Similar simulations were performed for 12.5 keV O^+ primary ions. For each primary beam type, the Cyclotene thickness was varied from 1 nm up to a thickness corresponding to the maximum penetration depth of the primary beam (20nm for Cs^+ and 60nm for O^+). For the Cameca IMS-3f system used in our studies, the angle of incidence of the primary ion beam relative to the sample surface is 30°. The angle of incidence of the primary ion beam in the simulations was chosen as the complementary angle (60°), corresponding to the greatest angle of incidence of the ion beam on the nanowire sidewall surfaces. From these simulations, it was found that the distribution of constituent Cyclotene ions (C, H, O, Si and N) mixed into the GaAs had a mean penetration depth ranging from 1.4 nm to 3 nm. This corresponding to a full ion beam mixing region (wherein 95% of Cyclotene ions are absorbed) extending between 4 nm and 12nm. For this work, since average radii of NWs in Sample A and B (34 nm and 32 nm respectively) are considerably larger than the ion beam mixing region, the contribution of the matrix effect to total secondary ion yield should be minimal. Nonetheless, this extent of the ion beam mixing region imposes a size limitation on this technique. This size limitation can potentially be overcome by either lowering the energy of the primary ion beam or replacing the thin film standard with a NW ensemble fabricated by reactive ion etching [76].

Having accounted for systematic uncertainties such as the matrix effect, the dopant concentration detection limit for NWs is merely the detection limit for films divided by the areal density of NWs. Since typical NW ensembles have areal densities of approximately 10%, the detection limit for NWs is typically degraded by an order of magnitude. Additionally, there exists a slight instrumental error on the order of several percent depending on the stability of the primary ion beam and lens voltages. However, this error is likely to have a small contribution to the overall uncertainty compared to the aforementioned matrix effects. Nevertheless, the authors concede that further study is required to increase the accuracy of dopant concentration quantification in ensemble NWs.

4.4 Conclusion

In conclusion, it is clear that SIMS is a valuable tool for two purposes: characterizing height uniformity in a NW ensemble and determining impurity dopant concentration in the NWs. Pertaining to its use in characterizing NW ensemble uniformity, SIMS provides a useful tool of measuring height uniformity in an ensemble without the need to manually process SEM images. Moreover, SIMS is able to characterize the segment height uniformity of any arbitrary axial heterostructure NW ensemble. Additionally, this concept can be extended to measure the dispersion in the

location of a junction in an axial homostructure (e.g. an axial p-n junction NW). This is particularly valuable when forming planar top contacts to ensemble NW devices [34].

Finally, SIMS has also been demonstrated to be both a simple and accurate method of determining dopant impurity concentrations. In contrast to APT, SIMS provides an excellent complementary tool. The strengths of SIMS include being a more accessible and relatively unsophisticated technique, while boasting a higher throughput desirable for NW ensembles, fewer systematic uncertainties (such as stoichiometric evaporation), fewer sample preparation requirements and a lower detection limit by analyzing multiple NWs to avoid problems with counting statistics. However, weaknesses of SIMS include the lack of three-dimensional resolution, the requirement for a dense ensemble of nearly identical NWs, the inability to perform dopant mapping and a NW size limitation due to ion beam mixing. In conclusion, this development of SIMS on NW ensembles can be used in conjunction with surface depletion and gate capacitance models to gain a comprehensive understanding of NW electrostatic characteristics, marking a crucial step towards the engineering of complex doping and compositional profiles in NWs for novel devices.

5 Analytical Model of Surface Depletion in Nanowires

5.1 Introduction

Surface effects such as surface depletion have been shown to have a significant detrimental effect on the performance of NW devices as described in Chapter 1.3. However, little theory has been published on surface depletion in NWs, thus necessitating a thorough theoretical understanding of NW surface depletion.

To better understand the extent of deleterious surface depletion, a model is required to solve Poisson's equation. The model presented by Schmidt et al. [77] provides a solution to Poisson's equation along with comprehensive, analytical expressions for various nanowire parameters, but fails to satisfy the boundary conditions for the situation when a NW is not fully depleted. A subsequent model presented by Simpkins et. al. [78] provides a full solution to Poisson's equation which satisfies all boundary conditions, but does not apply when the NW is fully depleted and does not relate the density of surface states to the final solution. As such, there is a need for both an accurate and complete surface depletion model, which will be provided in this chapter. This chapter was largely taken from our work published in the Journal of Applied Physics [36].

5.2 Theory

Similar to previous studies [77,78], NW surface depletion is modeled by solving Poisson's equation in cylindrical coordinates. Invoking the symmetry of a long NW, Poisson's equation can be simplified to an ordinary differential equation in r, the radial distance:

$$\frac{\partial^2\psi}{\partial r^2}+\frac{1}{r}\frac{\partial\psi}{\partial r}=-\frac{\rho}{\varepsilon} \tag{5.1}$$

where ψ is the electric potential, ρ is the net bulk charge density and ε is the permittivity of GaAs. A list of symbols can be found in Table 5.1. In general, the solution to this equation is given by [78]:

$$\psi(r)=-\frac{\rho}{4\varepsilon}r^2+C_1\ln(r)+C_2 \tag{5.2}$$

where C_1 and C_2 are constants.

To find C_1 and C_2, both Neumann and Dirichlet boundary conditions must be imposed on Eqn. (5.2):

$$\psi(r_q)=\psi_0 \tag{5.3}$$

$$\left.\frac{d\psi(r)}{dr}\right|_{r=r_q}=0 \tag{5.4}$$

where r_q is the radius of the quasi-neutral core region of the NW as shown in Figure 5.1 and ψ_0 is the potential at the centre of the NW (along the NW axis). Eqn. (5.3) merely

Table 5.1: List of symbols

Symbol	Description	Units
ψ	Electric potential	V
r	Radial distance (in cylindrical coordinates)	cm
ε	GaAs permittivity	F/cm
r_q	Radius of the quasi-neutral core region	cm
ψ_0	Potential at the centre of the NW	V
a	NW radius	cm
ρ_g	Net charge density in the space charge region	C/cm^3
$F_{1/2}$	Fermi-Dirac integral	-
ψ_s	Surface potential	V
D_{it}	Density of interface states at the GaAs/air interface	$cm^{-2}eV^{-1}$
Q_{it}	Interface charge density at the GaAs/air interface	cm^{-2}
E_g	Energy bandgap	eV
ψ_{CNL}	Charge neutrality level (CNL)	V
Δ	Potential difference between the CNL and intrinsic level	V
μ_n	Electron mobility	$cm^2V^{-1}s^{-1}$
μ_p	Hole mobility	$cm^2V^{-1}s^{-1}$
L	NW length	cm
σ_{eff}	NW effective conductivity	S/cm
σ_{rel}	NW conductivity relative to bulk	-

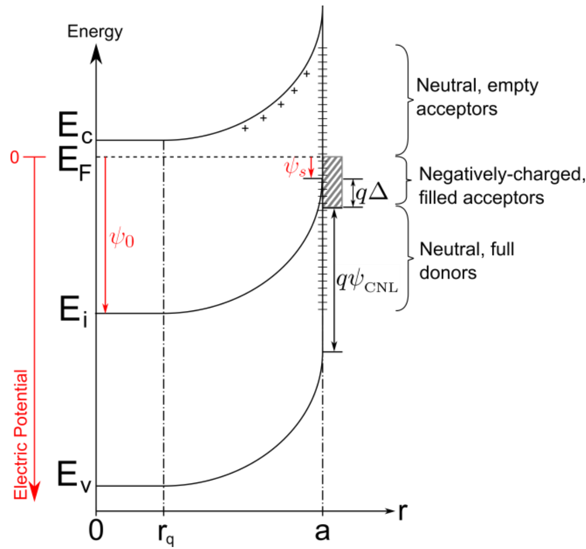

Figure 5.1: Band diagram along the cross-section of a NW

states that at $r = r_q$, the potential is given by the constant, ψ_0, as is evident from the equipotential quasi-neutral region between $r = 0$ to $r = r_q$ in Figure 5.1. From this figure, it is clear that $\psi(r)$ is defined to be the potential difference between the radially changing intrinsic level, E_i, and the constant Fermi level, E_f, where the potential is set at zero. Eqn. (5.4) merely states that at $r = r_q$, the radial component of the electric field is zero which is a necessary requirement at steady state.

5.2.1 Partially Depleted Regime: $\mathbf{r_q > 0}$

By substituting the boundary conditions from Eqns. (5.3) and (5.4) into Eqn. (5.2), C_1 and C_2 can be found and subsequently yield:

$$\psi(r) = \frac{\rho r_q^2}{2\varepsilon}\left[-\frac{r^2}{2r_q^2} + \ln\left(\frac{r}{r_q}\right) + \frac{1}{2}\right] + \psi_0 \tag{5.5}$$

Upon close examination, it can be immediately seen that this solution does not hold for a fully depleted NW (i.e. $r_q = 0$) since the $\ln\left(\frac{r}{r_q}\right)$ term is undefined. This special situation in the fully depleted regime where $r_q = 0$ will be analyzed later. However, Eqn. (5.5) gives a general expression of the potential in a NW in the partially depleted regime where $r_q > 0$. To explicitly find this potential, ρ, ψ_0 and r_q must be found. An expression for ρ will first be found.

5.2.1.1 Determination of ρ

In general, the charge density in the NW, $\rho(r)$, can be given as

$$\rho(r) = q\left[p(r) - n(r) + N_D^+ - N_A^-\right] \tag{5.6}$$

where q is the elementary charge, $p(r)$ is the free hole carrier density, $n(r)$ is the free electron carrier density, N_D^+ is the ionized donor doping density and N_A^- is the ionized acceptor doping density. In the quasi-neutral region of the NW between $r = 0$ and $r = r_q$, $n = N_D^+$ and $p = N_A^-$, thus making $\rho = 0$. Conversely, in the space charge region (SCR) between $r = r_q$ and $r = a$ of an n-type NW (i.e. $n, N_d^+ >> p, N_A^-$), the full depletion approximation (i.e. $n << N_D^+$) and complete ionization assumption (i.e. $N_D = N_D^+$) result

in a SCR charge density of $\rho = qN_D$. Therefore, the overall charge density in the NW can be written as

$$\rho = \begin{cases} 0 & \text{for} \quad 0 < r < r_q \\ qN_D \equiv \rho_g & \text{for} \quad r_q < r < a \end{cases} \tag{5.7}$$

where a is the radius of the GaAs core. Substituting Eqn. (5.7) into Eqn. (5.5) gives

$$\psi(r) = \begin{cases} \psi_0 & \text{for} \quad 0 < r < r_q \\ \psi_0 + \dfrac{\rho_g r_q^2}{2\varepsilon}\left[-\dfrac{r^2}{2r_q^2} + \ln\left(\dfrac{r}{r_q}\right) + \dfrac{1}{2}\right] & \text{for} \quad r_q < r < a \end{cases} \tag{5.8}$$

With an expression for ρ determined, an expression for ψ_0 is required as follows.

5.2.1.2 Determination of ψ_0

Typically, the Boltzmann approximation can be used to calculate the Fermi-level position based on the free carrier density. However, for high doping concentrations, as is typically the case for many NW device applications, the Boltzmann approximation is not entirely valid at all radii. In general, the free electron and hole concentrations are given by

$$n(r) = \frac{2}{\sqrt{\pi}} N_c F_{1/2}(\eta_F) \tag{5.9}$$

$$p(r) = \frac{2}{\sqrt{\pi}} N_v F_{1/2}(\eta'_F) \tag{5.10}$$

where $F_{1/2}(\eta)$ is the Fermi-Dirac integral given by

$$F_{1/2}(\eta) = \int_0^\infty \frac{x^{1/2}}{\exp(x-\eta)+1} dx \tag{5.11}$$

$$\eta_F = \frac{E_F - E_C}{kT} = \frac{q\psi(r) - E_g/2}{kT} \tag{5.12}$$

$$\eta_F' = \frac{E_V - E_F}{kT} = \frac{-\left(q\psi(r) + E_g/2\right)}{kT} \tag{5.13}$$

where N_c is the effective density of states in the conduction band, N_v is the effective density of states in the valence band, E_g is the energy bandgap, k is the Boltzmann constant and T is the temperature. The Fermi-Dirac integral cannot be solved analytically, but can be approximated by [79]:

$$F_{1/2}(\eta) \approx \frac{1}{2}\sqrt{\pi}\left\{\frac{3}{4}\sqrt{\pi}\left[\alpha(\eta)\right]^{-3/8} + e^{-\eta}\right\}^{-1} \tag{5.14}$$

where

$$\alpha(\eta) = \eta^4 + 33.6\eta\left\{1 - 0.68\exp\left[-0.17(\eta+1)^2\right]\right\} + 50 \tag{5.15}$$

Since $r_q > 0$, the centre of the NW is part of the quasi-neutral region of the NW and $\rho = 0$. If the NW is doped n-type and complete ionization is assumed, Eqn. (5.6) reduces to

$$\frac{2}{\sqrt{\pi}} N_c F_{1/2}(\eta_{F0}) = N_D \tag{5.16}$$

where η_{F0} is the value of η_F in the centre of the NW:

$$\eta_{F0}(\psi_0) = \left.\frac{E_F - E_C}{kT}\right|_{centre} = \frac{q\psi_0 - E_g/2}{kT} \tag{5.17}$$

Substituting Eqns. (5.14), (5.15) and (5.17) into Eqn. (5.16) yields a transcendental equation that can be solved to determine ψ_0. At this point, with ψ_0 and ρ determined, an expression for r_q is the last requirement to provide a full expression of $\psi(r)$.

5.2.1.3 Determination of r_q

r_q can be found by examining the potential at the surface $\psi_s = \psi(r=a)$. According to Eqn. (5.8),

$$\psi_s = \frac{\rho_g r_q^2}{2\varepsilon}\left[-\frac{a^2}{2r_q^2} + \ln\left(\frac{a}{r_q}\right) + \frac{1}{2}\right] + \psi_0 \tag{5.18}$$

From this equation, r_q (or correspondingly the depletion width, defined as $w = a - r_q$) can only be found if ψ_s is known. Alternatively, ψ_s can also be calculated precisely and independently by examining the surface charge and invoking charge neutrality. The charge neutrality level (CNL) of GaAs is $\psi_{\mathrm{CNL}} = 0.53$ V [80]. If a variable Δ is defined as $\Delta = \frac{E_g}{2q} - \psi_{\mathrm{CNL}} = 0.18\mathrm{V}$, the surface charge will then be given by

$$Q_{it} = -q \int_{E_i - q\Delta}^{E_i + q\psi_s} D_{it}\, dE \tag{5.19}$$

where D_{it} is the density of interface states at the GaAs/air interface. This equation makes the approximation that all interface states lying below the Fermi level are filled. Assuming that D_{it} is uniform between $E_i - q\Delta$ and $E_i + q\psi_s$,

$$Q_{it} = -q^2 D_{it}(\psi_s + \Delta) \quad (5.20)$$

Charge neutrality states that the sum of all bulk and surface charges in the system is zero:

$$\pi(a^2 - r_q^2)\rho_g + 2\pi a Q_{it} = 0 \quad (5.21)$$

Substituting Eqn. (5.20) into Eqn. (5.21) gives

$$\psi_s = \frac{(a^2 - r_q^2)\rho_g}{2aq^2 D_{it}} - \Delta \quad (5.22)$$

Eqn. (5.22) can be substituted into Eqn. (5.18) to yield the transcendental equation in r_q

$$\frac{(a^2 - r_q^2)\rho_g}{2aq^2 D_{it}} - \Delta = \frac{\rho_g r_q^2}{2\varepsilon}\left[-\frac{a^2}{2r_q^2} + \ln\left(\frac{a}{r_q}\right) + \frac{1}{2}\right] + \psi_0 \quad (5.23)$$

Eqn. (5.23) can be solved numerically to yield r_q. However, this equation cannot be solved for all a values. For a defined set of N_D and D_{it} values, there exists a certain critical GaAs NW radius, a_{crit}, for which the NW is fully depleted (i.e. $r_q = 0$). To find a_{crit}, Eqn. (5.23) can be solved in the limit as r_q approaches 0. For $a > a_{crit}$, r_q is given by the solution to the transcendental equation in Eqn. (5.23). Conversely, for $a < a_{crit}$, $r_q = 0$, which is the case treated in Section 5.2.2 below. With ρ, ψ_0 and r_q determined, a full expression of the potential in a partially depleted NW ($r_q > 0$) can be determined for a wide variety of D_{it}, a and N_D values.

5.2.2 Fully Depleted Regime: $r_q = 0$

As mentioned previously, Eqn. (5.5) does not hold in the fully depleted regime where $r_q = 0$ because this would cause the $\ln\left(\frac{r}{r_q}\right)$ term to be undefined. As a result, C_1 and C_2 in Eqn. (5.2) must be found again subject to different boundary conditions. Since $r_q = 0$, the Dirichlet and Neumann boundary conditions assume that $E = 0$ and $\psi = \psi_0'$ at the centre of the NW (at r = 0) due to the symmetry of the NW:

$$\psi(0) = \psi_0' \tag{5.24}$$

$$\left.\frac{d\psi(r)}{dr}\right|_{r=0} = 0 \tag{5.25}$$

Previously, the potential at the NW centre was given by ψ_0 and calculated on the basis of $n = N_D^+$ for the quasi-neutral region at $r = 0$. However, since the entire NW is depleted in this case, $n \neq N_D^+$ and the potential at the NW centre differs from the bulk case and is thus denoted as ψ_0'. By substituting the boundary conditions from Eqns. (5.24) and (5.25) into Eqn. (5.2), C_1 and C_2 can be found to yield:

$$\psi(r) = \psi_0' - \frac{\rho}{4\varepsilon} r^2 \quad \text{for} \quad 0 < r < a \tag{5.26}$$

This expression is valid provided that $a < a_{crit}$. To explicitly find this potential, ρ and ψ_0' must be found. An expression for ρ will first be found.

5.2.2.1 *Determination of* ρ

Using the same arguments as before, the charge density is identical to that given by Eqn. (5.7). Since $r_q = 0$, the charge density is given explicitly as $\rho = qN_D = \rho_g$ for all r . Substituting this into Eqn. (5.26) gives

$$\psi(r) = \psi_0' - \frac{\rho_g}{4\varepsilon} r^2 \quad \text{for} \quad 0 < r < a \tag{5.27}$$

With an expression for ρ determined, an expression for ψ_0' is required.

5.2.2.2 *Determination of* ψ_0'

In this case, ψ_0' can be found by examining ψ_s again, using the same approach as that taken earlier to find r_q. According to Eqn. (5.27),

$$\psi_s = \psi_0' - \frac{\rho_g}{4\varepsilon} a^2 \tag{5.28}$$

This surface potential can be found independently by examining the surface charge and invoking charge neutrality to yield the same equation as Eqn. (5.22), but with $r_q = 0$:

$$\psi_s = \frac{a\rho_g}{2q^2 D_{it}} - \Delta \tag{5.29}$$

Eqn. (5.29) can be substituted into Eqn. (5.28) to give ψ_0' as:

$$\psi_0' = \frac{a\rho_g}{2q^2 D_{it}} - \Delta + \frac{\rho_g}{4\varepsilon} a^2 \tag{5.30}$$

With ρ and ψ_0' determined, a full expression of the potential in a fully depleted NW can now be given explicitly for a wide variety of D_{it}, a and N_D values.

5.2.3 Effective free carrier concentration and conductivity

In order to extract relevant electrical properties, the free electron and hole densities, $n(r)$ and $p(r)$, can be found by substituting the model-generated $\psi(r)$ solutions from Eqns. (5.5) and (5.27) into Eqns. (5.9)-(5.15). Effective free carrier densities then can be found by integrating $n(r)$ and $p(r)$ across the entire radius of the NW:

$$n_{\text{eff}} = \frac{1}{\pi a^2}\int_0^a n(r)2\pi r dr \qquad (5.31)$$

$$p_{\text{eff}} = \frac{1}{\pi a^2}\int_0^a p(r)2\pi r dr \qquad (5.32)$$

For a NW of arbitrary length, L, the conductance of a shell of radius r and infinitesimal thickness *dr* is given by

$$dG(r) = q\left[\mu_e n(r) + \mu_p p(r)\right]\frac{2\pi r dr}{L} \qquad (5.33)$$

where μ_e is the electron mobility, μ_p is the hole mobility. Thus, the conductance of this NW can be found by integrating with respect to radius to yield a NW conductance of:

$$G = \frac{\sigma_{\text{eff}}\pi a^2}{L} \qquad (5.34)$$

whereby the effective conductivity of the NW is defined as

$$\sigma_{\text{eff}} \equiv q(\mu_e n_{\text{eff}} + \mu_p p_{\text{eff}}) \tag{5.35}$$

To compare this to the bulk, a relative conductivity defined as $\sigma_{\text{rel}} \equiv \sigma_{\text{eff}} / \sigma_{\text{bulk}}$ can be calculated whereby σ_{bulk} is the conductivity of bulk GaAs with the equivalent doping density.

5.3 Results and Discussion

In general, all aforementioned parameters are uniquely determined by three independent variables: a, D_{it} and N_D.

5.3.1 Model Output versus D_{it}

Figure 5.2 shows the model predictions for the variation of the key parameters with D_{it} for a typical $N_D = 10^{18}$ cm^{-3}. D_{it} can range from 10^{13} to 10^{14} cm^{-2}eV^{-1} for untreated GaAs $\{100\}$ surfaces of thin films, [81–83] while precise quantification of D_{it} for NW sidewall facets has been largely unexplored. Hence, Figure 5.2 has been plotted over a large range of possible D_{it} values. Figure 5.2a shows a_{crit} (solid black line) constantly increasing with increasing D_{it} until it asymptotically approaches the critical radius, a_{crit} = 51 nm, when the Fermi-level is pinned at the CNL as per Eqns. (5.22) and (5.29). It is apparent that even for highly doped NWs, D_{it} must be minimized by

passivation to avoid full depletion of a nanowire of typical dimensions. Surface passivation of NWs has been observed with the use of sulphur [84], InGaP [85], AlGaAs [58,86,87] and AlInP [88] passivation layers.

Figure 5.2a-c also examines parameters for two arbitrary NW radii of $a = 35$ nm (blue lines) and $a = 60$ nm (red lines). In particular, Figure 5.2a plots r_q as a function of D_{it}. At $a = 60$ nm, $a > a_{crit}$ for all D_{it} values and the NW is in the partially depleted regime. As such, r_q (red dashed line) is determined by Eqn. (5.23) and starts at $r_q \approx a$ for small D_{it} values, while asymptotically approaching 17 nm for increasing D_{it} values without becoming fully depleted. Conversely, at $a = 35$ nm, $a_{crit} = a$ at a defined critical interface state density, $D_{it} = D_{crit} = 3.5 \times 10^{12}$ cm^{-2} eV^{-1}, at which point the NW transitions between the fully and partially depleted regimes. For $D_{it} < D_{crit}$, the NW is in the partially depleted regime and r_q (blue dashed line) is determined from Eqn. (5.23). For $D_{it} > D_{crit}$, the NW is in the fully depleted regime and $r_q = 0$.

In Figure 5.2b, ψ_s is plotted according to Eqn. (5.22). As expected, ψ_s for $a = 35$ nm (dashed blue line) decreases more rapidly with increasing D_{it} than ψ_s for $a = 60$ nm (dashed red line) due to its larger surface area to volume ratio. As per Eqn. (5.22), ψ_s for both NWs asymptotically approaches $-\Delta = -0.18$ V for increasing D_{it}. This is consistent with Fermi level pinning at the CNL in the limit of D_{it} approaching

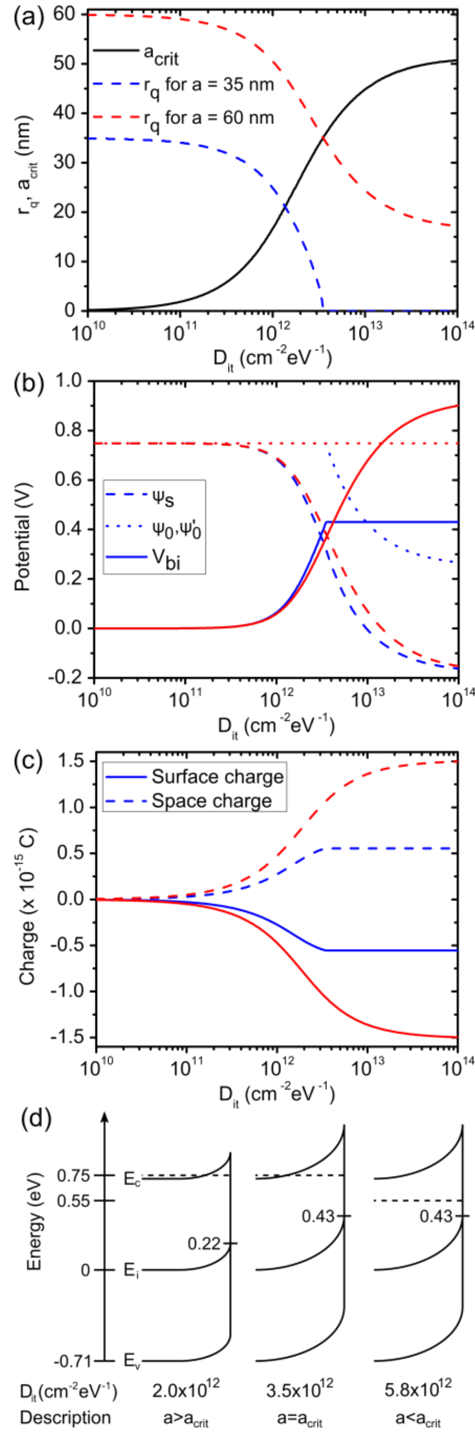

Figure 5.2: Model predictions of (a) a_{crit}, r_q, (b) ψ_s, ψ_0, V_{bb}, (c) surface charge, space charge and (d) energy band diagrams versus D_{it}. $N_D = 10^{18}$ cm $^{-3}$ for all plots. Blue lines indicate a = 35 nm and red lines indicate a = 60 nm. The energy band diagrams apply to a = 35 nm.

infinity [80]. ψ_0 is also plotted in Figure 5.2b, showing a marked difference in behaviour between $a = 35$ nm and $a = 60$ nm. Since $a = 60$ nm NWs are always in the partially depleted regime as per Figure 5.2a, the potential at the centre of the NW (dotted red line) is always a constant given by ψ_0 from Eqn. (5.16). However, for $a = 35$ nm, there exists a regime transition at $D_{it} = D_{crit}$. For $D_{it} < D_{crit}$, the potential at the centre of the NW (dotted blue line) is ψ_0 given by the solution to Eqn. (5.16) and equal to that of the $a = 60$ nm NW . For $D_{it} > D_{crit}$, the potential at the centre of the NW is ψ_0' given by Eqn. (5.30) and decreases with increasing D_{it}. In this regime, the NW is being depleted evenly throughout its entire radius. Finally, the built-in potential, defined as $V_{bi} = \psi_0 - \psi_s$, can also be plotted to showcase the much larger attainable V_{bi} for $a = 60$ nm (solid red line) than $a = 35$ nm (solid blue line) at high D_{it} due to the high ψ_0 maintained in the former. It can also be observed that in the fully depleted regime, ψ_0 decreases at the same rate as ψ_s, thus causing V_{bi} to remain constant with changing D_{it}

Consistent with this discussion is a plot of total surface charge and space charge as a function of D_{it} in Figure 5.2c. For the case of $a = 60$ nm, the depletion width continuously increases with increasing D_{it}, resulting in the rapid uncovering of positive space charge and an increase in the magnitude of both the surface charge (red solid line) and space charge (red dashed line). For the case of $a = 35$ nm, the same phenomenon of increasing surface charge (blue solid line) and space charge (blue

dashed line) occurs as D_{it} increases from 0 to D_{crit}. However, for $D_{it} > D_{crit}$, the depletion width has reached a maximum and the space charge density does not increase as drastically. Although the curves for $D_{it} > D_{crit}$ seem to remain constant, they are actually increasing in magnitude very slightly because the NW is still being depleted of majority free electrons as evidenced by the decrease in ψ_0 in Figure 5.2b. However, since the space charge density is explicitly written as $\rho = q(N_D - n)$, even large relative changes of the free electron carrier density, n, will not result in significant changes in ρ provided that $N_D >> n$ which is indeed the case in the SCR. However, these same large changes in n will still result in moderate changes in the position of the Fermi level.

Perhaps the best way to conceptualize Figure 5.2a-c is to examine the corresponding band diagrams of $a = 35$ nm NWs in Figure 5.2d. Figure 5.2d shows representative D_{it} values for the cases of $a > a_{crit}$ ($D_{it} < D_{crit}$), $a = a_{crit}$ ($D_{it} = D_{crit}$) and $a < a_{crit}$ ($D_{it} > D_{crit}$).

5.3.2 Model Output versus a

For completeness, Figure 5.3 shows key parameters plotted as a function of a for a typical $D_{it} = 10^{13}$ cm $^{-2}$ eV $^{-1}$. A large range of a values is used to showcase both fully and partially depleted regimes with large $a = 1$ μm representing the planar film case ($a >> w$).

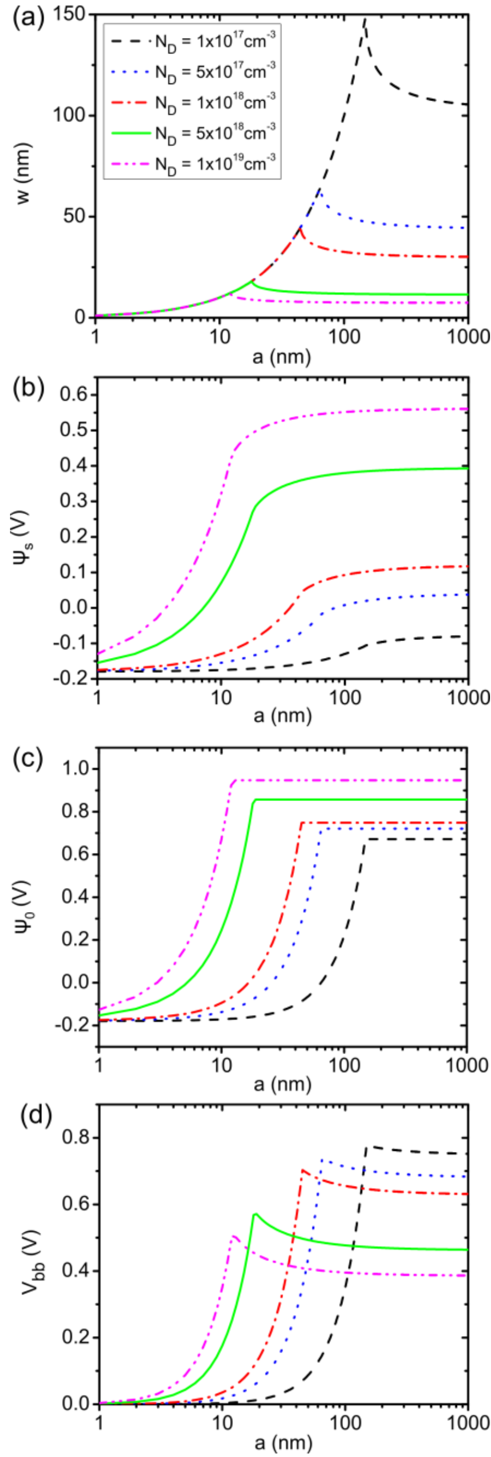

Figure 5.3: Model predictions of (a) w, (b) ψ_s, (c) ψ_0 and (d) V_{bb} versus a for different N_D curves. $D_{it} = 10^{13}$ cm $^{-2}$ eV^{-1} for all plots.

w is plotted as a function of a for various N_D values in Figure 5.3a. In the planar film case (near $a = 1\mu$m), the depletion width decreases with increasing doping density as is typical for Schottky barriers. The depletion width for each N_D increases steadily as a approaches a_{crit} and peaks at $a = a_{crit}$. This can be attributed to the surface area to volume ratio (*SAV*) being equal to $2/a$ and therefore, higher for small a. Physically, this increase in *SAV* with decreasing a decreases the number of bulk free electrons per surface state near the surface, thus locally decreasing the effective doping and causing w to increase in the partially depleted regime. It is clear that high doping densities are required to avoid full depletion of unpassivated nanowires with typical dimensions.

In the planar film case, ψ_s remains relatively constant as shown in Figure 5.3b. However, in the partially depleted regime just above $a = a_{crit}$, ψ_s begins to decrease with NW radius due to the increase in w from Figure 5.3a. Since Q_{it} is linearly dependent on ψ_s, this can be qualitatively explained by a decrease in surface charge density due to the decrease in the number of bulk free electrons per surface state mentioned above. In the fully depleted regime below $a = a_{crit}$, ψ_s decreases rapidly with NW radius. In the limit of small a, the Fermi level at the surface becomes pinned at the CNL and ψ_s approaches $-\Delta$.

Figure 5.3c shows ψ_0 as a function of a. As expected, ψ_0 increases with increasing N_D across all a. In the partially depleted regime of each curve, ψ_0 is a constant given by the solution to Eqn. (5.16). In the fully depleted regime for each curve, ψ_0 decreases with decreasing a as per Eqn. (5.30) and similar to ψ_s, the Fermi level at the centre of the NW also becomes pinned at the CNL and ψ_0 approaches $-\Delta$.

Figure 5.3d shows a plot of V_{bi}, the difference between Figure 5.3b and Figure 5.3c. This figure shows that the largest V_{bi} is attained when N_D is minimized. In the partially depleted regime above $a = a_{crit}$, the built-in potential increases to a maximum, $V_{bi,\max}$ at $a = a_{crit}$, due to the aforementioned ψ_s increase shown in Figure 5.3b. $V_{bi,\max}$ in NWs can increase by up to 34% from the planar film case of $V_{bi,\text{planar}} = V_{bi}(a = 1\,\mu\text{m})$, perhaps lending itself well to applications in NW photoconductor detectors utilizing high built-in potentials [16].

Figure 5.4 shows how n_{eff} and σ_{rel} vary as a function of a. In the partially depleted regime, Eqn. (5.35) can be simplified to $\sigma_{\text{rel}} = n_{\text{eff}} / N_D$ since $n_{\text{eff}} >> p_{\text{eff}}$. At $a = a_{crit}$, both n_{eff} and σ_{rel} can be reduced by up to 96% relative to the planar film case. To counteract this and preserve a high σ_{rel} of 0.5, a must be approximately double a_{crit}. In the fully depleted regime, n_{eff} and σ_{rel} are reduced drastically with decreasing a until some radius, a_0, is reached whereby $n_{\text{eff}} \approx n_i = 2.1\times10^6$ cm $^{-3}$, the intrinsic

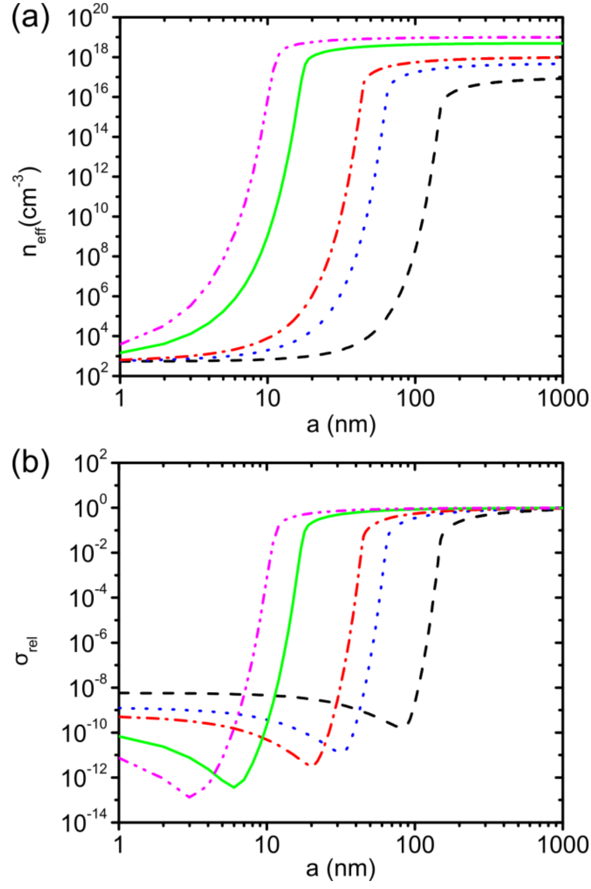

Figure 5.4: Model predictions of (a) n_{eff} and (b) σ_{rel} versus a for different N_D curves. $D_{it} = 10^{13}$ cm $^{-2}$ eV $^{-1}$ for all plots.

carrier concentration of GaAs [80]. At this radius, the Fermi level essentially lies at midgap throughout the NW, causing σ_{rel} to exhibit a minimum. As $a \to 0$ from a_0, n_{eff} continually reduces to a value less than n_i as consistent with the Fermi level lowering further and being pinned at the CNL throughout the NW. Therefore, as a is reduced from a_0 to 0, p_{eff} and correspondingly, σ_{rel} increase, thus causing inversion to occur.

This inversion with nanowire radius has been observed recently [89] and may prove useful for the development of NW MOSFETs.

5.3.3 Comparison with SRXPS measurements

To confirm the model to experiment, Si-doped p-type GaAs NWs ranging in radius from 75 nm to 105 nm were grown by MBE and characterized along their length by spatially resolved x-ray photoelectron spectroscopy (SRXPS). This was performed by Mattia Fanetti and others (collaborators from the Silvia Rubini group) at the Sincrotrone Trieste light facility. Due to the p-type doping, an analogous model was adapted for p-type NWs based on the band diagram shown in Figure 5.5a. SRXPS characterization enabled the determination of the binding energy of the trapped surface electrons, thus enabling the calculation of the Fermi level at the surface. As such, the surface Fermi level, found to be independent of axial position along the NWs, was determined for multiple wires, and plotted in Figure 5.5b. In this figure, NWs doped at a doping density of 4.6x10^{18} cm^{-3} (red points, samples REF1 and REF2) were found to have $q\psi_s \sim 0.5$ eV and NWs doped at 4.4x10^{17} cm^{-3} (orange points, sample REF3) were found to have $q\psi_s \sim 0.25$ eV. Doping density was determined by electrical measurements and used to model the depletion in the NW, yielding Figure 5.5c showing the potential at each end of the NW radius distribution (a=75nm and a=105nm) for $D_{it} = 1.5x10^{13}$ cm^{-2}eV^{-1}. This

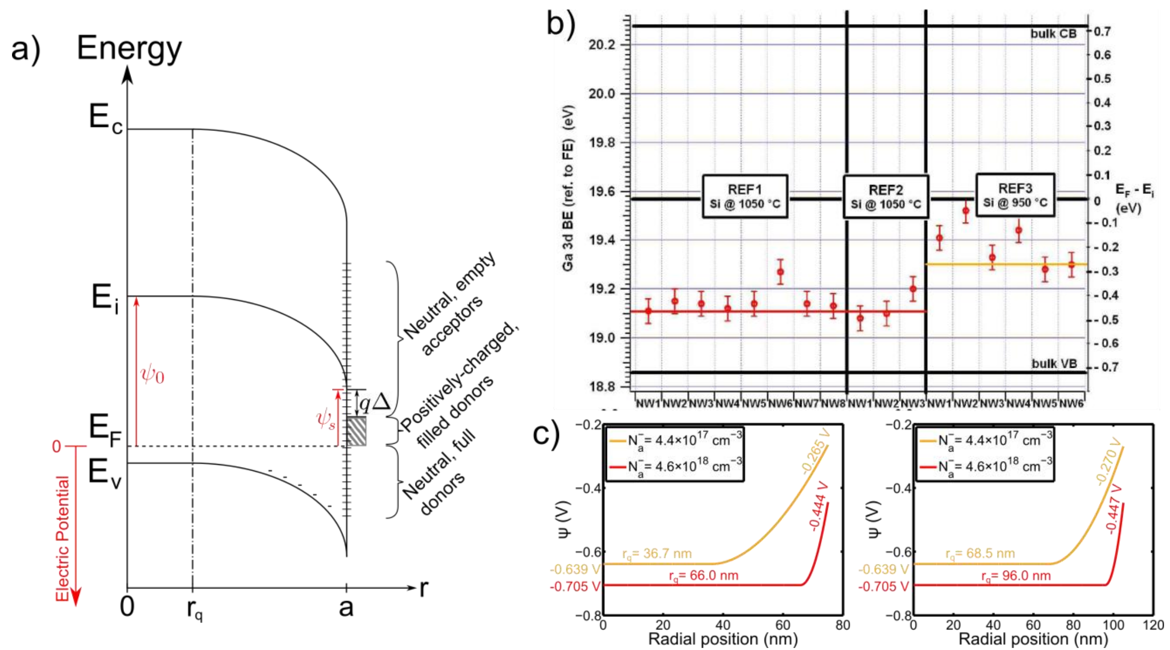

Figure 5.5: a) Band diagram showing surface depletion in a p-type NW. b) SRXPS for NWs p-doped at 4.6x10^{18} cm^{-3} (REF1 and REF2) and at 4.4x10^{17} cm^{-3} (REF3) along with the model generated fits represented by the solid red and orange lines. c) $\psi(r)$ for $D_{it} = 1.5x10^{13}$ cm^{-2}eV^{-1} for NWs ranging between a=75nm (left) and a=105nm (right). The red and orange fit lines from the model in (b) correspond to the colour-coded surface potentials in (c).

D_{it} value is consistent with previous reports on both GaAs NWs [90] and GaAs thin films which can have interface state densities ranging from 10^{12} cm^{-2}eV^{-1} to 10^{14} cm^{-2}eV^{-1} [91]. The surface potentials of approximately 0.27V and 0.45V for REF1,2 and REF3, respectively, from Figure 5.5c fit very well to measured surface Fermi levels shown in Figure 5.5b, thus confirming the validity of the model.

5.4 Conclusion

In conclusion, a comprehensive analytical model was established to give a complete description of surface depletion in NWs in relationship to D_{it}, a and N_D. For completeness, this model gives distinct solutions to the cases of full and partial NW depletion, while specifying the CNL level and using an analytical expression for the Fermi-Dirac integral.

From the model, key parameters were plotted as a function of both D_{it} and a, showing interesting features in both the fully and partially depleted regimes. Once in the fully depleted regime, the NW depletes evenly throughout the NW with increasing D_{it}, causing the Fermi level to drop below the planar value for ψ_0. In the partially depleted regime, due to increasing *SAV* of NWs as $a \to a_{crit}$, w was found to increase by more than 41% compared to a planar film for a typical $D_{it} = 10^{13}$ cm^{-2}eV^{-1}. This increase in w causes a drastic reduction in ψ_s, while ψ_0 remains a constant, causing V_{bb} to increase by up to 34% from planar film values. This increase could prove useful in NW photoconductor detectors.

Furthermore, NW conductivity was examined. When $a = a_{crit}$, the NW conductivity was reduced by up to 96% relative to bulk, highlighting the severity of NW surface depletion and the need for surface passivation. In order to preserve a high σ_{rel} of 0.5, a must be approximately $2a_{crit}$. At some radius a_0 (where $0 < a_0 < a_{crit}$), the

Fermi level lies near midgap, causing conductivity to become a minimum. Below a_0, inversion occurs and conductivity increases. Inversion in thin NWs may be utilized in the operation of NW MOSFETS.

Finally, the model was compared to SRXPS results and gave excellent fits to experimentally determined surface Fermi levels. This confirmed the validity of the depletion model.

6 AlInP Surface Passivation of GaAs Nanowires

6.1 Introduction

Surface effects such as surface depletion and recombination have been shown to be one of the dominant factors which limit current III-V NW solar cell devices [31] as discussed previously in Chapter 1.3. While this can be addressed by merely increasing the radii of NWs, this option would result in the loss of some of the most promising NW properties such as the ability for NW growth on lattice-mismatched substrates and the potential for quantum confinement. This stresses the need for surface passivation to be implemented into III-V NW devices.

While successful surface passivation of Si NWs has been reported frequently [92], surface passivation of GaAs NWs is less common. Chemical surface passivation of GaAs NWs using $(NH_4)_2S$ has demonstrated an order of magnitude decrease in surface state density [93] and was subsequently implemented into a GaAs NW ensemble solar cell to improve the relative conversion efficiency by 19% [84]. Unfortunately, this type of sulfur passivation layer is unstable in oxygen, thus casting doubt on its long-term viability.

Surface passivation of GaAs NWs using various III-V materials have also been explored. By growing InGaP shells radially onto GaAs cores, photoluminescence (PL)

intensity was found to increase by three orders of magnitude [85]. Perhaps the most common III-V passivation material to date has been AlGaAs with a GaAs capping layer. AlGaAs passivation of GaAs NW sidewalls has shown a 20x improvement in PL intensity [86], an order of magnitude decrease in surface recombination velocity using time-resolved photoluminescence (TRPL) [87], and an 82% decrease in surface state density using time-resolved terahertz spectroscopy [58].

In this chapter, GaAs NW surfaces were passivated with a lattice-matched AlInP shell. Due to its wide bandgap and low refractive index, AlInP lends itself well to optoelectronic applications and is already currently used as a window layer in solar cells [94] and a cladding layer in lasers and LEDs [95]. The performance of AlInP as a passivation layer was assessed in this work by fabricating ensemble NW devices and comparing the current-voltage (I-V) characteristics between AlInP-passivated GaAs NW devices and unpassivated GaAs NW reference devices. TRPL measurements were also conducted to compare carrier lifetimes between passivated and unpassivated GaAs NWs. This chapter was largely taken from work published in the Nanotech 2013 conference proceedings [37] and in Semiconductor Science and Technology [38]. With the exception of a sulfur passivated GaAs NW ensemble solar cell [84], all aforementioned reports have been based on optical characterization of single NWs to confirm passivation. As such, this was one of the first reports of surface passivation demonstrated by electrical characterization of a NW ensemble device with a III-V passivating shell.

6.2 Experimental Details

The radial GaAs-AlInP heterostructure NWs were grown by the Au-assisted vapor-liquid-solid (VLS) mechanism using a gas source molecular beam epitaxy (MBE) system. In preparation for growth, an n-type GaAs (111)B substrate with a silicon doping density of (1-5)$\times 10^{18}$ cm^{-3} was pre-cleaned by a 20 min UV ozone, followed by a 30s buffered HF bath and finally a 10 min rinse in deionized (DI) water. The substrate was then transferred into an electron-beam evaporation system where 1 nm of Au was deposited onto the substrate to serve as the seed particle for VLS growth. Finally, the substrate was placed in the MBE system where it underwent several degassing and plasma cleaning steps (described elsewhere [96]) in preparation for NW growth. The NWs were then grown, starting with the n-type GaAs core. The GaAs core was grown at a high growth temperature of 600°C for 30 min with a V/III flux ratio of 2.3 and a two-dimensional equivalent growth rate of 0.5 μm/hr. The GaAs core segment was also doped with Te to achieve a nominal doping density of 1×10^{18} cm^{-3} as calibrated by previous thin film growths. Finally, the undoped, nominally lattice-matched $Al_{0.52}In_{0.48}P$ shell was grown at a lower temperature of 500°C and a higher V/III flux ratio of 3.5 to promote shell growth, while keeping the growth rate and duration the same as that of the core. An unpassivated reference sample was also grown using the same conditions but without the AlInP shell growth.

A JEOL JSM-7000F scanning electron microscope (SEM) was used to characterize the as-grown NW ensemble, while a JEOL 2010F high resolution transmission electron microscope (TEM) was used to characterize individual NWs removed from the substrate by sonication.

After characterization by electron microscopy, an ensemble NW resistor device was fabricated using a series of processing steps outlined schematically in Figure 6.1a-d. First, a 3:1 volume mixture of Cyclotene 3022-35 to T1100 thinner was spin-coated onto the passivated and unpassivated NW ensemble samples to act as a planarizing material to achieve the structure shown schematically in Figure 6.1a. Cyclotene was selected due to its high thermal stability, low porosity, low surface roughness and high electrical resistivity as reported in Chapter 3. Next, the Cyclotene layer was back-etched to a height of $\sim 1\ \mu$m by reactive ion etching (RIE) in a 1:1 mixture (by flow rate) of O_2 and CF_4 as shown schematically in Figure 6.1b. Thereafter, the samples were sonicated in DI water for 60 minutes using a Branson 1510 ultrasonic cleaner. This was used as a novel method to remove the tops of the NWs that were exposed above the polymer film. This method also removed the AlInP segment covering the top of the NWs to expose the GaAs core for electrical contacting and achieve complete planarization of the NW array as shown schematically in Figure 6.1c. Finally, an array of 0.5 mm^2 top contact pads composed of 50 nm Ni, 100 nm Ge and 650 nm Au, and a bottom substrate contact composed of 25 nm Ni, 50 nm Ge and 120 nm Au were deposited by electron beam evaporation (as shown schematically in Figure 6.1d) followed by subsequent annealing

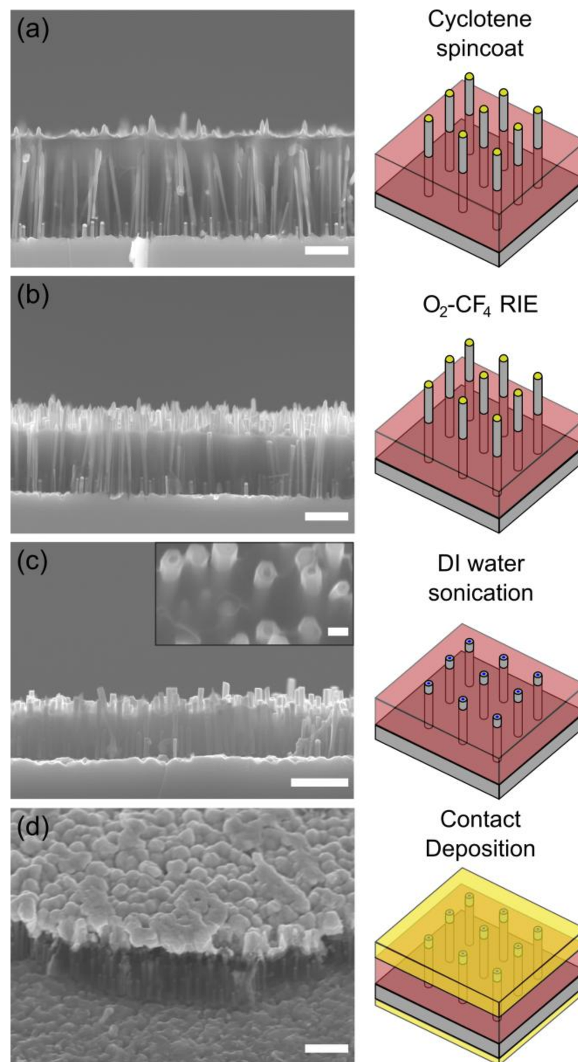

Figure 6.1: Tilted and side-view SEM images and schematics of the NW ensemble (a) after spin-coating with the Cyclotene mixture (1 µm scale bar), (b) after reactive ion etching (1 µm scale bar), (c) after DI water sonication (1 µm scale bar, Inset: 100 nm scale bar) and (d) after contact deposition and annealing (1 µm scale bar).

at 400°C in N_2 for 30s to alloy the contacts to the GaAs. The details of these processing steps are reported thoroughly in previous chapters.

Upon completion of device fabrication, I-V characteristics of the passivated and unpassivated samples were measured across the length of NWs (between top and

bottom contacts, as shown schematically in Figure 6.3a using a two-point probe system with a Keithley 2400 sourcemeter. In this work, positive bias corresponds to the situation whereby the top of the NWs are held at a potential, +V, while the bottom of the substrate is tied to ground. Capacitance-voltage (C-V) characteristics were also measured between top and bottom contacts on unpassivated NW devices using a Hewlett Packard HP4192A analyzer with 0.01 V modulation voltage at 1 kHz. The sample was connected to the instrument by means of the HP 16047 C Test Fixture. Dynamic secondary ion mass spectrometry (SIMS) was performed on the unpassivated NW sample to ascertain the doping density in the NWs. The details of this SIMS analysis have been discussed in Chapter 4.

Finally, PL and TRPL were used to confirm surface passivation. The experimental details of this optical characterization can be found in Chapter 2.

6.3 Results

SEM characterization of as-grown NWs in Figure 6.2a showed a dense array of vertical NWs with heights varying between 1 µm and 2.5 µm and a NW density of approximately 2×10^{9} cm^{-2}. The radius of unpassivated NWs varied from 10-36 nm, while that of the passivated NWs varied from 15-80 nm due to the additional thickness of the AlInP shell. High angle annular dark field (HAADF) TEM imaging of sonicated NWs in Figure 6.2b showed a "spear" morphology near the NW top. The contrast stripes

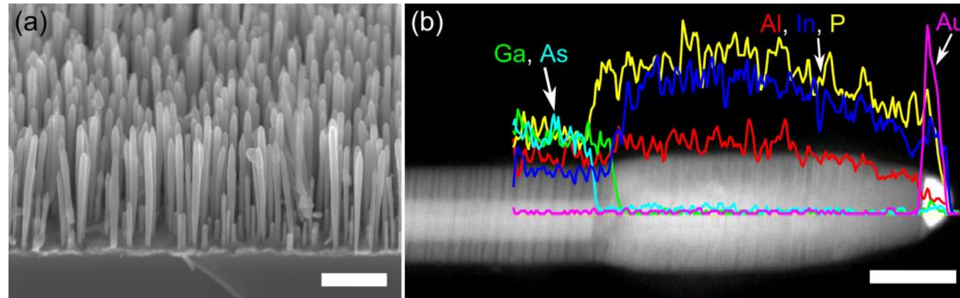

Figure 6.2: (a) 45o tilted SEM image of the as-grown NW ensemble (1 µm scale bar). (b) HAADF image of an individual NW. Superimposed EDX linescans indicate the presence of Ga (green) and As (cyan) in the core; Al (red), In (blue) and P (yellow) in the shell and top axial segment; and the Au (purple) seed particle at the top of the NW. The scale bar is 50 nm.

across the NW diameter are stacking faults, commonly observed in NWs and reported previously [97,98]. The energy dispersive x-ray spectroscopy (EDX) linescan showed that the NW top underneath the Au particle (the "spear head") is composed only of AlInP, while the NW base contains both the GaAs core and the AlInP shell. The detection of Al, In and P in the base region of the nanowire in the EDX linescan come from the shell in front of and behind the GaAs core. By examining the Z-contrast in HAADF imaging, it is clear that the NW is composed of a GaAs core denoted by the bright high-Z contrast, and a surrounding AlInP shell denoted by the dark low-Z contrast. The $Al_x In_{1-x} P$ shells were found by EDX to have an average composition of x=0.52 with a standard deviation of 0.03, confirming a lattice-match to the GaAs core. The HAADF imaging indicated a typical AlInP shell thickness of 5 nm near the base of the NWs to 45 nm near the top of the NWs, thus giving reason for the reverse tapering observed in Figure 6.2a. HAADF

imaging of NW cross sections prepared by ultramicrotome (not shown) confirmed that the GaAs core was encapsulated by AlInP throughout its entire length.

A comparison of the respective SEM images and schematics in Figure 6.1 show that the desired structures were achieved at each processing step. I-V measurements described below indicated that the AlInP shells conducted negligible current. Hence, removal of the axial, "spear head" section of AlInP (shown in Figure 6.2b) was imperative to successfully contact the conductive GaAs cores instead of the insulating AlInP. This was accomplished by the sonication procedure. In Chapter 3, sonication was proven useful only in achieving planarization and removing the Au catalysts at the top of the NWs. While that is certainly achieved here as shown by the planar NW ensemble in Figure 6.1c, sonication has also proven to be useful in removing the AlInP "spear head" as shown clearly by the exposed GaAs cores in the inset of Figure 6.1c. Due to its mechanical nature, this technique can be broadly applied to all NW heterostructures composed of other materials. From Figure 6.1c, the length of the NWs in the device were found to equal 900 nm as tabulated in Table 6.1.

Figure 6.3b shows I-V curves of both passivated and unpassivated NWs using the corresponding color-coded two-point probe configurations found in Figure 6.3a. Firstly, it must be noted that a parasitic series resistance of 3Ω exists within the measurement apparatus, which was added to the subsequent model as a series resistance, R_s. I-V characteristics measured laterally across Contact A (green triangles) and vertically across the GaAs substrate and film alone (without NWs) at Contact C (blue triangles) showed

Table 6.1: Parameter values used in model

Variable	Description	Value	Reference/Source
a	NW radius	Figure 6.5b	SEM
N_D^+	Donor concentration in NW	9.8×10^{17} cm $^{-3}$	SIMS
D_{it}	Density of interface states along GaAs NW surface	Figure 6.4	C-V
L	Length of NWs	900 nm	SEM
A_{NWs}	Area of the tops of the NWs under a contact pad	1.05×10^{-4} cm ^{2}	SEM
A_{pad}	Area of a contact pad	5.03×10^{-3} cm ^{2}	SEM
$N_{D,sub}$	Donor concentration in the substrate	2.5×10^{18} cm $^{-3}$	known
$\varepsilon_c / \varepsilon_0$	Cyclotene relative permittivity	2.65	known
$\varepsilon / \varepsilon_0$	GaAs relative permittivity	12.9	[80]
N_C	Effective density of states in conduction band	4.7×10^{17} cm $^{-3}$	[80]
μ_n	Electron mobility	3000 cm ^{2} V $^{-1}$ s $^{-1}$	[80]
μ_p	Hole mobility	150 cm ^{2} V $^{-1}$ s $^{-1}$	[80]
τ_p	Excess hole carrier lifetime in the substrate	1 ns	[99]
τ_n	Excess electron carrier lifetime in the NWs	1 μ s	[99]
ψ_{CNL}	Charge neutrality level	0.53 eV	[80]
R_s	Parasitic series resistance in the measurement apparatus	3 Ω	I-V
r_c	Specific contact resistivity	10^{-6} Ω cm ^{2}	[100]
R_{lk}	NW Leakage Resistance	1.2 GΩ	[101]
n	Ideality factor	3	[102]

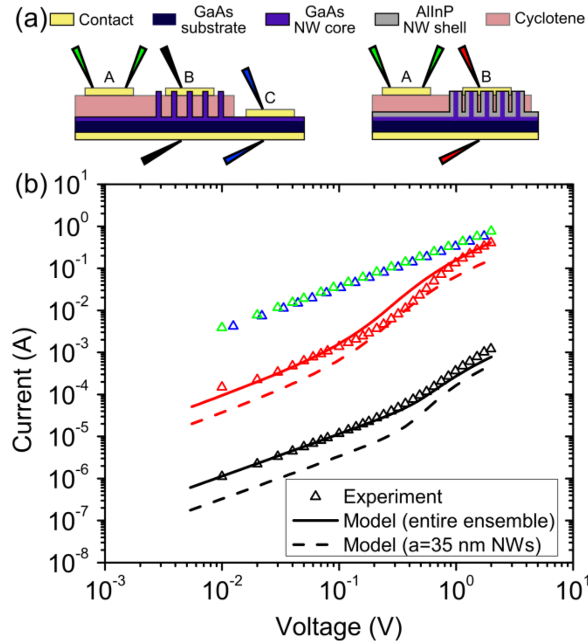

Figure 6.3: (a) Schematic of the three different top contacts deposited on unpassivated (left) and passivated (right) NW devices with varying two-point probe configurations. (b) Current-voltage measurements across a single contact pad (green), the substrate alone (blue), passivated NWs (red) and unpassivated NWs (black). Model-generated I-V curves (solid lines) of the entire ensemble and that from the upper 1% of NW diameters (dashed lines). The colours of the curves correspond with the probe colours in (a).

linear behaviour with a resistance equal to the parasitic series resistance. This indicated a relatively small contribution of the film, substrate and top contact to the overall series resistance. Secondly, the I-V curve was found to be non-linear, yet weakly rectifying due to factors discussed in the Model section. Due to the weak rectification and the treatment of the reverse bias behaviour in previous reports [88], this report was solely focused on the forward bias characteristics displayed in Figure 6.3b. Thirdly, a comparison of the I-V characteristics measured across passivated NWs (red triangles) showed a two order of magnitude increase in current and four order of magnitude

decrease in high-bias resistance compared to unpassivated NWs (black triangles). The passivated NWs showed a current limited by R_s at high bias. Additionally, further I-V measurements of passivated NWs (not shown) with the axial AlInP sections left intact were found to draw two orders of magnitude less current than the unpassivated NWs, thus confirming that conduction occurred almost exclusively within the GaAs cores. As such, the increase in current flow upon the addition of the AlInP shell signifies successful passivation. Results of the characterization using C-V and TRPL are deferred to discussions below.

6.4 Model

To fully examine the extent of surface passivation, the I-V characteristics were fit using a combination of two models: a surface depletion model and a transport model. The surface depletion model was taken mostly from Chapter 5, but does not assume complete ionization of donor impurities and contains modifications to include a density of surface states which is nonuniform across the bandgap. This surface depletion model determined the variation in electric potential as a function of radius in the NW and the resultant effective carrier concentrations needed for the subsequent transport model. The transport model enabled the NW ensemble to be modeled using an equivalent circuit from which the I-V fits were generated. A capacitance model was also used to determine the interface state density energy distribution.

6.4.1 Modified Surface Depletion Model

While a thorough derivation of the surface depletion model is already given in Chapter 5, a summary of key equations and a derivation of the modifications will be discussed for convenience. For a cylindrical NW, Poisson's equation can be reduced to an ordinary differential equation in r, the radial distance:

$$\frac{\partial^2\psi}{\partial r^2}+\frac{1}{r}\frac{\partial\psi}{\partial r}=-\frac{\rho}{\varepsilon} \tag{6.1}$$

where ρ is the net bulk charge density, ψ is the electric potential and ⍰ is the permittivity of GaAs.

6.4.1.1 Partially Depleted Regime

As per Chapter 5, the potential in the NW is given by:

$$\psi(r) = \begin{cases} \psi_0 & \text{for } 0<r<r_q \\ \psi_0+\frac{qN_D^+r_q^2}{2\varepsilon}[-\frac{r^2}{2r_q^2}+\ln(\frac{r}{r_q})+\frac{1}{2}] & \text{for } r_q<r<a \end{cases} \tag{6.2}$$

where q is the elementary charge, N_D^+ is the ionized donor doping density, r_q is the radius of the quasi-neutral core region of the NW, ψ_0 is the potential along the centre axis of the NW and a is the radius of the GaAs core. To fully express $\psi(r)$, ψ_0 and r_q must be determined.

ψ_0 can be determined using Fermi-Dirac statistics which states that $n=N_D^+$ at the NW centre:

$$\frac{2}{\sqrt{\pi}} N_c F_{1/2}(\eta_{F0}) = N_D^+ \quad \text{where} \quad \eta_{F0} = \frac{q\psi_0 - E_g/2}{kT} \tag{6.3}$$

where $F_{1/2}(\eta)$ is the Fermi-Dirac integral, N_c is the effective density of states in the conduction band, E_g is the bandgap energy, k is the Boltzmann constant, and *T* is the temperature.

r_q can be determined by invoking charge neutrality which states:

$$\pi(a^2 - r_q^2)qN_D^+ + 2\pi a Q_{it} = 0 \tag{6.4}$$

where Q_{it} is the surface charge density. This states that r_q is uniquely expressed in terms of Q_{it} for a NW of known a and N_D^+.

Along the NW sidewalls [36]:

$$Q_{it} = -q^2 \int_0^{(\psi_s+\Delta)} D_{it}(V)dV \tag{6.5}$$

where D_{it} is the density of interface states at the GaAs nanowire surface, $\psi_s \equiv \psi(r=a)$ is the surface potential, and $\Delta \equiv \frac{E_g}{2q} - \psi_{\text{CNL}}$ where ψ_{CNL} is the charge neutrality level (CNL). For GaAs, $\psi_{\text{CNL}} = 0.53\text{V}$ [80] and thus, $\Delta = 0.18\text{V}$. It is clear that Q_{it} is uniquely determined by ψ_s for a NW of known $D_{it}(V)$. In turn, ψ_s at the surface of the NW (r=a) is given by Eqn. (6.2) to yield:

$$\psi_s = \frac{qN_D^+ r_q^2}{2\varepsilon}\left[-\frac{a^2}{2r_q^2} + \ln\left(\frac{a}{r_q}\right) + \frac{1}{2}\right] + \psi_0 \tag{6.6}$$

In summary, given a NW with known N_D^+, a and $D_{it}(V)$, ψ(r) can be determined transcendentally from Eqn. (6.2) to (6.6).

6.4.1.2 *Fully Depleted Regime*

In the previous analysis, r_q cannot be solved for all a values. For a specific set of N_D^+ and $D_{it}(V)$ values, there exists a critical radius, a_{crit}, below which the entire NW is depleted. To find a_{crit}, Eqn. (6.4) must be solved for a in the limit as r_q approaches zero. For $a > a_{crit}$, the NW is in the partially depleted regime, allowing application of the previous analysis. However, for $a < a_{crit}$, the NW is in the fully depleted regime ($r_q = 0$) and is treated as follows.

As per Chapter 5, the potential in a fully depleted NW is given by:

$$\psi(r) = \psi_0 - \frac{qN_D^+}{4\varepsilon} r^2 \quad \text{for} \quad 0 < r < a \tag{6.7}$$

ψ_0 can be found by invoking charge neutrality, examining the surface charge. This yields Eqn. (6.4) and (6.5) again, but with $r_q = 0$. These equations can be combined to give an expression for Q_{it} which is a transcendental equation in ψ_s given a NW with known N_D^+, a and $D_{it}(V)$:

$$-\frac{aqN_D^+}{2} = -q^2 \int_0^{(\psi_s + \Delta)} D_{it}(V) dV \tag{6.8}$$

ψ_0 can subsequently be determined easily from Eqn. (6.7):

$$\psi_0 = \psi_s + \frac{qN_D^+}{4\varepsilon}a^2 \quad (6.9)$$

With ψ_0 determined, a complete expression for $\psi(r)$ can be given as per Eqn. (6.7).

6.4.2 Capacitance Model

In the previous analysis, it remains to determine $D_{it}(V)$. $D_{it}(V)$ for the unpassivated NWs was estimated from measured C-V characteristics. The differential form of the surface charge density can be stated as:

$$dQ_{it} = -q^2 D_{it}(V)dV \quad (6.10)$$

where V is an applied bias and D_{it} is the density of states at the GaAs surface. This equation qualitatively states that at some applied bias, V, an infinitesimal change in the surface charge density, dQ_{it}, is equal to $D_{it}(V)$ multiplied by the infinitesimal change in energy range (of filled surface states), qdV, multiplied by the elementary charge, q. From Eqn. (6.5), $D_{it}(V)$ is related to the capacitance across the NWs, C_{NWs}, according to [80]:

$$C_{NWs}(V) = \frac{dQ}{dV} = A_{NWs}q^2 D_{it}(V) \quad (6.11)$$

where A_{NWs} is the area of the tops of the NWs under a contact pad. The total capacitance between top and bottom contacts is estimated as:

$$C_{tot}(V) = C_{NWs}(V) + C_c = C_{NWs} + \frac{\varepsilon_c(A_{pad} - A_{NWs})}{L} \quad (6.12)$$

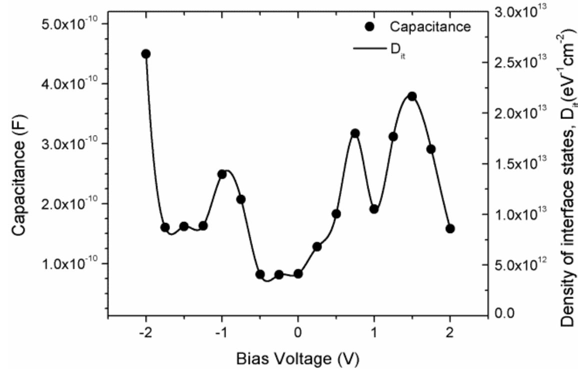

Figure 6.4: 1kHz-modulated C-V data (black circles, left axis) and interpolated $D_{it}(V)$ (solid line, right axis) for unpassivated NWs.

where C_c is the capacitance across the cyclotene, ε is the permittivity of the cyclotene and A_{pad} is the area of the contact pad. C_c was found to be 12.8 pF. Combining Eqn. (6.12) with Eqn. (6.11) allows $D_{it}(V)$ to be calculated. In this analysis, we assume that the C-V characteristic is dominated by surface (interface) states at the NW-contact interface, and that this surface state density is similar to that on the NW sidewalls.

Using this analysis, the measured C-V data in Figure 6.4 (left axis) was interpolated to yield $D_{it}(V)$, which is plotted in Figure 6.4 as the black solid line. For the passivated sample, we assumed that the surface passivation reduced $D_{it}(V)$ by a constant factor across the bias range (i.e., for all V). This is consistent with previous reports which assume a uniform surface state distribution density that is reduced by a constant 82% across the distribution [58].

6.4.3 Transport Model

To relate model generated $\psi(r)$ functions to carrier transport, one must first use the Fermi-Dirac integral to determine the free electron and hole densities, $n(r)$ and $p(r)$, respectively [36]. The effective free carrier densities in a particular nanowire NW_i can then be found by integrating and subsequently averaging $n(r)$ and $p(r)$ across the radius a_i of NW_i:

$$n_{\mathrm{eff,i}} = \frac{1}{\pi a_i^2} \int_0^{a_i} n(r) 2\pi r dr \tag{6.13}$$

$$p_{\mathrm{eff,i}} = \frac{1}{\pi a_i^2} \int_0^{a_i} p(r) 2\pi r dr \tag{6.14}$$

With these effective carrier densities calculated numerically, all necessary carrier transport equations can be solved. The NW ensemble device was modeled with an equivalent circuit shown in Figure 6.5a. Each parallel branch in Figure 6.5a represents a single NW and is composed of a diode D_i, series resistor R_i and identical leakage resistor R_{lk}.

The diode, D_i, arises due to the surface depletion of each NW_i. As will be shown in the subsequent discussion, surface depletion of the NWs results in effective electron concentrations of approximately 10^{13} cm^{-3} and 10^{17} cm^{-3} for even the thickest unpassivated and passivated NWs respectively. For the thinner NWs that comprise the majority of the ensemble, the effective electron concentration is even lower, even reaching intrinsic levels at some radii. This makes the NWs resemble a lightly doped or

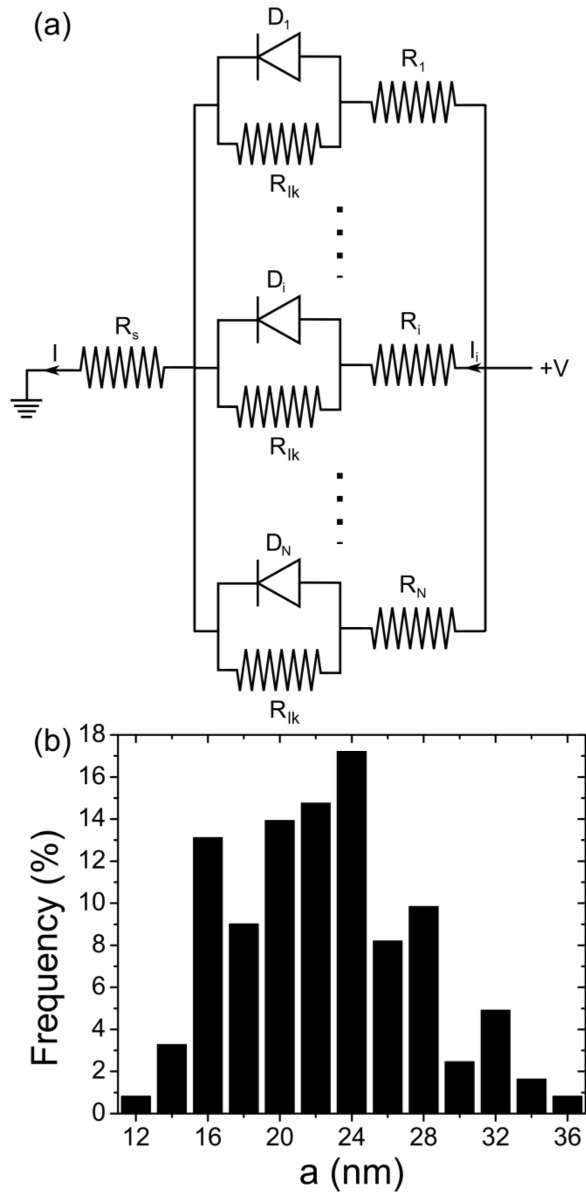

Figure 6.5: (a) Equivalent circuit diagram of the ensemble device. The left side represents the bottom contact, while the right side represents the top contact. (b) Radius distribution of all contacted GaAs cores.

even intrinsic GaAs film. Since the NWs are in contact with a highly doped substrate with a carrier concentration of (1-5)$\times 10^{18}$ cm^{-3}, electrons will diffuse from the substrate into the NWs, thus establishing a potential barrier. In effect, this creates an p-i-n junction minus the p-type section at the NW-substrate interface of NW$_i$ which can be modeled by diode, D_i. As confirmed experimentally, D_i is expected to give weak rectification relative to a pn junction. Assuming low injection, it can be easily shown that the reverse saturation current for D$_i$ is given in general by [80]:

$$I_{0,i} = \pi a_i^2 q \left(\frac{D_p p_{sub}}{L_p} + \frac{D_n n_{\text{eff},i}}{L_n} \right) \tag{6.15}$$

where D_p, L_p and p_{sub} are the diffusion coefficient, diffusion length and carrier concentration for holes in the n-doped substrate while D_n, L_n and $n_{eff,i}$ are the diffusion coefficient, diffusion length and effective carrier concentration for electrons in NW$_i$.

The series resistance, R_i, represents the resistance of NW$_i$ as determined by the surface depletion model. Under low injection, the conductance of a shell of radius r and infinitesimal thickness *dr* is given by $dG_i = q\left[\mu_e n(r) + \mu_p p(r)\right] 2\pi r dr / L$ where μ_e is the electron mobility, μ_p is the hole mobility and L is the length of the NW. Thus, the conductance of NW$_i$ can be found by integrating with respect to radius to yield a NW resistance of:

$$R_i = (G_i)^{-1} = \left(\frac{\sigma_{\mathrm{eff},i} \pi a_i^2}{L} \right)^{-1} \tag{6.16}$$

where $\sigma_{\mathrm{eff},i} = q(\mu_e n_{\mathrm{eff},i} + \mu_p p_{\mathrm{eff},i})$. Taking into consideration the specific contact resistance, r_c, finally yields:

$$R_i = \left(\frac{\sigma_{\mathrm{eff},i} \pi a_i^2}{L} \right)^{-1} + \frac{r_c}{\pi a_i^2} \tag{6.17}$$

Finally, R_{lk} in Figure 6.5a represents a possible leakage path for current to bypass the NWs. Current leakage has been previously observed in single NW I-V measurements [103] with a possible source being surface charge hopping [104].

Standard circuit analysis of Figure 6.5a shows that the current flowing through a single NW, I_i, and the voltage drop across the parallel branches, V', can be related by the transcendental equation:

$$I_i(V') = I_{0,i} \left[\exp\left(\frac{V' - I_i R_i}{nV_t} \right) - 1 \right] + \frac{V' - I_i R_i}{R_{lk}} \tag{6.18}$$

where n is the ideality factor, $V_t = kT/q$ is the thermal voltage and $V = V' + IR_s$ is the applied bias. To fit the experimental I-V data, I_i is summed over the entire NW radius distribution under the contact pad ($I = \sum_{i=1}^{N} I_i$), thus yielding the total current measured from a contact pad. The NW radius distribution in Figure 6.5b was determined from SEM measurements.

6.5 Analysis and Discussion

Table 6.1 summarizes the model parameters. As described earlier, SEM characterization was used to measure the distribution in NW radius. SIMS was used to measure the dopant concentration from which the ionized dopant concentration was determined as $N_D^+ = (9.1 \pm 0.7) \times 10^{17}$ cm^{-3}. $N_D^+ = 9.8 \times 10^{17}$ cm^{-3} was found to provide the best fit to the data and falls within the measurement uncertainty. The value of r_c was taken for GaAs contacted with Ni-Ge-Au [100] and was found to have a negligible contribution compared to the parasitic series resistance. The ideality factor, n, in Eqn. (6.18) was found to have a value of 3, consistent with the large ideality factors as high as 4.52 previously observed in pn junction NWs [102]. To fit the unpassivated data at low bias, R_{lk} was set to 1.2 GΩ. With these and the remaining parameters [80,99] in Table 1, a good fit to the I-V measurements was obtained as shown in Figure 6.3b. Most importantly, the passivated NW I-V data were fit with a reduction in D_{it} of 55%. At zero bias, this represents a reduction from $D_{it} = 4.2 \times 10^{12}$ cm^{-2} eV^{-1} for unpassivated NWs to $D_{it} = 1.9 \times 10^{12}$ cm^{-2} eV^{-1} in passivated NWs, which rivals the performance of previous AlGaAs and $(NH_4)_2S$ passivation results [58,93].

Figure 6.3b also shows the model I-V curve for passivated NWs (red dashed line) and unpassivated NWs (black dashed line) using only the GaAs NWs with radii varying between $a = 34$ nm and $a = 35$ nm. This range represents the top 1% of the NW

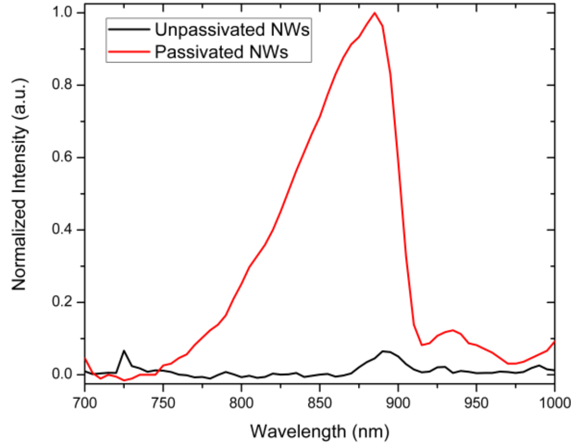

Figure 6.6: PL spectra from passivated (red) and unpassivated (black) NWs

ensemble radius distribution. The similarity in magnitude between the current drawn by the entire ensemble and the current drawn by the thickest 1% of the NW ensemble shows that the current is dominated by the $a \sim 35$ nm NWs due to their low resistance relative to smaller radius NWs. Upon examination of $\psi(r)$ for both unpassivated and passivated NWs, it was found that the unpassivated $a = 35$ nm NWs were fully depleted with the Fermi-level pinned a mere 0.12 eV above the midgap ($\psi_s = 0.12$ V), while the passivated $a = 35$ nm NWs were only partially depleted ($r_q \sim 4$ nm) with the Fermi-level 0.36 eV above midgap ($\psi_s = 0.36$ V). Using Eqn. (6.13), this corresponds to an effective free electron carrier concentration of $n_{\mathrm{eff}} = 4.4 \times 10^{13}$ cm $^{-3}$ for unpassivated NWs and $n_{\mathrm{eff}} = 1.2 \times 10^{17}$ cm $^{-3}$ for passivated NWs, representing a four order of magnitude improvement, thus showing the effectiveness of passivation. In order to further confirm effective passivation using AlInP shells, both PL and TRPL were performed on both passivated and unpassivated samples. PL spectra shown in Figure 6.6

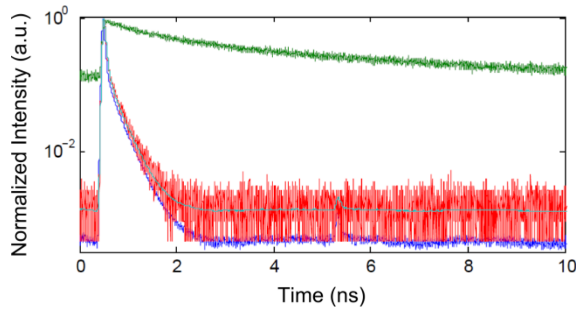

Figure 6.7: TRPL decay curves comparing passivated NWs (green) with unpassivated NWs (red). The blue curve shows the system response, while the cyan curve is a fit to the unpassivated NW PL spectrum.

shows a 20x increase in PL intensity upon passivation. As shown in the TRPL decay curves of Figure 6.7, the PL decay from unpassivated NWs is very short, with an approximate lifetime of 20 ps. The decay from core-shell NWs is non-exponential, with an effective lifetime of ~ 500 ps, marking a 25x improvement.

6.6 Conclusion

In conclusion, the fabrication and passivation of an ensemble NW device has been successfully demonstrated. During fabrication, sonication was used as a novel method to successfully remove axial AlInP sections, allowing the GaAs NW core to be contacted for I-V characterization. Model parameters included the NW radius distribution obtained from SEM, doping density obtained from SIMS, and energy distribution of surface state density estimated from C-V measurements. Using reasonable fitting parameters, the NWs were shown to exhibit a 55% decrease in

surface state density upon passivation and an impressive four order of magnitude increase in the effective carrier concentration of the characteristic a=35 nm NWs. The thickest 1% of NWs in the ensemble dominated the I-V characteristics, which is a behavior that should be common to all ensemble NW devices with a distribution in radius. Finally, passivation was further confirmed PL measurements showing a 20x improvement in PL intensity and by TRPL measurements showing a 25x improvement of carrier lifetime upon passivation.

7 Electrostatic Model of Radial PN Junction Nanowires

7.1 Introduction

In the effort to realize the untapped potential of radial pn junction NWs, many empirical attempts have been made to optimize the efficiency of devices. However, little work has been done to establish fundamental models of underlying electrostatics of NWs. Earlier reports focused on modelling carrier transport in thicker NWs, thus allowing full depletion of the shell or core to be ignored [105]. Later reports have examined thin NWs, but have used numerical models, thus limiting the extraction of qualitative physical behavior for a wide variety of NW parameters [31]. There is therefore a need for a radial pn junction NW model that is applicable to a wide variety of core and shell doping densities, dimensions and surface state densities. In this contribution, Poisson's equation is solved for a p-core/n-shell structure to give radial energy band profiles and electric fields for a NW of arbitrary doping, radius and surface state density. The model is used to generate results for a wide range of parameters to examine the underlying physics and optimize the built-in potential of the pn junction. This work has been published in the Journal of Applied Physics [39].

7.2 Theory

Invoking the symmetry of a long cylindrical NW, Poisson's equation can be reduced to an ordinary differential equation in *r*, the radial distance:

$$\frac{d^2\psi}{dr^2}+\frac{1}{r}\frac{d\psi}{dr}=-\frac{\rho}{\varepsilon}=-\frac{dE}{dr}-\frac{E}{r} \tag{7.1}$$

where ρ is the net bulk charge density, ψ is the electric potential, ε is the permittivity of the NW material and E is the electric field. As in Chapter 5, the $\psi(r)$ is defined to be the potential difference between the radially changing intrinsic level, E_i, and the Fermi level, E_f, where the potential is set at zero.

The general solution of this equation for $\psi(r)$ and $E(r)$ is given by:

$$\psi(r)=-\frac{\rho}{4\varepsilon}r^2+C_1\ln(r)+C_2 \tag{7.2}$$

$$E(r)=-\frac{d\psi}{dr}=\frac{\rho}{2\varepsilon}r-\frac{C_1}{r} \tag{7.3}$$

where C_1 and C_2 are constants. Since the boundary conditions are different in the p- and n-doped regions, these constants will also be different in each region (i.e. C_{1a} and C_{2a} for the p-doped core, C_{1b} and C_{2b} for the n-doped shell). To write Eqns (7.2) and (7.3) explicitly, two tasks must be performed: an expression for ρ must be found, and boundary conditions of continuous potential and electric field must be imposed on each boundary in the NW.

Since there are two possible depletion cases for the core (fully or partially depleted core) and two possible depletion cases for the shell (fully or partially depleted shell), there are four total depletion cases for the radial pn junction NW. It will become clear in the following sections that each case subjects Eqns. (7.2) and (7.3) to different boundary conditions thereby necessitating for each case to be solved separately.

7.2.1 Case 1: Partially Depleted P-core and N-shell

This simplest case as demonstrated by the band diagram in Figure 7.1 has several characteristics. Firstly, this is the case whereby the space charge region (SCR) in the n-doped shell from the pn junction does not overlap with the SCR in the n-doped shell from the surface depletion. Referring to Figure 7.1, this can be written quantitatively as $r_s > r_n$ where r_s and r_n are the radii demarking the edges of the quasi-neutral region (QNR) in the shell. Secondly, this is the case whereby the p-doped core is not fully depleted. Quantitatively, this can be written as $r_p > 0$ where r_p is the edge of the QNR in the core. Hence, this case dictates that in both the core and shell regions, there exists a QNR. This case is only applicable for NWs whereby some finite QNR, albeit extremely thin in some cases, exists in each region.

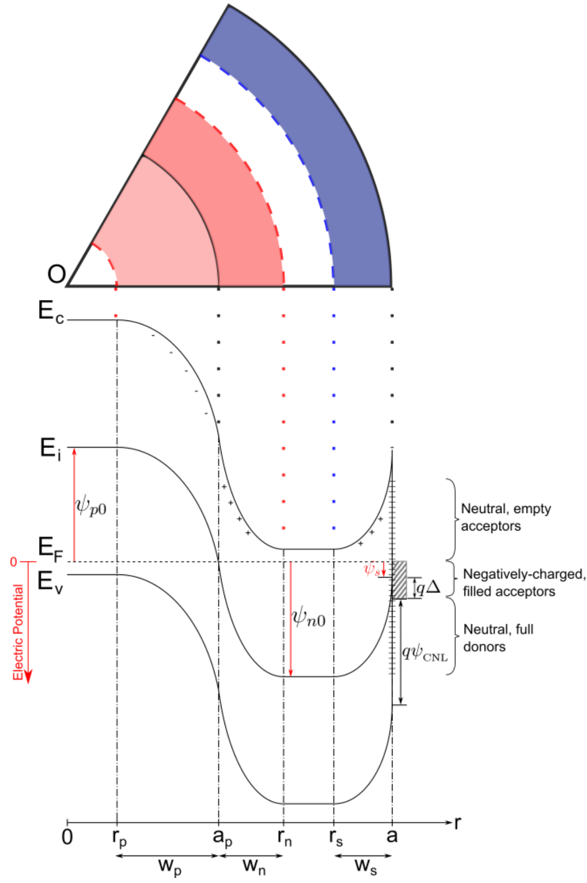

Figure 7.1: Schematic (top) of a NW slice where O is the centre of the NW and the corresponding energy band diagram (bottom) for Case 1 of a p-core/n-shell NW.

Using the full depletion and complete ionization approximations, it is straightforward to fully express the charge density as:

$$\rho = \begin{cases} 0 & \text{for} \quad 0 < r < r_p \\ -qN_A & \text{for} \quad r_p < r < a_p \\ +qN_D & \text{for} \quad a_p < r < r_n \\ 0 & \text{for} \quad r_n < r < r_s \\ +qN_D & \text{for} \quad r_s < r < a \end{cases} \tag{7.4}$$

where a_p is the core radius, a is the NW radius, N_A is the acceptor concentration in the p-core, N_D is the donor concentration in the n-shell and q is the elementary charge.

7.2.1.1 P-doped Core

To find C_{1a} and C_{2a}, both Neumann and Dirichlet boundary conditions must be imposed on Eqns. (7.2) and (7.3). To impose the Neumann boundary condition, it is assumed that $E = 0$ in the QNR (between $0 < r < r_p$) and that the E-field is continuous throughout the p-doped core since there are no surface or interface charge densities. Mathematically, this gives the Neumann boundary condition:

$$\text{B.C. 1a: } E(r = r_p) = 0 \tag{7.5}$$

Substituting Eqn. (7.5) into Eqn. (7.3) allows C_{1a} to be determined, giving:

$$E(r) = -\frac{qN_A}{2\varepsilon r}\left(r^2 - r_p^2\right) \quad \text{for} \quad r_p < r < a_p \tag{7.6}$$

To impose the Dirichlet boundary condition, it is assumed that $\psi = \psi_{p0}$ (see Figure 7.1) in the QNR (between $0 < r < r_p$) and that ψ is continuous throughout the p-doped core (otherwise $E = \infty$ at discontinuities). ψ_{p0} is given by Fermi-Dirac statistics as in bulk p-type material. This gives the boundary condition:

$$\text{B.C. 2a: } \psi(r = r_p) = \psi_{p0} \tag{7.7}$$

Substituting Eqn. (7.7) into Eqn. (7.2) allows C_{2a} to be determined, giving:

$$\psi(r) = \psi_{p0} - \frac{qN_A r_p^2}{2\varepsilon}\left[-\frac{r^2}{2r_p^2} + \ln\left(\frac{r}{r_p}\right) + \frac{1}{2}\right] \quad \text{for} \quad r_p < r < a_p \tag{7.8}$$

7.2.1.2 N-doped Shell

To impose the Neumann boundary condition, it is assumed that $E = 0$ in the quasi-neutral region (between $r_n < r < r_s$) and that the E-field is continuous at $r = r_n$:

$$\text{B.C. 1b: } E(r = r_n) = 0 \tag{7.9}$$

Substituting Eqn. (7.9) into Eqn. (7.3) determines C_{1b}, giving:

$$E(r) = \frac{qN_D}{2\varepsilon r}\left(r^2 - r_n^2\right) \quad \text{for} \quad a_p < r < r_n \tag{7.10}$$

To impose the Dirichlet boundary condition, it is assumed that $\psi = \psi_{n0}$ in the quasi-neutral region (between $r_n < r < r_s$) and that ψ is continuous throughout the n-doped shell (otherwise $E = \infty$ at discontinuities):

$$\text{B.C. 2b: } \psi(r = r_n) = \psi_{n0} \tag{7.11}$$

ψ_{n0} is given by Fermi-Dirac statistics as in bulk n-type material. Substituting Eqn. (7.11) into Eqn. (7.2) determines C_{2b}, giving:

$$\psi(r) = \psi_{n0} + \frac{qN_D r_n^2}{2\varepsilon}\left[-\frac{r^2}{2r_n^2} + \ln\left(\frac{r}{r_n}\right) + \frac{1}{2}\right] \quad \text{for} \quad a_p < r < r_n \tag{7.12}$$

A similar analysis at the $r = r_s$ boundary gives:

$$E(r) = \frac{qN_D}{2\varepsilon r}\left(r^2 - r_s^2\right) \quad \text{for} \quad r_s < r < a \tag{7.13}$$

$$\psi(r)=\psi_{n0}+\frac{qN_D r_s^2}{2\varepsilon}\left[-\frac{r^2}{2r_s^2}+\ln\left(\frac{r}{r_s}\right)+\frac{1}{2}\right] \quad \text{for} \quad r_s<r<a \tag{7.14}$$

Combining Eqns. (7.6), (7.10) and (7.13) gives a complete expression for the electric field varying radially in a NW:

$$E(r)=\begin{cases} 0 & \text{for } 0<r<r_p \\ -\dfrac{qN_A}{2\varepsilon r}\left(r^2-r_p^2\right) & \text{for } r_p<r<a_p \\ -\dfrac{qN_D}{2\varepsilon r}\left(r_n^2-r^2\right) & \text{for } a_p<r<r_n \\ 0 & \text{for } r_n<r<r_s \\ \dfrac{qN_D}{2\varepsilon r}\left(r^2-r_s^2\right) & \text{for } r_s<r<a \end{cases} \tag{7.15}$$

Combining Eqns. (7.8), (7.12) and (7.14) gives a complete expression for the potential varying radially in a NW:

$$\psi(r)=\begin{cases} \psi_{p0} & \text{for } 0<r<r_p \\ \psi_{p0}-\dfrac{qN_A r_p^2}{2\varepsilon}\left[-\dfrac{r^2}{2r_p^2}+\ln\left(\dfrac{r}{r_p}\right)+\dfrac{1}{2}\right] & \text{for } r_p<r<a_p \\ \psi_{n0}+\dfrac{qN_D r_n^2}{2\varepsilon}\left[-\dfrac{r^2}{2r_n^2}+\ln\left(\dfrac{r}{r_n}\right)+\dfrac{1}{2}\right] & \text{for } a_p<r<r_n \\ \psi_{n0} & \text{for } r_n<r<r_s \\ \psi_{n0}+\dfrac{qN_D r_s^2}{2\varepsilon}\left[-\dfrac{r^2}{2r_s^2}+\ln\left(\dfrac{r}{r_s}\right)+\dfrac{1}{2}\right] & \text{for } r_s<r<a \end{cases} \tag{7.16}$$

For a NW of known a, a_p, N_A and N_D, $\psi(r)$ and $E(r)$ can only be explicitly expressed if r_p, r_n and r_s are found. The solution for r_s has been shown in Chapter 5 to be the solution to the transcendental equation:

$$\frac{N_D\left(a^2-r_s^2\right)}{2aqD_{it}}-\Delta=\frac{qN_Dr_s^2}{2\varepsilon}\left[-\frac{a^2}{2r_s^2}+\ln\left(\frac{a}{r_s}\right)+\frac{1}{2}\right]+\psi_{n0} \quad (7.17)$$

where D_{it} is the density of interface states at the NW surface and $\Delta=\frac{E_g}{2q}-\psi_{\mathrm{CNL}}$ where ψ_{CNL} is the charge neutrality level (CNL) and E_g is the energy bandgap of the NW.

Finally, r_p and r_n can be found by applying boundary conditions of continuous ψ and *E* at the pn junction boundary ($r=a_p$) as described in the following section.

7.2.1.3 PN Junction Boundary

To impose the Neumann boundary condition, it is assumed that E is continuous at the junction, $r=a_p$:

$$\text{B.C. 3: } E^-(r=a_p)=E^+(r=a_p) \quad (7.18)$$

Therefore, using Eq. (15):

$$N_A\left(a_p^2-r_p^2\right)=N_D\left(r_n^2-a_p^2\right) \quad (7.19)$$

It is clear that this is simply a restatement of charge neutrality. Eqn. (7.19) can be rearranged to give r_n as a function of r_p :

$$r_n=\sqrt{a_p^2+\frac{N_A}{N_D}\left(a_p^2-r_p^2\right)} \quad (7.20)$$

It remains to determine r_p as follows.

To impose the Dirichlet boundary condition, it is assumed that ψ is continuous at the junction, $r = a_p$:

$$\text{B.C. 4: } \psi^-(r = a_p) = \psi^+(r = a_p) \quad (7.21)$$

Therefore,

$$\therefore \psi_{p0} - \frac{qN_A r_p^2}{2\varepsilon}\left[-\frac{a_p^2}{2r_p^2} + \ln\left(\frac{a_p}{r_p}\right) + \frac{1}{2}\right] = \psi_{n0} + \frac{qN_D r_n^2}{2\varepsilon}\left[-\frac{a_p^2}{2r_n^2} + \ln\left(\frac{a_p}{r_n}\right) + \frac{1}{2}\right] \quad (7.22)$$

This equation can be rearranged and simplified to give the built-in potential as

$$V_{bi} \equiv \psi_{n0} - \psi_{p0} = \frac{e}{4\varepsilon}\left[N_D r_n^2\left(2\ln\left(\frac{r_n}{a_p}\right) - 1\right) + a_p^2(N_a + N_d) + N_a r_p^2\left(2\ln\left(\frac{r_p}{a_p}\right) - 1\right)\right] \quad (7.23)$$

Eqn. (7.20) can be substituted into Eqn. (7.23) to yield a transcendental equation in r_p. With r_p found, r_n can be easily determined by Eqn. (7.20).

7.2.2 Case 2: Fully Depleted P-core and Partially Depleted N-shell

In this case, like Case 1, the junction SCR and surface SCR in the n-doped shell do not overlap such that $r_s > r_n$. Unlike Case 1, the p-doped core is fully depleted such that $r_p = 0$.

Using the full depletion and complete ionization approximations, the charge density is given by

$$\rho = \begin{cases} -qN_A & \text{for } 0 < r < a_p \\ +qN_D & \text{for } a_p < r < r_n \\ 0 & \text{for } r_n < r < r_s \\ +qN_D & \text{for } r_s < r < a \end{cases} \quad (7.24)$$

7.2.2.1 P-doped Core

Similar to Case 1, the Neumann and Dirichlet boundary conditions assume that $E=0$ and $\psi = \psi'_{p0}$ at the centre of the NW (at r = 0) due to the symmetry of the NW. This gives:

$$\text{B.C. 1a: } E(r=0)=0 \quad (7.25)$$

$$\text{B.C. 2a: } \psi(r=0)=\psi'_{p0} \quad (7.26)$$

It is noted that $\psi'_{p0} \neq \psi_{p0}$ under full depletion of the core. Invoking these boundary conditions yields

$$E(r) = -\frac{qN_A}{2\varepsilon} r \quad \text{for} \quad 0 < r < a_p \quad (7.27)$$

$$\psi(r) = \frac{qN_A}{4\varepsilon} r^2 + \psi'_{p0} \quad \text{for} \quad 0 < r < a_p \quad (7.28)$$

7.2.2.2 N-doped Shell

For the partially depleted n-shell in this case, the boundary conditions are the same as those for the n-shell of Case 1. As such, $E(r)$ and $\psi(r)$ are given by Eqn. (7.10) and (7.12) at the junction and by Eqn. (7.13) and (7.14) at the surface.

Combining Eqns. (7.27), (7.10) and (7.13) gives a complete expression for the electric field varying radially in a NW:

$$E(r) = \begin{cases} -\dfrac{qN_A}{2\varepsilon} r & \text{for } 0 < r < a_p \\ -\dfrac{qN_D}{2\varepsilon r}\left(r_n^2 - r^2\right) & \text{for } a_p < r < r_n \\ 0 & \text{for } r_n < r < r_s \\ \dfrac{qN_D}{2\varepsilon r}\left(r^2 - r_s^2\right) & \text{for } r_s < r < a \end{cases} \tag{7.29}$$

Combining Eqns. (7.28), (7.12) and (7.14) gives a complete expression for the potential varying radially in a NW:

$$\psi(r) = \begin{cases} \psi'_{p0} + \dfrac{qN_A}{4\varepsilon} r^2 & \text{for } 0 < r < a_p \\ \psi_{n0} + \dfrac{qN_D r_n^2}{2\varepsilon}\left[-\dfrac{r^2}{2r_n^2} + \ln\left(\dfrac{r}{r_n}\right) + \dfrac{1}{2}\right] & \text{for } a_p < r < r_n \\ \psi_{n0} & \text{for } r_n < r < r_s \\ \psi_{n0} + \dfrac{qN_D r_s^2}{2\varepsilon}\left[-\dfrac{r^2}{2r_s^2} + \ln\left(\dfrac{r}{r_s}\right) + \dfrac{1}{2}\right] & \text{for } r_s < r < a \end{cases} \tag{7.30}$$

For a NW of known a, a_p, N_A and N_D, $\psi(r)$ and $E(r)$ can be explicitly expressed if r_n, r_s and ψ'_{p0} are found. r_s is found by solving Eqn. (7.17). Similar to Case 1, ψ'_{p0} and r_n can be found by applying boundary conditions of continuous ψ and *E* at the pn junction boundary ($r = a_p$).

7.2.2.3 PN Junction Boundary

Similar to Case 1, the Neumann and Dirichlet boundary conditions given by Eqns. (7.18) and (7.21) are imposed to give:

$$r_n = a_p \sqrt{\frac{N_A}{N_D} + 1} \tag{7.31}$$

$$\psi'_{p0} = \psi_{n0} + \frac{qN_D r_n^2}{2\varepsilon}\left[-\frac{a_p^2}{2r_n^2} + \ln\left(\frac{a_p}{r_n}\right) + \frac{1}{2}\right] - \frac{qN_A}{4\varepsilon} a_p^2 \tag{7.32}$$

Eqn. (7.31) is equivalent to Eqn. (7.20), but with $r_p = 0$. Since a_p, N_A and N_D are known, r_n can be immediately determined from Eqn. (7.31) and substituted into Eqn. (7.32) to determine ψ'_{p0}.

7.2.3 Case 3: Partially Depleted P-core and Fully Depleted N-shell

In this case, like Case 1, the p-doped core is partially depleted such that $r_p > 0$. Unlike Case 1, the junction SCR and surface SCR in the n-doped shell overlap such that $r_s < r_n$.

Using the full depletion and complete ionization approximations, the charge density is given by

$$\rho = \begin{cases} 0 & \text{for} \quad 0 < r < r_p \\ -qN_A & \text{for} \quad r_p < r < a_p \\ +qN_D & \text{for} \quad a_p < r < a \end{cases} \tag{7.33}$$

7.2.3.1 P-doped Core

For the partially depleted p-core in this case, the boundary conditions are the same as those for the p-core of Case 1. As such, $E(r)$ and $\psi(r)$ are given by Eqn. (7.6) and (7.8) in the SCR.

7.2.3.2 N-doped Shell

To impose Neumann and Dirichlet boundary conditions, it is assumed that there exists some $r_0 > a_p$ where $E = 0$ and $\psi = \psi'_{n0}$. This gives:

$$\text{B.C. 1a: } E(r = r_0) = 0 \tag{7.34}$$

$$\text{B.C. 2a: } \psi(r = r_0) = \psi'_{n0} \tag{7.35}$$

It is noted that $\psi'_{n0} \neq \psi_{n0}$ under full depletion of the shell. If $a_p < r_0 < a$, these boundary conditions merely assert that r_0 is the position in which $E(r)$ changes sign from negative to positive as r crosses from the SCR of the junction to the SCR of the surface. Since E must be continuous, E must be zero at r_0. As such, r_0 marks the boundary between the SCR of the junction and the surface. Invoking these boundary conditions yields:

$$E(r) = \frac{qN_D}{2\varepsilon r}\left(r^2 - r_0^2\right) \quad \text{for} \quad a_p < r < a \tag{7.36}$$

$$\psi(r) = \psi'_{n0} + \frac{qN_D r_0^2}{2\varepsilon}\left[-\frac{r^2}{2r_0^2} + \ln\left(\frac{r}{r_0}\right) + \frac{1}{2}\right] \quad \text{for} \quad a_p < r < a \tag{7.37}$$

Combining Eqns. (7.6) and (7.36) gives a complete expression for the electric field varying radially in a NW:

$$E(r) = \begin{cases} 0 & \text{for } 0 < r < r_p \\ -\dfrac{qN_A}{2\varepsilon r}\left(r^2 - r_p^2\right) & \text{for } r_p < r < a_p \\ -\dfrac{qN_D}{2\varepsilon r}\left(r_0^2 - r^2\right) & \text{for } a_p < r < a \end{cases} \tag{7.38}$$

Combining Eqns. (7.8) and (7.37) gives a complete expression for the potential varying radially in a NW:

$$\psi(r) = \begin{cases} \psi_{p0} & \text{for } 0 < r < r_p \\ \psi_{p0} - \dfrac{qN_A r_p^2}{2\varepsilon}\left[-\dfrac{r^2}{2r_p^2} + \ln\left(\dfrac{r}{r_p}\right) + \dfrac{1}{2}\right] & \text{for } r_p < r < a_p \\ \psi'_{n0} + \dfrac{qN_D r_0^2}{2\varepsilon}\left[-\dfrac{r^2}{2r_0^2} + \ln\left(\dfrac{r}{r_0}\right) + \dfrac{1}{2}\right] & \text{for } a_p < r < a \end{cases} \tag{7.39}$$

For a NW of known a, a_p, N_A and N_D, $\psi(r)$ and $E(r)$ can be explicitly expressed if r_p, r_0 and ψ'_{n0} are found. r_p, r_0 and ψ'_{n0} are found by imposing boundary conditions at the pn junction and examining the surface potential as follows.

7.2.3.3 PN Junction Boundary

Again, it is assumed that *E* and ψ are continuous at the junction, $r = a_p$. Mathematically, this takes the same form as Eqns. (7.18) and (7.21). Imposing these boundary conditions gives:

$$r_0 = \sqrt{a_p^2 + \frac{N_A}{N_D}\left(a_p^2 - r_p^2\right)} \tag{7.40}$$

$$\psi'_{n0} = \psi_{p0} - \frac{qN_A r_p^2}{2\varepsilon}\left[-\frac{a_p^2}{2r_p^2} + \ln\left(\frac{a_p}{r_p}\right) + \frac{1}{2}\right] - \frac{qN_D r_0^2}{2\varepsilon}\left[-\frac{a_p^2}{2r_0^2} + \ln\left(\frac{a_p}{r_0}\right) + \frac{1}{2}\right] \tag{7.41}$$

Finally, r_p is determined by examining the surface potential as follows.

7.2.3.4 NW Surface Potential

According to Eqn. (7.39), the surface potential is given by:

$$\psi_s \equiv \psi(r = a) = \psi'_{n0} + \frac{qN_D r_0^2}{2\varepsilon}\left[-\frac{a^2}{2r_0^2} + \ln\left(\frac{a}{r_0}\right) + \frac{1}{2}\right] \tag{7.42}$$

ψ_s can be found independently by analyzing the surface charge. Assuming a uniform density of interface states [36], the surface charge is given by:

$$Q_{it} = -q^2 D_{it}(\psi_s + \Delta) \tag{7.43}$$

Charge neutrality throughout the NW states that:

$$N_D(a^2 - a_p^2) - N_A(a_p^2 - r_p^2) - 2aqD_{it}(\psi_s + \Delta) = 0 \tag{7.44}$$

As such, the surface potential can be written as

$$\psi_s = \frac{N_D(a^2 - a_p^2) - N_A(a_p^2 - r_p^2)}{2aqD_{it}} - \Delta \tag{7.45}$$

For a NW of known a, a_p, N_A, N_D and D_{it}, it is clear that Eqns. (7.40), (7.41) and (7.45) are functions of r_p alone and can be substituted into Eqn. (7.42) to form a

transcendental equation that can be solved to give r_p. r_0 can subsequently be determined by Eqn. (7.40) and ψ'_{n0} can finally be determined by Eqn. (7.41) to give an explicit expression for $\psi(r)$ and $E(r)$ given in Eqns. (7.38) and (7.39).

7.2.4 Case 4: Fully Depleted P-core and N-shell

In this case, like Case 2, the p-doped core is fully depleted such that $r_p = 0$. Like Case 3, the junction SCR and surface SCR in the n-doped shell overlap such that $r_s < r_n$.

Using the full depletion and complete ionization approximations, the charge density is given by:

$$\rho = \begin{cases} -qN_A & \text{for} \quad 0 < r < a_p \\ +qN_D & \text{for} \quad a_p < r < a \end{cases} \tag{7.46}$$

7.2.4.1 P-doped Core

For the p-core in this case, the boundary conditions are the same as those for the p-core of Case 2. As such, $E(r)$ and $\psi(r)$ are given by Eqn. (7.27) and (7.28) in the SCR.

7.2.4.2 N-doped Shell

For the n-shell in this case, the boundary conditions are the same as those for the n-shell of Case 3. As such, $E(r)$ and $\psi(r)$ are given by Eqn. (7.36) and (7.37) in the SCR.

Combining Eqns. (7.27) and (7.36) gives a complete expression for the electric field varying radially in a NW:

$$E(r) = \begin{cases} -\dfrac{qN_A}{2\varepsilon} r & \text{for } 0 < r < a_p \\ -\dfrac{qN_D}{2\varepsilon r}\left(r_0^2 - r^2\right) & \text{for } a_p < r < a \end{cases} \tag{7.47}$$

Combining Eqns. (7.28) and (7.37) gives a complete expression for the potential varying radially in a NW:

$$\psi(r) = \begin{cases} \psi'_{p0} + \dfrac{qN_A}{4\varepsilon} r^2 & \text{for } 0 < r < a_p \\ \psi'_{n0} + \dfrac{qN_D r_0^2}{2\varepsilon}\left[-\dfrac{r^2}{2r_0^2} + \ln\left(\dfrac{r}{r_0}\right) + \dfrac{1}{2}\right] & \text{for } a_p < r < a \end{cases} \tag{7.48}$$

For a NW of known a, a_p, N_A and N_D, $\psi(r)$ and $E(r)$ can be explicitly expressed if r_0, ψ'_{p0} and ψ'_{n0} are found. These can be found by imposing boundary conditions at the pn junction and examining the surface potential as follows.

7.2.4.3 PN Junction Boundary

Again, it is assumed that *E* and ψ are continuous at the junction, $r = a_p$. Mathematically, this takes the same form as Eqns. (7.18) and (7.21). Imposing these boundary conditions gives:

$$r_0 = a_p \sqrt{\frac{N_A}{N_D} + 1} \tag{7.49}$$

$$\psi'_{p0} = \psi'_{n0} + \frac{qN_D r_0^2}{2\varepsilon}\left[-\frac{a_p^2}{2r_0^2} + \ln\left(\frac{a_p}{r_0}\right) + \frac{1}{2}\right] - \frac{qN_A}{4\varepsilon} a_p^2 \tag{7.50}$$

Finally, ψ'_{n0} is determined by examining the surface potential as follows.

7.2.4.4 NW Surface Potential

According to Eqn. (7.48), the surface potential is identical to Eqn. (7.42). Using a similar approach to Case 3, the charge neutrality at the surface can be invoked to yield the same equation as Eqn. (7.45) but with $r_p = 0$:

$$\psi_s = \frac{N_D(a^2 - a_p^2) - N_A a_p^2}{2aqD_{it}} - \Delta \tag{7.51}$$

This equation can be substituted into Eqn. (7.42) to yield an explicit expression for ψ'_{n0}:

$$\psi'_{n0} = \frac{N_D(a^2 - a_p^2) - N_A a_p^2}{2aqD_{it}} - \Delta - \frac{qN_D r_0^2}{2\varepsilon}\left[-\frac{a^2}{2r_0^2} + \ln\left(\frac{a}{r_0}\right) + \frac{1}{2}\right] \tag{7.52}$$

For a NW of known a, a_p, N_A, N_D and D_{it}, r_0 can be explicitly determined from Eqn. (7.49), thus allowing the determination of ψ'_{n0} from Eqn. (7.52) and finally the determination of ψ'_{p0} from Eqn. (7.50). An explicit expression for $\psi(r)$ and $E(r)$ can then be written from Eqns. (7.48) and (7.50).

7.2.5 Classification into Cases Based on NW Parameters

Perhaps the most nontrivial task in modelling the electrostatics in a radial pn junction lies in the categorization of a NW parameter set into one of the four cases. For a NW of known a, a_p, N_A, N_D and D_{it}, the logic flowchart in Figure 7.2 outlines the classification of the cases.

In accordance with Figure 7.2a-b, r_s is first separately calculated as a basis for comparison to r_n calculated later (See Figure 7.2f,h). Here, the p-doped core is ignored and the overall critical radius, a_{crit}, is calculated by solving Eqn. (7.17) for a in the limit of r_s approaching zero (Figure 7.2a). As discussed in Chapter 5, this gives the minimum NW radius before which a uniformly n-doped NW is completely depleted. If $a > a_{crit}$, r_s can be calculated from Eqn. (7.17) (See Figure 7.2b). Conversely, if $a < a_{crit}$, the NW shell will be fully depleted regardless of the size of the core. As such, r_s is set to zero.

With r_s calculated, NW parameter sets can be classified into one of the four cases in accordance with Figure 7.2c-j. First, the critical p-core radius, $a_{p,crit}$, is found by

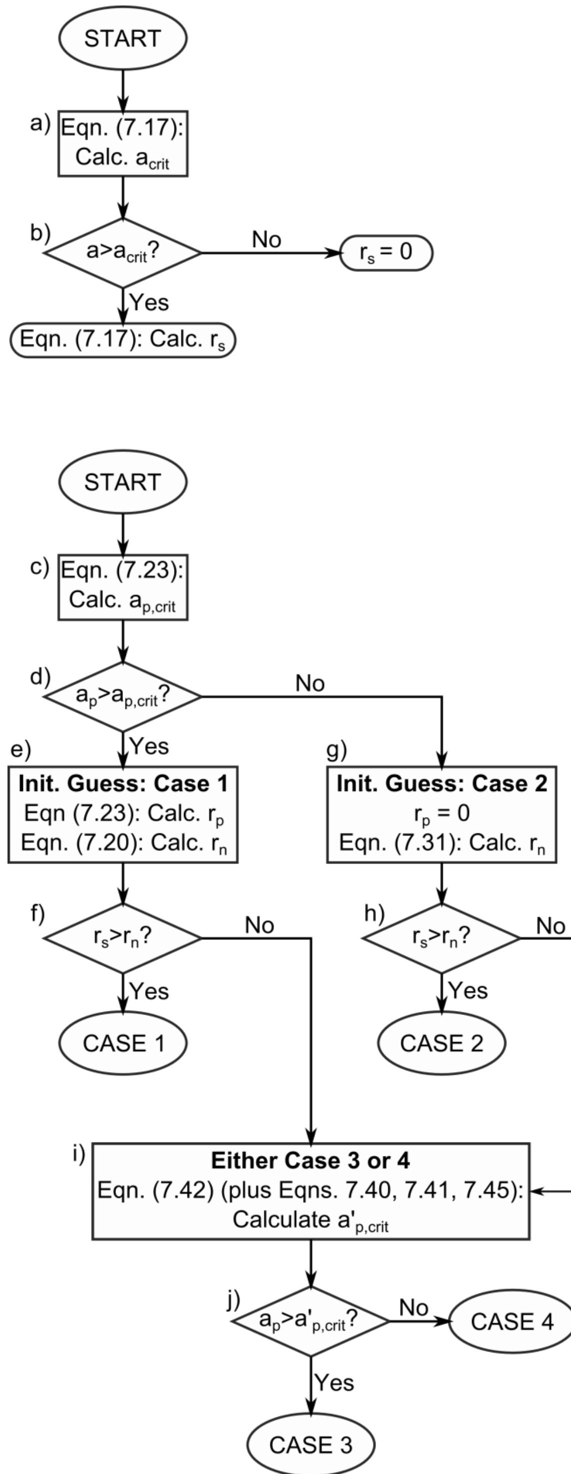

Figure 7.2: Logic flowchart outlining the classification of a NW with arbitrary a, a_p, N_A, N_D and D_{it} into each of the four depletion cases

solving Eqn. (7.23) (with Eqn. (7.20) substituted in) for a in the limit of r_p approaching zero (Figure 7.2c). This critical p-core radius is the minimum a_p before a NW will transition from Case 1 to Case 2.

If $a > a_{p,crit}$ (Figure 7.2d), an initial guess can be made that this NW belongs to Case 1 (Figure 7.2e). To verify this, r_p and r_n can be calculated from Eqn. (7.23) and (7.20) respectively. Then, r_n can be compared to the previously calculated r_s. If $r_s > r_n$ (Figure 7.2f), the junction SCR and surface SCR do not overlap, thus validating the initial Case 1 guess by satisfying both conditions ($a_p > a_{p,crit}$ and $r_s > r_n$). This NW would then belong to Case 1.

If $a < a_{p,crit}$ (Figure 7.2d), an initial guess can be made that this NW belongs to Case 2 (Figure 7.2g). To test this initial guess, r_p is set to zero in accordance with Case 2 and r_n is calculated from Eqn. (7.31). Similar to Figure 7.2f, if $r_s > r_n$ (Figure 7.2h), the junction SCR and surface SCR do not overlap, thus validating the initial Case 2 guess by satisfying both conditions ($a_p < a_{p,crit}$ and $r_s > r_n$). This NW would then belong to Case 2.

It is clear then, that all Case 1 and 2 NWs will be successfully categorized if $r_s > r_n$. As such, if $r_s < r_n$ (Figure 7.2f,h), the NW must be either Case 3 or 4 . To discern between Case 3 and Case 4 NWs, a new $a_{p,crit}$ must be found because the previously

calculated $a_{p,crit}$ is derived from Eqn. (7.23) which does not apply to Cases 3 and 4. As such, this new $a'_{p,crit}$ can be calculated by solving Eqn. (7.42) (with Eqns. (7.40), (7.41) and (7.45) substituted in) for a in the limit of r_p approaching zero (Figure 7.2i). From this, it is clear that $a'_{p,crit}$ is the minimum a_p before a NW will transition from Case 3 to Case 4. As such, if $a_p > a'_{p,crit}$ (Figure 7.2j), the core is only partially depleted and the NW belongs to Case 3. Conversely, if $a_p < a'_{p,crit}$, the core is fully depleted and the NW belongs to Case 4.

7.3 Results and Analysis

With this model, any NW of known a, a_p, N_A, N_D and D_{it} can be classified into a particular case with a full expression for the electric field and potential varying radially in the NW. To analyze the general output of the model, GaAs was chosen as the NW material and the various cases (1-4) as a function of a_p and a were displayed as a contour plot for various N_A, N_D and D_{it} values as shown in Figure 7.3. For simplicity, Figure 7.3 shows the specific cases where $N \equiv N_A = N_D$, although the results can obviously be generalized for any N_A and N_D. To better understand the model results, specific parameters marked by the lettered points in Figure 7.3 (typical $D_{it} = 10^{13}$ cm^{-2}eV^{-1} and $N = 10^{18}$ cm^{-3}) are examined alongside the corresponding lettered band diagrams shown in Figure 7.4.

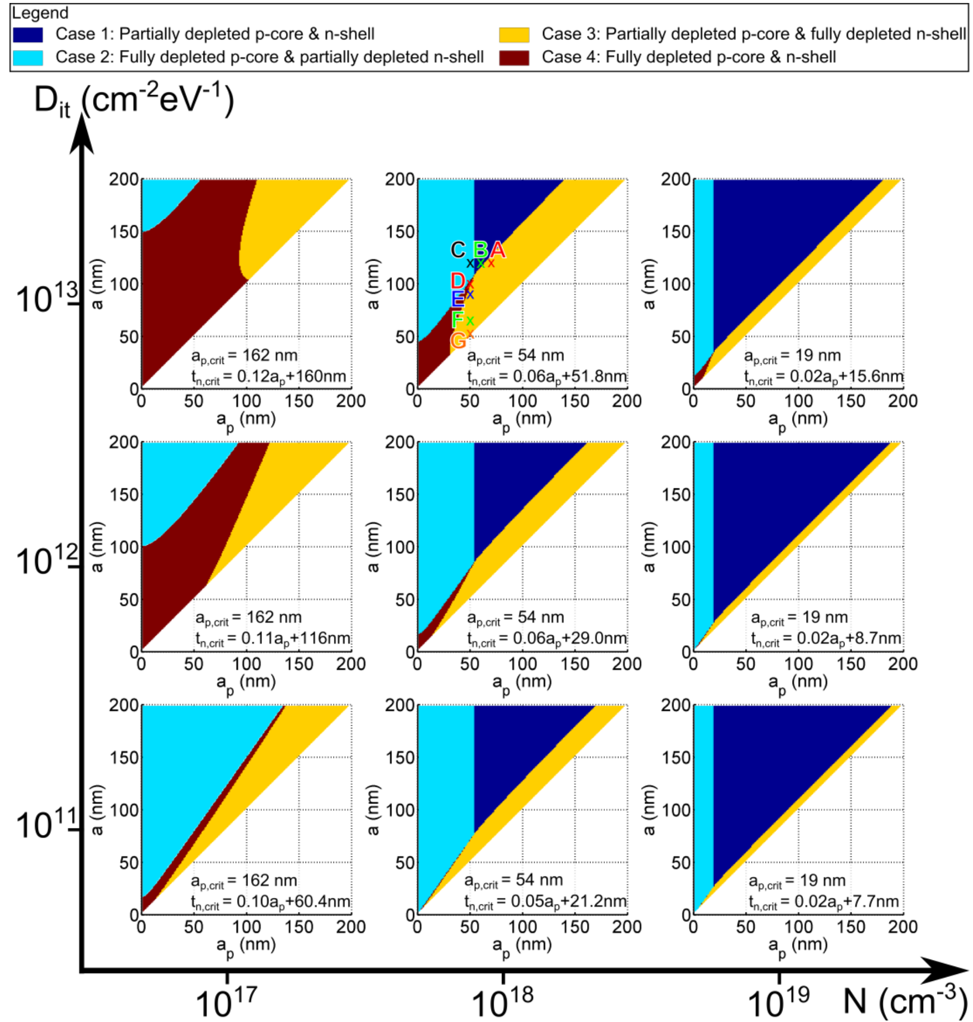

Figure 7.3: Contour plots showing the case (1-4) as a function of *a* and a_p. Different rows and columns in the matrix correspond to different D_{it} and $N \equiv N_A = N_D$, respectively. The minimum critical core radius ($a_{p,crit}$) and shell thickness ($t_{n,crit}$) to maintain Case 1 NWs are also shown in each plot.

Point B ($a_p = 60$ nm, $a = 120$ nm) belongs to Case 1 (blue region) and most resembles the bulk situation whereby a quasi-neutral region exists in both the core and shell. Keeping a fixed total radius, $a = 120$ nm, the core is enlarged while the shell thickness is reduced to result in Point A ($a_p = 70$ nm, $a = 120$ nm) belonging to Case 3

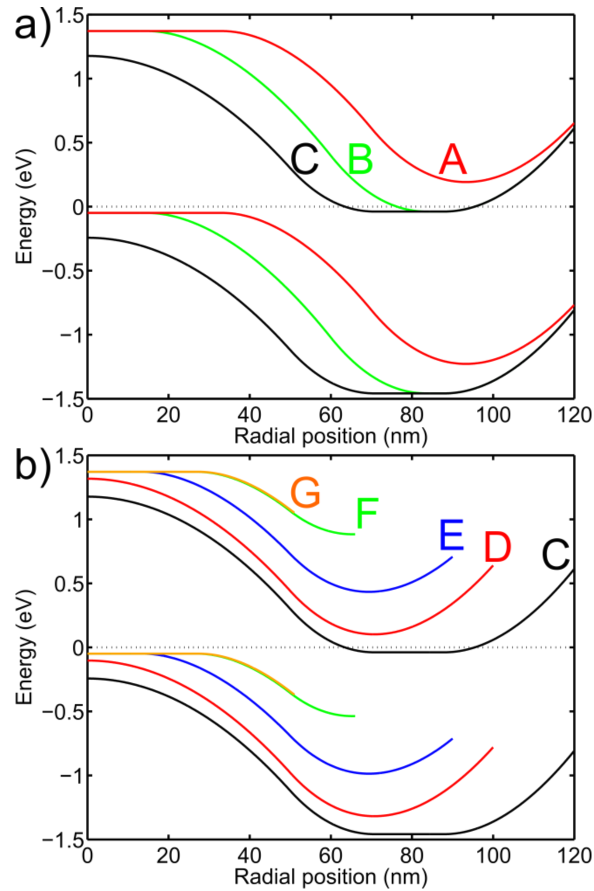

Figure 7.4: Band diagrams of different (a_p, a) coordinates corresponding to the lettered points in Figure 7.3 (for a typical $D_{it} = 10^{13}$ cm^{-2}eV^{-1} and $N = 10^{18}$ cm^{-3}). The Fermi level for each band diagram is given by the dashed line along the horizontal axis. The (a_p, a) coordinates (in units of nm) are A: (70,120), B: (60,120), C: (50,120), D: (50,100), E: (50,90), F: (50,66), G: (50,51).

(yellow region). It is clear from Figure 7.4a that the shell of the Point A NW is completely depleted, thus causing the Fermi level in the shell to move further from the conduction band (CB) edge compared to case B. Conversely, if the core radius is reduced while the shell is enlarged relative to Point B, then Point C ($a_p = 50$ nm, $a = 120$ nm) belonging to Case 2 is reached. From Figure 7.4a, it is clear that the core of the Point C NW is

completely depleted and the Fermi level in the core is further from the valence band (VB) edge than for Point B. It is readily apparent that the complete depletion of either the shell (Point A) or core (Point C) will lead to a reduction in the built-in potential.

To extend the analysis, NWs of fixed core radius, $a_p = 50$ nm (Points C to G) can be examined. Using Point C as a starting point, a can be reduced to 100 nm to reach Point D belonging to Case 4. This Case 4 classification can be clearly seen in Figure 7.4b where no quasi-neutral region in present for the Point D NW and the Fermi level is further from the CB edge in the shell compared to Point C. a can be further reduced to 90 nm to reach Point E belonging to Case 3. While it is not surprising that this thinner shell remains fully depleted, it is counterintuitive that the core with an unchanged size, while previously fully depleted, is now only partially depleted. This occurs as a result of the reduced shell material available to deplete the core. From Figure 7.4b, it is also clear that Point E is the situation whereby the Fermi level at the surface is pinned at midgap. If a is reduced further to 66 nm, Point F is reached where it remains in Case 3. This is the special situation where the Fermi level at the surface is pinned at the CNL (i.e. $\psi_s = -\Delta$) as per Eqns. (7.40) and (7.45). This implies that there is no surface charge according to Eqn (7.43) and hence, no electric field at the surface of the NW according to Eqn. (7.38). This is seen clearly in Figure 7.4b by the flat band at the surface. Finally, if the shell thickness is reduced to 1 nm such that $a = 51$ nm (Point G), the band diagram for a uniformly doped p-type NW is recovered. From Figure 7.4b, it is clear that the Fermi level at the surface lies below the CNL, thereby implying that the surface charge is

positive as is the case for p-type NWs. This differs from the negative surface charge of Points C to E. For all band diagrams in Figure 7.4b, the polarity of the surface charge is clearly reflected by the direction of the electric field at the surface. From the progression of Point C to Point G, the qualitative nature of the variable, r_0 becomes clear. For $a > r_0$, the surface states are filled with electrons and r_0 serves as a boundary between the junction SCR and surface SCR in the shell. For $a < r_0$, the surface states are filled with holes and the band diagram resembles that of a uniformly doped p-type NW since the shell is so thin Finally, the decreasing built-in potential, V_{bi}, from Point C to G can be readily observed.

From this discussion, Case 1 NWs are clearly desired to achieve a maximum V_{bi}. To confirm this, a corresponding matrix comprising contour plots of V_{bi} as a function of a_p and a can be generated as shown in Figure 7.5. A comparison between Figure 7.3 and Figure 7.5 shows that high built-in potential is only maintained in Case 1 NWs, outside of which the V_{bi} decreases rapidly.

It is clear from Figure 7.3 and Figure 7.5 that there exists a critical core radius , $a_{p,crit}$, above which the NW will be in Case 1. Additionally, there exists a critical shell thickness, $t_{n,crit}$, below which the shell will be completely depleted (Case 3 or 4). $a_{p,crit}$ and $t_{n,crit}$ for each plot are shown in Figure 7.3. In most cases, it can be seen that $t_{n,crit}$ has a slight linear dependence on a_p. By comparing the rows within both Figure 7.3 and

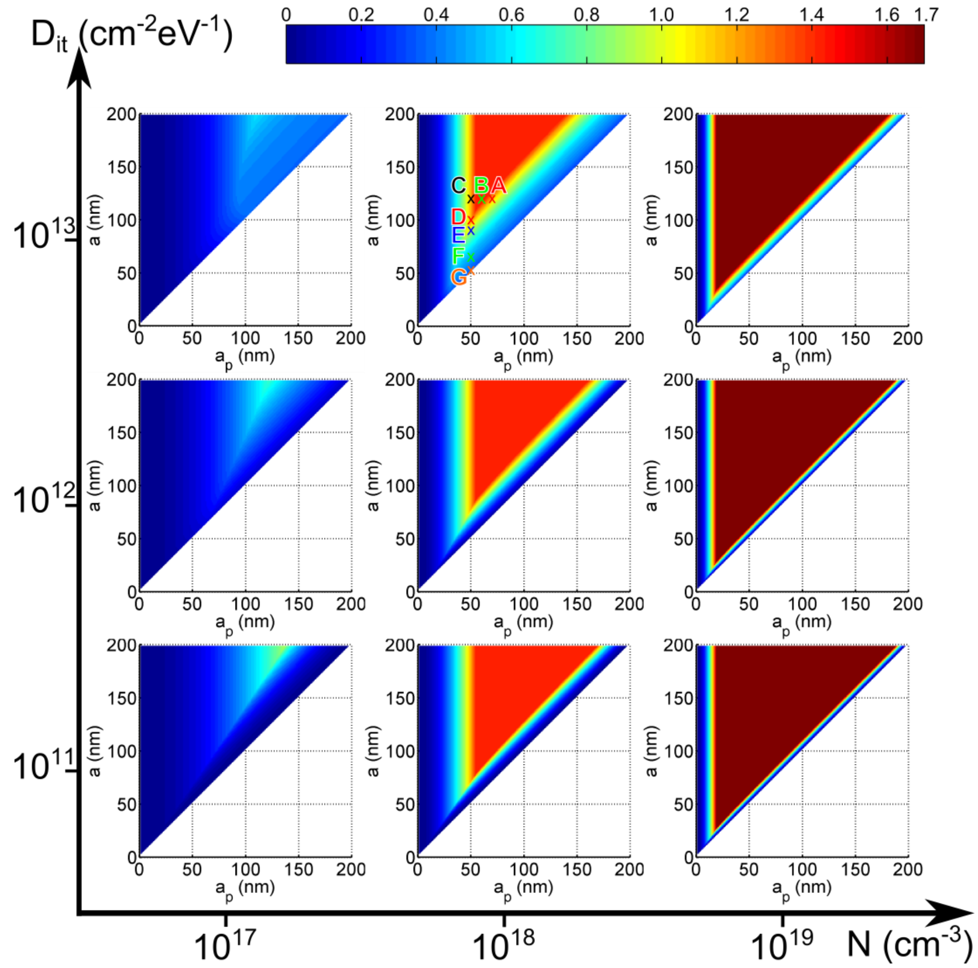

Figure 7.5: Contour plots showing the built-in potential as a function of *a* and a_p. Different rows and columns in the matrix correspond to different D_{it} and $N \equiv N_A = N_D$, respectively.

Figure 7.5, it can be seen that an increased D_{it} leads to an increased $t_{n,crit}$, increasing from ~24 nm to ~60 nm for $N = 10^{18}$ cm^{-3} and from ~8 nm to ~19 nm for $N = 10^{19}$ cm^{-3}. This is largely expected since a larger surface state density necessitates a thicker shell to prevent full depletion. Additionally, $a_{p,crit}$ is seen to be independent of D_{it}. If the columns within Figure 7.3 and Figure 7.5 are compared, it can be observed that an

increased N leads to both a significantly reduced $a_{p,crit}$ and $t_{n,crit}$. The reduced $a_{p,crit}$ can be attributed to the increased N_A, while the reduced $t_{n,crit}$ can be attributed to the increased N_D. This is confirmed by decoupling N_A and N_D as shown in Figure 7.6.

By comparing columns within Figure 7.6, it can be seen that the increased N_A leads to a reduced $a_{p,crit}$ as previously stated. Additionally, this also leads to an increased $t_{n,crit}$ since higher doped cores deplete the shell more heavily, thus necessitating a thicker shell. A two order of magnitude increase of N_A from 10^{17} cm^{-3} to 10^{19} cm^{-3} can be seen to cause an approximately one order of magnitude reduction in $a_{p,crit}$ from hundreds to tens of nanometers. By comparing rows within Figure 7.6, it is clear that an increased N_D leads to a significantly reduced $t_{n,crit}$ as previously stated as well as an increased $a_{p,crit}$ since higher doped shells deplete the core more heavily, thus necessitating a thicker core.

In addition to the general trends present in Figure 7.3, Figure 7.5 and Figure 7.6, several observations pertinent to device design can be made. Firstly, it can be seen that V_{bi} will be greatly reduced for a < 200 nm NWs if either the core, shell or both are doped at 10^{17} cm^{-3}. This holds true for a wide range of D_{it} values. Secondly, the blue Case 1 region in Figure 7.3 and corresponding red "high-V_{bi} region" in Figure 7.5 and Figure 7.6 are largest for high doping of both the core and shell.

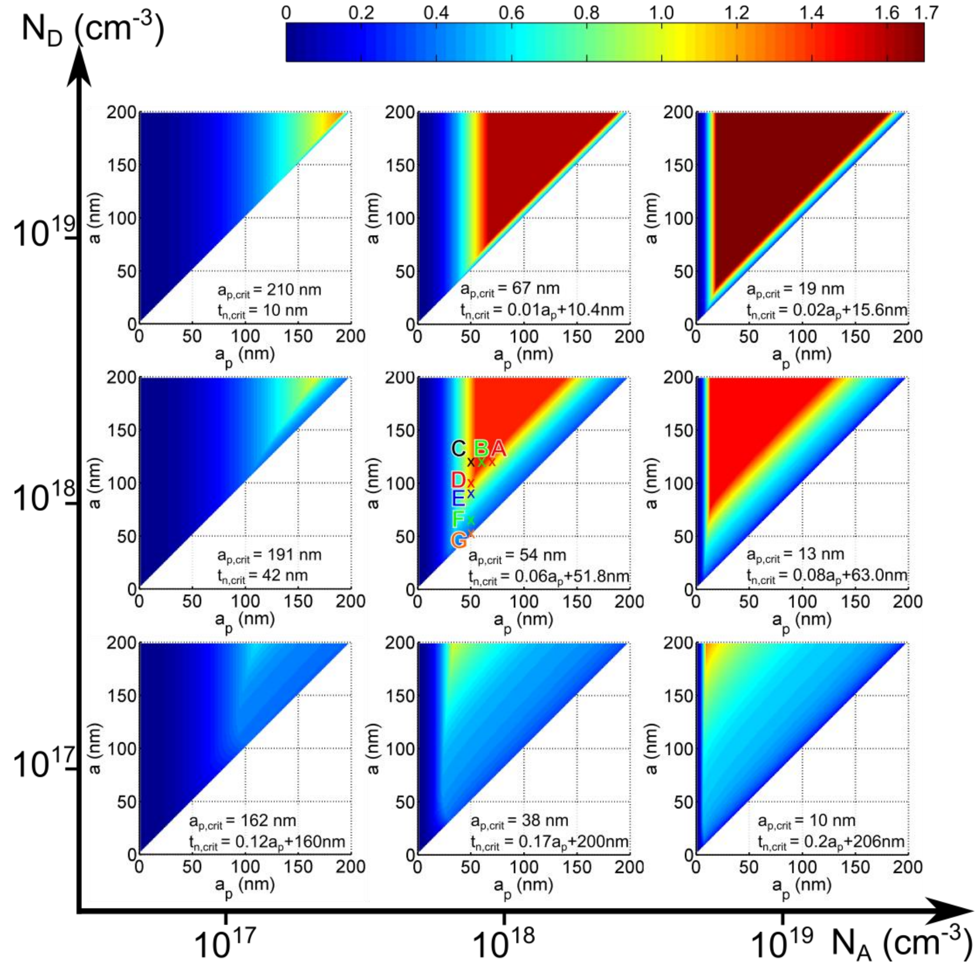

Figure 7.6: Contour plots showing the built-in potential as a function of *a* and a_p for a typical $D_{it} = 10^{13}$ cm^{-2}eV^{-1}. Different rows and columns in the matrix correspond to different N_D and N_A, respectively.

7.4 Discussion

In order to relate this model to practical radial pn junction NW devices, dimension and doping parameters are extracted from state-of-the-art radial pn junction GaAs NW solar cells as input into the model. Mariani et al [33] reported surface passivated GaAs pn junction NWs with $a_p = 90$ nm, $a = 130$ nm, $N_A = 10^{17}$ cm^{-3} and

$N_D = 10^{18}$ cm^{-3}, yielding a record 6.63% efficiency for GaAs NWs, but a relatively low open-circuit voltage (V_{oc}) of 0.44 V. Using these doping and dimension parameters along with $D_{it} = 10^{11}$ cm^{-2}eV^{-1} as fitting parameter, the model predicted $V_{bi} = 0.30$ V. However, if the core doping is modified slightly to $N_A = 1.5\times10^{17}$ cm^{-3}, $V_{bi} = 0.46$ V. This agrees well with the reported experimental value of $V_{oc} = 0.44$ V. This example illustrates the sensitivity of V_{bi} to slight N_A changes when the core is fully depleted.

With this model, a III-V radial pn junction NW ensemble grown on an inexpensive lattice-mismatched Si substrate can be proposed with the following NW parameters: $a_p = 50$ nm, $a = 90$ nm, $N = N_D = N_A = 2\times10^{18}$ cm^{-3} and assuming $D_{it} = 10^{12}$ cm^{-2}eV^{-1}. The specific NW geometry was based on a previous report [31] and is shown schematically in the inset of Figure 7.7. The core radius was chosen subject to two constraints: $a_p > a_{p,crit}$ to avoid full core depletion and a_p below the critical radius to avoid dislocations due to the lattice mismatch at the NW-substrate interface [14]. $a = 90$ nm was chosen because previous reports have demonstrated that maximum absorption is achieved at this total radius [106], while $D_{it} = 10^{12}$ cm^{-2}eV^{-1} represents a reasonable value under surface passivation. From Figure 7.7 plotted for $a_p = 50$ nm, $a = 90$ nm and $D_{it} = 10^{12}$ cm^{-2}eV^{-1}, it is clear that the NW will belong to the Case 1 region provided that N_A and N_D are on the order of 10^{18} cm^{-3}.

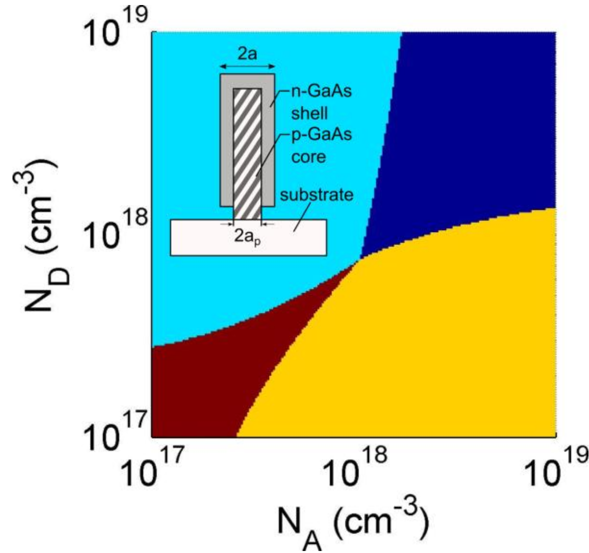

Figure 7.7: Contour plot showing the case (1-4) as a function of N_A and N_D for $a_p = 50$ nm, $a = 90$ nm, $D_{it} = 10^{12}$ cm^{-2}eV^{-1}. Inset: Schematic of proposed design.

7.5 Conclusion

In conclusion, a comprehensive solution to Poisson's equation for a radial pn junction NW with surface depletion has been found for each of the four depletion cases of the NW. By varying the core and shell dimensions in the model, interesting underlying physical behavior was found such as the change in the surface charge polarity (within Case 4) and a change in the core depletion width merely by changing the shell thickness. For device purposes, it was confirmed that V_{bi} rapidly degrades for NWs which do not belong to Case 1, thus stressing the need for a low $a_{p,crit}$ and $t_{n,crit}$. $t_{n,crit}$ increased with increasing D_{it}, while $a_{p,crit}$ was independent of D_{it}. When N_A increased, $a_{p,crit}$ decreased, while $t_{n,crit}$ increased. The opposite occurred for increasing N_D. The model

agreed well with state-of-the-art NW PV devices. Finally, a possible device design was proposed by taking material, optical and electrical constraints into consideration.

8 Conclusion and Future Work

8.1 Thesis Summary

In summary, five key issues facing current NW devices were addressed: poor contacts to NW ensemble devices, the lack of simple precise methods to evaluate doping in NWs, the need for a greater fundamental understanding of surface depletion, combating deleterious surface effects and the need for a thorough understanding of electrostatics in radial pn junction NWs.

With regards to NW contacting, the spincoating of a filling medium is deemed an ideal option for planarizing the front contacts while preventing shunt paths from the top contact to the substrate. Multiple filling materials were assessed for porosity, planarization and thermal stability, ultimately resulting in the choice of Cyclotene as an ideal filling material. Contact planarization was further improved by the novel approach of removing the tops of the NWs by sonication.

With regards to NW doping, SIMS was shown to be a valuable tool in not only being a simple and precise method to determine the impurity dopant concentration, but also characterizing the height uniformity in a NW ensemble. Moreover, this highly unique ability was shown to be easily extended to the analysis of the segment height uniformity for any arbitrary NW ensemble with axial heterostructures or homojunctions

(e.g. an axial p-n junction NW). Due to its simplicity, it makes for an ideal complimentary technique to the complex, yet powerful method of APT.

With regards to attaining a greater understanding of NW depletion, a thorough model of surface depletion was given for any NW of arbitrary D_{it}, a and N_D. This model yielded several features unique to NWs compared to films. Firstly, the NW is depleted evenly throughout the NW upon full depletion, causing the Fermi level to drop below the planar value. Secondly, the depletion width was found to be significantly larger than in thin films due to the increasing surface area to volume ratio for small radii. This enabled higher built-in potentials in NWs than possible in films. Thirdly, heavy depletion of the NW resulted in a severe degradation in NW conductivity, even causing inversion for thin and/or lightly doped NWs. Finally, the surface depletion model was validated by providing excellent fits to experimental SRXPS data of surface potentials.

With regards to the need to combat deleterious surface effects in NW devices, n-type GaAs NWs were effectively passivated with AlInP. I-V characteristics were measured for passivated and unpassivated ensemble NW devices and subsequently fit with a surface depletion, capacitance and transport model to show that the NWs exhibited a 55% decrease in surface state density upon passivation and an impressive four order of magnitude increase in the effective carrier concentration of the characteristic thick NWs. It was also found that the NWs with radii above the 99th percentile of the distribution dominated the I-V characteristics Furthermore, passivation was further confirmed by PL measurements showing a 20x improvement in PL intensity

and by TRPL measurements showing a 25x improvement of carrier lifetime upon passivation.

Finally, with regards to understanding the electrostatics in pn junction NWs, Poisson's equation was solved for a radial pn junction NWs for each of the four depletion cases of the NW. Interesting underlying physical behaviour was found such as surface polarity change and changing core depletion by merely varying shell thickness. The built-in potential was found to degrade rapidly upon full depletion of the core and/or shell, stressing the need to optimize the core and shell doping, while minimizing the surface state density to maintain a high built-in potential. The model agreed well with state-of-the-art NW PV devices. Finally, a possible device design was proposed by taking material, optical and electrical constraints into consideration.

8.2 Future Work

While this thesis provides a significant step towards addressing several key NW optoelectronic device issues, there remain many significant issues. Firstly, while the front contact sheet resistance was lowered in NW ensemble devices, it is still difficult to make ohmic contact to the NWs with many traditional thin film ohmic contact materials and especially transparent contacts such as indium tin oxide (ITO). More work must be performed on the minimization of the contact resistance to NWs. Secondly, while SIMS has proven to be remarkably powerful for NW ensembles, it is currently limited in the

analysis of single NWs. The progress of SIMS on NWs can be advanced by pursuing nanoSIMS on individual, isolated, vertically standing NWs to improve the spatial resolution of the technique. Thirdly, while AlInP passivation of GaAs NW resistors was successful by reducing surface depletion, this passivation layer must be implemented into NW solar cell devices in future work. This would extend the AlInP passivation to more practical devices and would additionally test its ability in reducing surface recombination. Finally, the electrostatic model for radial pn junctions should be expanded to include more complex structures such as pin junctions. More depth can be added to the model by including a model for the I-V characteristics of the NW device.

References

[1] R. S. Wagner and W. C. Ellis, Applied Physics Letters **4**, 89 (1964).

[2] V. Mourik, K. Zuo, S. M. Frolov, S. R. Plissard, E. P. a M. Bakkers, and L. P. Kouwenhoven, Science (New York, N.Y.) **336**, 1003 (2012).

[3] Y. Li, F. Qian, J. Xiang, and C. M. Lieber, Materials Today **9**, 18 (2006).

[4] T. Bryllert, L.-E. Wernersson, T. Löwgren, and L. Samuelson, Nanotechnology **17**, S227 (2006).

[5] H. Yu, Y. Sun, N. Singh, G.-Q. Lo, and D.-L. Kwong, Microelectronics Reliability **52**, 651 (2012).

[6] X. Chen, C. K. Y. Wong, C. a. Yuan, and G. Zhang, Sensors and Actuators B: Chemical **177**, 178 (2013).

[7] S. Gradecak, F. Qian, Y. Li, H.-G. Park, and C. M. Lieber, Applied Physics Letters **87**, 173111 (2005).

[8] E. D. Minot, F. Kelkensberg, M. van Kouwen, J. a van Dam, L. P. Kouwenhoven, V. Zwiller, M. T. Borgström, O. Wunnicke, M. a Verheijen, and E. P. a M. Bakkers, Nano Letters **7**, 367 (2007).

[9] H. Xia, Z.-Y. Lu, T.-X. Li, P. Parkinson, Z.-M. Liao, F.-H. Liu, W. Lu, W.-D. Hu, P.-P. Chen, H.-Y. Xu, J. Zou, and C. Jagadish, ACS Nano (2012).

[10] R. R. LaPierre, A. C. E. Chia, S. J. Gibson, C. M. Haapamaki, J. Boulanger, R. Yee, P. Kuyanov, J. Zhang, N. Tajik, N. Jewell, and K. M. a. Rahman, Physica Status Solidi (RRL) - Rapid Research Letters **16**, n/a (2013).

[11] R. Yan, D. Gargas, and P. Yang, Nature Photonics **3**, 569 (2009).

[12] C. Z. Ning, *Advances in Semiconductor Lasers*, 1st ed. (Elsevier Inc., 2012), pp. 455–486.

[13] M. S. Kang, C.-H. Lee, J. B. Park, H. Yoo, and G.-C. Yi, Nano Energy **1**, 391 (2012).

[14] G. E. Cirlin, V. G. Dubrovskii, I. P. Soshnikov, N. V. Sibirev, Y. B. Samsonenko, a. D. Bouravleuv, J. C. Harmand, and F. Glas, Physica Status Solidi (RRL) - Rapid Research Letters **3**, 112 (2009).

[15] S. Li and A. Waag, Journal of Applied Physics **111**, 071101 (2012).

[16] C. Soci, A. Zhang, X.-Y. Bao, H. Kim, Y. Lo, and D. Wang, Journal of Nanoscience and Nanotechnology **10**, 1430 (2010).

[17] R. Kapadia, Z. Fan, K. Takei, and A. Javey, Nano Energy **1**, 132 (2012).

[18] H. Goto, K. Nosaki, K. Tomioka, S. Hara, K. Hiruma, J. Motohisa, and T. Fukui, Applied Physics Express **2**, 35004 (2009).

[19] E. C. Garnett, M. L. Brongersma, Y. Cui, and M. D. McGehee, Annual Review of Materials Research **41**, 269 (2011).

[20] T. J. Kempa, R. W. Day, S.-K. Kim, H.-G. Park, and C. M. Lieber, Energy & Environmental Science **6**, 719 (2013).

[21] P. Krogstrup, H. I. Jørgensen, M. Heiss, O. Demichel, J. V Holm, M. Aagesen, J. Nygard, and A. Fontcuberta i Morral, Nature Photonics **7**, 306 (2013).

[22] H. J. Joyce, Q. Gao, H. Hoe Tan, C. Jagadish, Y. Kim, J. Zou, L. M. Smith, H. E. Jackson, J. M. Yarrison-Rice, P. Parkinson, and M. B. Johnston, Progress in Quantum Electronics **35**, 23 (2011).

[23] R. R. LaPierre, Journal of Applied Physics **110**, 014310 (2011).

[24] Y. Hu, M. Li, J.-J. He, and R. R. LaPierre, Nanotechnology **24**, 065402 (2013).

[25] J. Yang, D. Cheong, J. Rideout, S. Tavakoli, and R. Kleiman, in *2011 37th IEEE Photovoltaic Specialists Conference* (IEEE, 2011), pp. 001019–001024.

[26] L. Tsakalakos, Materials Science and Engineering: R: Reports **62**, 175 (2008).

[27] T. Stelzner, M. Pietsch, G. Andrä, F. Falk, E. Ose, and S. Christiansen, Nanotechnology **19**, 295203 (2008).

[28] L. Tsakalakos, J. Balch, J. Fronheiser, B. a. Korevaar, O. Sulima, and J. Rand, Applied Physics Letters **91**, 233117 (2007).

[29] J. Wallentin and M. T. Borgström, Journal of Materials Research **26**, 2142 (2011).

[30] L. J. Lauhon, M. S. Gudiksen, and C. M. Lieber, Philosophical Transactions. Series A, Mathematical, Physical, and Engineering Sciences **362**, 1247 (2004).

[31] R. R. LaPierre, Journal of Applied Physics **109**, 034311 (2011).

[32] M. D. Kelzenberg, S. W. Boettcher, J. A. Petykiewicz, D. B. Turner-Evans, M. C. Putnam, E. L. Warren, J. M. Spurgeon, R. M. Briggs, N. S. Lewis, and H. a Atwater, Nature Materials **9**, 239 (2010).

[33] G. Mariani, A. C. Scofield, C.-H. Hung, and D. L. Huffaker, Nature Communications **4**, 1497 (2013).

[34] A. C. E. Chia and R. R. LaPierre, Nanotechnology **22**, 245304 (2011).

[35] A. C. E. Chia, J. P. Boulanger, and R. R. LaPierre, Nanotechnology **24**, 045701 (2013).

[36] A. C. E. Chia and R. R. LaPierre, Journal of Applied Physics **112**, 063705 (2012).

[37] A. C. E. Chia and R. R. Lapierre, in *Nanotechnology 2013: Electronics, Devices, Fabrication, MEMS, Fluidics and Computational (Volume 2)* (2013), pp. 25–28.

[38] A. C. E. Chia, M. Tirado, F. Thouin, R. Leonelli, D. Comedi, and R. R. LaPierre, Semiconductor Science and Technology (2013).

[39] A. C. E. Chia and R. R. LaPierre, Journal of Applied Physics **114**, 074317 (2013).

[40] D. K. Schroder, *Semiconductor Material and Device Characterization* (John Wiley & Sons, Inc., Hoboken, NJ, USA, 2005).

[41] M. Schier, Journal of The Electrochemical Society **142**, 3238 (1995).

[42] https://www.elettra.trieste.it/lightsources/elettr (n.d.).

[43] M. K. Abyaneh, L. Gregoratti, M. Amati, M. Dalmiglio, and M. Kiskinova, e-Journal of Surface Science and Nanotechnology **9**, 158 (2011).

[44] L. F. Voss, Q. Shao, C. E. Reinhardt, R. T. Graff, A. M. Conway, R. J. Nikolić, N. Deo, and C. L. Cheung, Journal of Vacuum Science & Technology B: Microelectronics and Nanometer Structures **28**, 916 (2010).

[45] C. J. Novotny, E. T. Yu, and P. K. L. Yu, Nano Letters **8**, 775 (2008).

[46] S. Perraud, S. Poncet, S. Noël, M. Levis, P. Faucherand, E. Rouvière, P. Thony, C. Jaussaud, and R. Delsol, Solar Energy Materials and Solar Cells **93**, 1568 (2009).

[47] P. Nguyen, H. T. Ng, T. Yamada, M. K. Smith, J. Li, J. Han, and M. Meyyappan, Nano Letters **4**, 651 (2004).

[48] E. Latu-Romain, P. Gilet, P. Noel, J. Garcia, P. Ferret, M. Rosina, G. Feuillet, F. Lévy, and A. Chelnokov, Nanotechnology **19**, 345304 (2008).

[49] G. Cirlin, A. Bouravleuv, I. Soshnikov, Y. B. Samsonenko, V. Dubrovskii, E. Arakcheeva, E. Tanklevskaya, and P. Werner, Nanoscale Research Letters **5**, 360 (2009).

[50] Y. B. Tang, Z. H. Chen, H. S. Song, C. S. Lee, H. T. Cong, H. M. Cheng, W. J. Zhang, I. Bello, and S. T. Lee, Nano Letters **8**, 4191 (2008).

[51] C. Xu, X. Wang, and Z. L. Wang, Journal of the American Chemical Society **131**, 5866 (2009).

[52] E. P. DeGarmo, J. T. Black, and R. A. Kohser, *Materials and Processes in Manufacturing* (Wiley, 2007).

[53] C. Gutsche, I. Regolin, K. Blekker, A. Lysov, W. Prost, and F. J. Tegude, Journal of Applied Physics **105**, 024305 (2009).

[54] C. Gutsche, A. Lysov, I. Regolin, K. Blekker, W. Prost, and F.-J. Tegude, Nanoscale Research Letters **6**, 65 (2010).

[55] M. T. Borgström, E. Norberg, P. Wickert, H. a Nilsson, J. Trägårdh, K. a Dick, G. Statkute, P. Ramvall, K. Deppert, and L. Samuelson, Nanotechnology **19**, 445602 (2008).

[56] C. Liu, L. Dai, L. P. You, W. J. Xu, and G. G. Qin, Nanotechnology **19**, 465203 (2008).

[57] G. Imamura, T. Kawashima, M. Fujii, C. Nishimura, T. Saitoh, and S. Hayashi, Nano Letters **8**, 2620 (2008).

[58] P. Parkinson, H. J. Joyce, Q. Gao, H. H. Tan, X. Zhang, J. Zou, C. Jagadish, L. M. Herz, and M. B. Johnston, Nano Letters **9**, 3349 (2009).

[59] T. Richter, H. L. R. Meijers, R. Calarco, and M. Marso, Nano Letters **8**, 3056 (2008).

[60] J. E. Allen, D. E. Perea, E. R. Hemesath, and L. J. Lauhon, Advanced Materials **21**, 3067 (2009).

[61] E. Koren, N. Berkovitch, and Y. Rosenwaks, Nano Letters **10**, 1163 (2010).

[62] D. E. Perea, E. R. Hemesath, E. J. Schwalbach, J. L. Lensch-falk, P. W. Voorhees, and L. J. Lauhon, Nature Nanotechnology **4**, 315 (2009).

[63] D. E. Perea, J. L. Lensch, S. J. May, B. W. Wessels, and L. J. Lauhon, Applied Physics A **85**, 271 (2006).

[64] D. E. Perea, E. Wijaya, J. L. Lensch-Falk, E. R. Hemesath, and L. J. Lauhon, Journal of Solid State Chemistry **181**, 1642 (2008).

[65] T. J. Prosa, R. Alvis, L. Tsakalakos, and V. S. Smentkowski, Journal of Microscopy **239**, 92 (2010).

[66] C. M. Eichfeld, S. S. a Gerstl, T. J. Prosa, Y. Ke, J. M. Redwing, and S. E. Mohney, Nanotechnology **23**, 215205 (2012).

[67] J. R. Riley, R. a Bernal, Q. Li, H. D. Espinosa, G. T. Wang, and L. J. Lauhon, ACS Nano **6**, 3898 (2012).

[68] K.-K. Lew, L. Pan, T. E. Bogart, S. M. Dilts, E. C. Dickey, J. M. Redwing, Y. Wang, M. Cabassi, T. S. Mayer, and S. W. Novak, Applied Physics Letters **85**, 3101 (2004).

[69] M. C. Putnam, M. A. Filler, B. M. Kayes, M. D. Kelzenberg, Y. Guan, N. S. Lewis, J. M. Eiler, and H. A. Atwater, Nano Letters **8**, 3109 (2008).

[70] R. J. H. Morris, M. G. Dowsett, S. H. Dalal, D. L. Baptista, K. B. K. Teo, and W. I. Milne, Surface and Interface Analysis **39**, 898 (2007).

[71] R. G. Wilson, F. A. Stevie, and C. W. Magee, *Secondary Ion Mass Spectrometry: a Practical Handbook for Depth Profiling and Bulk Impurity Analysis* (Wiley-Interscience, 1989).

[72] R. R. Wixom, L. W. Rieth, and G. B. Stringfellow, Journal of Crystal Growth **269**, 276 (2004).

[73] S. H. Lee, C. Y. Fetzer, G. B. Stringfellow, D. H. Lee, and T. Y. Seong, Journal of Applied Physics **85**, 3590 (1999).

[74] M. Hilse, M. Ramsteiner, S. Breuer, L. Geelhaar, and H. Riechert, Applied Physics Letters **96**, 193104 (2010).

[75] J. F. Ziegler, M. D. Ziegler, and J. P. Biersack, Nuclear Instruments and Methods in Physics Research Section B: Beam Interactions with Materials and Atoms **268**, 1818 (2010).

[76] Y. Choi, J. Zhu, J. Grunes, J. Bokor, and G. A. Somorjai, The Journal of Physical Chemistry B **107**, 3340 (2003).

[77] V. Schmidt, S. Senz, and U. Gösele, Applied Physics A **86**, 187 (2006).

[78] B. S. Simpkins, M. a. Mastro, C. R. Eddy, and P. E. Pehrsson, Journal of Applied Physics **103**, 104313 (2008).

[79] D. Bednarczyk and J. Bednarczyk, Physics Letters A **64**, 409 (1978).

[80] S. M. Sze and K. K. Ng, *Physics of Semiconductor Devices* (John Wiley & Sons, Inc., Hoboken, NJ, USA, 2006).

[81] A. M. Cowley and S. M. Sze, Journal of Applied Physics **36**, 3212 (1965).

[82] S. Lodha, D. B. Janes, and N.-P. Chen, Journal of Applied Physics **93**, 2772 (2003).

[83] G. Myburg, W. E. Meyer, F. D. Auret, H. Burger, and W. O. Barnard, Materials Science and Technology **14**, 1269 (1998).

[84] N. Tajik, Z. Peng, P. Kuyanov, and R. R. LaPierre, Nanotechnology **22**, 225402 (2011).

[85] N. Sköld, L. S. Karlsson, M. W. Larsson, M.-E. Pistol, W. Seifert, J. Trägårdh, and L. Samuelson, Nano Letters **5**, 1943 (2005).

[86] J. Noborisaka, J. Motohisa, S. Hara, and T. Fukui, Applied Physics Letters **87**, 093109 (2005).

[87] O. Demichel, M. Heiss, J. Bleuse, H. Mariette, and A. Fontcuberta i Morral, Applied Physics Letters **97**, 201907 (2010).

[88] A. C. E. Chia, M. Tirado, Y. Li, S. Zhao, Z. Mi, D. Comedi, and R. R. LaPierre, Journal of Applied Physics **111**, 094319 (2012).

[89] N. Han, F. Wang, J. J. Hou, F. Xiu, S. Yip, A. T. Hui, T. Hung, and J. C. Ho, ACS Nano **6**, 4428 (2012).

[90] A. Lin, J. N. Shapiro, P. N. Senanayake, A. C. Scofield, P.-S. Wong, B. Liang, and D. L. Huffaker, Nanotechnology **23**, 105701 (2012).

[91] H. Hasegawa and T. Sawada, Thin Solid Films **103**, 119 (1983).

[92] M. C. Putnam, S. W. Boettcher, M. D. Kelzenberg, D. B. Turner-Evans, J. M. Spurgeon, E. L. Warren, R. M. Briggs, N. S. Lewis, and H. a. Atwater, Energy & Environmental Science **3**, 1037 (2010).

[93] J. Lloyd-Hughes, S. K. E. Merchant, L. Fu, H. H. Tan, C. Jagadish, E. Castro-Camus, and M. B. Johnston, Applied Physics Letters **89**, 232102 (2006).

[94] A. Luque and S. S. Hegedus, *Handbook of Photovoltaic Science and Engineering* (John Wiley & Sons, Ltd, Chichester, UK, 2003), pp. 1–43.

[95] Y. Gu, Y. G. Zhang, A. Z. Li, and H. Li, Materials Science and Engineering: B **139**, 246 (2007).

[96] J. A. Czaban, D. A. Thompson, and R. R. LaPierre, Nano Letters **9**, 148 (2009).

[97] M. C. Plante and R. R. LaPierre, Journal of Crystal Growth **310**, 356 (2008).

[98] M. C. Plante and R. R. LaPierre, Nanotechnology **19**, 495603 (2008).

[99] M. Levinshtein and M. Shur, *Handbook Series on Semiconductor Parameters*, v. 2 (World Scientific Publishing Company, Incorporated, 1995).

[100] T. Kim and P. H. Holloway, Critical Reviews in Solid State and Materials Sciences **22**, 239 (1997).

[101] O. Salehzadeh, K. L. Kavanagh, and S. P. Watkins, Journal of Applied Physics **113**, 134309 (2013).

[102] B. Tian, X. Zheng, T. J. Kempa, Y. Fang, N. Yu, G. Yu, J. Huang, and C. M. Lieber, Nature **449**, 885 (2007).

[103] O. Salehzadeh, M. X. Chen, K. L. Kavanagh, and S. P. Watkins, Applied Physics Letters **99**, 182102 (2011).

[104] J. Caram, C. Sandoval, M. Tirado, D. Comedi, J. Czaban, D. A. Thompson, and R. R. LaPierre, Nanotechnology **21**, 134007 (2010).

[105] B. M. Kayes, H. A. Atwater, and N. S. Lewis, Journal of Applied Physics **97**, 114302 (2005).

[106] Y. Hu, R. R. LaPierre, M. Li, K. Chen, and J.-J. He, Journal of Applied Physics **112**, 104311 (2012).